



# Planetary Mapping Tools Applied to Floor-Fractured Craters on Mars

Dissertation  
zur Erlangung des Doktorgrades  
doctor rerum naturalium (Dr.rer.nat.)  
in der Wissenschaftsdisziplin  
Geoinformatik, Fernerkundung und Kartographie

eingereicht an der Mathematisch-Naturwissenschaftlichen Fakultät  
der Universität Potsdam

von

Dipl.-Ing. Marlene Bamberg

Potsdam, 2014

This work is licensed under a Creative Commons License:  
Attribution – Noncommercial – Share Alike 4.0 International  
To view a copy of this license visit  
<http://creativecommons.org/licenses/by-nc-sa/4.0/>

Hauptgutachter und Betreuer: Prof. Dr. Hartmut Asche  
Institut für Geographie  
Universität Potsdam

Published online at the  
Institutional Repository of the University of Potsdam:  
URL <http://opus.kobv.de/ubp/volltexte/2014/7210/>  
URN <urn:nbn:de:kobv:517-opus-72104>  
<http://nbn-resolving.de/urn:nbn:de:kobv:517-opus-72104>





# Erklärung der Urheberschaft

Hiermit versichere ich, dass ich die vorliegende Doktorarbeit ohne Hilfe Dritter und ohne Benutzung anderer als der angegebenen Quellen und Hilfsmittel angefertigt habe. Wörtlich oder dem Sinn nach aus anderen Werken entnommene Stellen sind unter Angabe der Quellen kenntlich gemacht.



# Danksagung

Mein großer Dank geht an meinen Betreuer Herr Prof. Dr. Hartmut Asche (Universität Potsdam), sowie an Herrn Prof. Dr. Ralf Jaumann (DLR), die mich während der gesamten Arbeit stets mit fachlichen Anregungen und Hilfestellungen unterstützt haben, mir jedoch auch die Freiheit gelassen haben, das Projekt nach meinen Vorstellungen umzusetzen. Sie ermöglichten mir im Rahmen des Kooperationsprojektes zwischen der Universität Potsdam und dem DLR die Einrichtungen beider Institute zu nutzen und durch die Teilnahme an verschiedenen nationalen und internationalen Konferenzen meinen fachlichen Horizont zu erweitern. Dafür möchte ich mich ausdrücklich bedanken.

Weiter möchte ich mich bei meinen Kollegen am Institut für Planetenforschung (Abteilung der Planetengeologie und Geodäsie) und der Universität Potsdam (Institut für Geographie) bedanken, die mir mit fachlichen Diskussionen und Anregungen immer zur Seite standen. Durch ihre Hilfestellungen bei technischen und organisatorischen Aufgaben wurde ich auch in meinem Arbeitsalltag unterstützt, so dass ich ein sehr angenehmes Zusammenarbeiten genießen durfte. Auch danke ich meinen Kollegen der Freien Universität Berlin (Fachrichtung für Planetologie und Fernerkundung) für die Hilfsbereitschaft und erfolgreiche Zusammenarbeit.

Besonderer Dank gilt außerdem meinen Zimmerkollegen, die mit mir die letzten drei Jahre durchlebt haben. Die Mischung aus anregenden Diskussionen, fachlichen Ratschlägen aber auch angenehmen Pausen hat immer für einen interessanten und ausgewogenen Arbeitsalltag gesorgt.

Ganz besonders möchte ich mich bei denjenigen bedanken, die mich bei der Fertigstellung der Arbeit tatkräftig unterstützt und mir unermüdlich Hilfestellung gegeben haben. Besondere Hochachtung und Dankbarkeit geht hier an meinen Korrekturleser und meine Korrekturleserinnen. Vielen Dank für die unermüdliche Unterstützung und die tollen Ideen.

Von ganzem Herzen danke ich meiner Familie. Ohne die grenzenlose und uneingeschränkte Unterstützung meiner Eltern könnte ich nicht in der Position sein in der jetzt glücklicherweise bin. Sie waren immer für mich da und haben gemeinsam mit meinem Bruder meine innere Ausgeglichenheit und Stärke aufgebaut und gefestigt, die ich während meiner Dissertationsarbeit und in manchen Lebenssituationen dringend gebraucht habe. Danke.





# Kurzfassung

Planetenforschung umfasst oft zeitintensive Projekte, bei denen Expertise und Erfahrung eine wesentliche Rolle spielen. Auf Grund äußerst komplexer und sich selten wiederholender Forschungsfragen sind Annahmen, Definitionen und Regeln zur Lösung dieser Fragen nicht leicht nachvollziehbar oder aber nicht eindeutig dokumentiert. Ein Vergleich der Ergebnisse unterschiedlicher Forscher zum selben Thema oder eine Erweiterung der Forschungsfrage macht dies somit nur schwer möglich. Vergleiche liefern oftmals verzerrte Ergebnisse, da die Ausgangslage und Randbedingungen unterschiedlich definiert worden sind.

Das Ziel dieser Arbeit ist es eine Standardmethode zur Oberflächenanalyse zu entwickeln, die auf zahlreiche Untersuchungsfragen angewandt werden kann. Eine gleichbleibende Qualität der Ergebnisse muss durch diese Methode gewährleistet sein. Ein weiteres Ziel ist es, dass diese Methode ohne Vorwissen und Expertise im Bereich Informatik angewandt werden kann und die Ergebnisse in kurzer Zeit vorliegen. Außerdem müssen die Ergebnisse vergleichbar und nachvollziehbar sein. Automatisch operierende Analysewerkzeuge können die zahlreichen Anforderungen erfüllen und als Standardmethode dienen. Statistische Ergebnisse werden durch diese Methode erzielt. Die Werkzeuge basieren auf vordefinierten, geowissenschaftlichen Techniken und umfassen Messungen, Berechnungen und Klassifikationen der zu untersuchenden Oberflächenstrukturen. Für die Anwendung dieser Werkzeuge müssen Schlüsselstrukturen und Randbedingungen definiert werden. Des Weiteren benötigen die Werkzeuge eine Datenbank, in der alle Oberflächenstrukturen, aber auch Informationen zu den Randbedingungen gespeichert sind. Es ist mit geringem Aufwand möglich, Datenbanken zu aktualisieren und sie auf verschiedenste Fragestellungen zu adaptieren. Dies steigert die Flexibilität, Reproduzierbarkeit und auch Vergleichbarkeit der Untersuchung.

Die vordefinierten Randbedingungen und die Qualität der Datenbank haben jedoch auch direkten Einfluss auf die Qualität der Ergebnisse. Um eine gleichbleibend hohe Qualität der Untersuchung zu gewährleisten muss sichergestellt werden, dass alle vordefinierten Bedingungen eindeutig sind und auf vorheriger Forschung basieren.

Die automatisch operierenden Analysewerkzeuge müssen als mögliche Standardmethode getestet werden. Hierbei geht es darum Vorteile, aber auch Nachteile zu identifizieren und zu bewerten. In dieser Arbeit werden die Analysewerkzeuge auf einen bestimmten Einschlagskratertyp auf dem Mars angewandt. Krater mit zerbrochenen Kraterböden (Floor-Fractured Craters) sind in verschiedensten Regionen auf dem Mars zu finden, sie zeigen zahlreiche Oberflächenstrukturen und wurden durch unterschiedliche Prozesse geformt. All diese Fakten machen diesen Kratertyp zu einem interessanten und im geologischen und morphologischen Sinne sehr komplexen Anwendungsgebiet. 433 Krater sind durch die Werkzeuge analysiert und je nach Entstehungsprozess klassifiziert worden. Für diese Analyse sind Position der Krater, Art des Umfeldes und Strukturen im Kraterinneren ausschlaggebend. Die kombinierten Informationen geben somit Auskunft über die Prozesse, welche zum Zerbrechen des Kraterbodens geführt haben.

Die entwickelten Analysewerkzeuge können geologische Prozesse, die sehr ähn-

lich sind, von einander abhängig sind und zusätzlich auch dieselben Oberflächenstrukturen formen, nicht eindeutig unterscheiden. Aus diesem Grund sind fluviale und glaziale Entstehungsprozesse für den untersuchten Kratertyp zusammengefasst. Die Analysewerkzeuge liefern Wahrscheinlichkeitswerte für drei mögliche Entstehungsarten. Um die Qualität der Ergebnisse zu verbessern muss eine Wahrscheinlichkeit über 50 % erreicht werden. Die Werkzeuge zeigen, dass 15 % der Krater durch Vulkanismus, 20 % durch Tektonik und 43 % durch Wasser- und Eis-bedingte Prozesse gebildet wurden. Insgesamt kann für 75 % des untersuchten Kratertyps ein potentieller Entstehungsprozess zugeordnet werden. Für 25 % der Krater ist eine Klassifizierung nicht möglich. Dies kann durch eine Kombination von geologischen Prozessen, einer Überprägung von wichtigen Schlüsselstrukturen, oder eines bisher nicht berücksichtigten Prozesses erklärt werden.

Zusammenfassend ist zu sagen, dass es möglich ist planetare Oberflächenstrukturen quantitativ durch automatisch operierende Analysewerkzeuge zu erfassen und hinsichtlich einer definierten Fragestellung zu klassifizieren. Zusätzliche Informationen können durch die entwickelten Werkzeuge gewonnen werden, daher sind sie als Assistenzsystem zu betrachten.

# Abstract

Planetary research is often user-based and requires considerable skill, time, and effort. Unfortunately, self-defined boundary conditions, definitions, and rules are often not documented or not easy to comprehend due to the complexity of research. This makes a comparison to other studies, or an extension of the already existing research, complicated. Comparisons are often distorted, because results rely on different, not well defined, or even unknown boundary conditions.

The purpose of this research is to develop a standardized analysis method for planetary surfaces, which is adaptable to several research topics. The method provides a consistent quality of results. This also includes achieving reliable and comparable results and reducing the time and effort of conducting such studies. A standardized analysis method is provided by automated analysis tools that focus on statistical parameters. Specific key parameters and boundary conditions are defined for the tool application. The analysis relies on a database in which all key parameters are stored. These databases can be easily updated and adapted to various research questions. This increases the flexibility, reproducibility, and comparability of the research. However, the quality of the database and reliability of definitions directly influence the results. To ensure a high quality of results, the rules and definitions need to be well defined and based on previously conducted case studies. The tools then produce parameters, which are obtained by defined geostatistical techniques (measurements, calculations, classifications).

The idea of an automated statistical analysis is tested to prove benefits but also potential problems of this method. In this study, I adapt automated tools for floor-fractured craters (FFCs) on Mars.

These impact craters show a variety of surface features, occurring in different Martian environments, and having different fracturing origins. They provide a complex morphological and geological field of application. 433 FFCs are classified by the analysis tools due to their fracturing process. Spatial data, environmental context, and crater interior data are analyzed to distinguish between the processes involved in floor fracturing.

Related geologic processes, such as glacial and fluvial activity, are too similar to be classified separately by the automated tools. Glacial and fluvial fracturing processes are merged together for the classification. The automated tools provide probability values for each origin model. To guarantee the quality and reliability of the results, classification tools need to achieve a probability of 50 % for the origin. This analysis method shows that 15 % of the FFCs are fractured by intrusive volcanism, 20 % by tectonic activity, and 43 % by water & ice related processes. In total, 75 % of the FFCs are classified to an origin type. This can be explained by a combination of origin models, superposition or erosion of key parameters, or an unknown fracturing model. Those features have to be manually analyzed in detail. Another possibility would be the improvement of key parameters and rules for the classification.

This research shows that it is possible to conduct an automated statistical analysis of morphologic and geologic features based on analysis tools. Analysis tools provide additional information to the user and are therefore considered assistance systems.



# Contents

<b>List of Figures</b>	<b>xv</b>
<b>List of Tables</b>	<b>xviii</b>
<b>List of Abbreviations</b>	<b>xxi</b>
<b>1. Introduction</b>	<b>1</b>
1.1. Motivation and Purpose . . . . .	1
1.2. Structure of the Thesis . . . . .	2
<b>1. Technical and Scientific Background</b>	<b>3</b>
<b>2. Geographical Information Systems (GIS)</b>	<b>5</b>
2.1. Definition . . . . .	5
2.2. ArcGIS and JMars . . . . .	5
2.3. Data Models . . . . .	6
2.4. Coordinate Systems and Projections . . . . .	8
2.5. Data Analyses in GIS . . . . .	10
2.5.1. Measurements . . . . .	10
2.5.2. Calculations . . . . .	10
2.5.3. Attribute & Spatial Analyses . . . . .	11
2.6. Automated Systems . . . . .	12
2.6.1. ModelBuilder . . . . .	12
2.6.2. Expert Systems . . . . .	12
2.7. Databases . . . . .	14
<b>3. Data and Data Processing</b>	<b>17</b>
3.1. Remote Sensing . . . . .	17
3.1.1. Scanning Systems . . . . .	17
3.1.2. Spectra . . . . .	19
3.1.3. Resolution . . . . .	19
3.2. Data Processing . . . . .	20
3.2.1. Data Quality . . . . .	21
3.2.2. Pre-Processing . . . . .	21
3.2.3. Data Processing Software . . . . .	23
3.3. Instruments . . . . .	23
3.3.1. Mars Orbiter Laser Altimeter (MOLA) . . . . .	23
3.3.2. Thermal Emission Spectrometer (TES) . . . . .	24
3.3.3. Thermal Emission Imaging System (THEMIS) . . . . .	25
3.3.4. High Resolution Stereo Camera (HRSC) . . . . .	25
3.3.5. Context Camera (CTX) . . . . .	26

<b>4. Floor-Fractured Craters (FFCs)</b>	<b>29</b>
4.1. Why Select FFCs?	29
4.2. Discovery and Research of FFCs	29
4.3. Possible Formation Processes	30
4.3.1. Intrusive Volcanism	30
4.3.2. Subsurface Ice	30
4.3.3. Groundwater Migration	31
4.3.4. Rayleigh Convection	32
4.3.5. Deep-Water Fault Systems	33
4.3.6. Tectonics	34
4.4. Importance of FFCs	34
<b>II. Methods</b>	<b>37</b>
<b>5. Manual Crater Analysis</b>	<b>39</b>
5.1. Data and Software used for Crater Analysis	39
5.2. Observations of Crater A	40
5.2.1. Geologic Setting and Crater Morphology	40
5.2.2. Measurements	44
5.2.3. Crater Size Frequency Distribution	45
5.3. Observation of Crater Lipany	46
5.3.1. Geologic Setting and Crater Morphology	46
5.3.2. Measurements	47
5.3.3. Crater Size Frequency Distribution	47
<b>6. Databases</b>	<b>53</b>
6.1. Parameters for the Database	53
6.1.1. Interior Surface Features	53
6.1.2. Exterior Surface Features	54
6.2. Generating the Database	56
<b>7. Automated Tools for Analysis of FFCs</b>	<b>67</b>
7.1. Purpose	67
7.2. Automation and User-Based Analysis	67
7.3. Hierarchic Structure	68
7.4. Tools	70
7.4.1. Measurements	70
7.4.2. Calculations	75
7.4.3. Classifications	77
<b>8. Implementation in ArcGIS</b>	<b>85</b>
8.1. Programming Language: Python	85
8.2. Python in ArcGIS	85
8.3. ArcGIS Tools	86

<b>III. Quantitative and Qualitative Analysis</b>	<b>87</b>
<b>9. Result of Case Study</b>	<b>89</b>
9.1. Chronology . . . . .	89
9.1.1. Crater A . . . . .	89
9.1.2. Crater Lipany . . . . .	90
9.2. Origin of Fracturing in Observed Craters . . . . .	90
9.2.1. Crater A . . . . .	90
9.2.2. Crater Lipany . . . . .	92
<b>10. Result of Tool Analysis</b>	<b>95</b>
10.1. General Attributes of FFCs . . . . .	95
10.1.1. Location . . . . .	95
10.1.2. Size . . . . .	95
10.1.3. Depth . . . . .	95
10.2. Crater Interior . . . . .	97
10.2.1. Surface Features . . . . .	97
10.2.2. Elevation . . . . .	99
10.3. Crater Context . . . . .	102
10.3.1. Surface Features . . . . .	102
10.3.2. Erosion & Paleolakes . . . . .	102
10.4. Origin Types . . . . .	103
10.4.1. Result of the Six Origin Types . . . . .	103
10.4.2. Most Likely Origin for each FFC . . . . .	105
10.4.3. Origin Types in Detail . . . . .	106
10.4.4. Case Study Craters . . . . .	109
<b>11. Discussion</b>	<b>111</b>
11.1. Interpretation of Tool Analysis Results . . . . .	111
11.2. Three Final Origin Types . . . . .	118
11.3. Limits of the Classification Tools . . . . .	118
11.4. Comparison of Manual and Automated Analysis . . . . .	119
11.5. Advantages . . . . .	121
<b>12. Summary &amp; Conclusion</b>	<b>123</b>
12.1. Technical Results . . . . .	123
12.2. Scientific Results . . . . .	124
<b>13. Future Work</b>	<b>127</b>
13.1. Technical Improvements . . . . .	127
13.2. Scientific Applications . . . . .	128
<b>Appendix</b>	<b>141</b>
Publications . . . . .	141
Conference Contributions . . . . .	141
Awards . . . . .	142
Curriculum Vitae . . . . .	143





# List of Figures

2.1.	Attribute table . . . . .	7
2.2.	Vector and raster data . . . . .	8
2.3.	Schematic overview of image data processing for a GIS . . . . .	9
2.4.	ESRI tool examples . . . . .	13
3.1.	Scanning principles . . . . .	19
3.2.	The electromagnetic spectrum . . . . .	20
3.3.	Remote sensing principles . . . . .	21
3.4.	Data workflow . . . . .	22
3.5.	Global MOLA map . . . . .	24
3.6.	THEMIS-VIS coverage . . . . .	26
3.7.	HRSC coverage . . . . .	27
3.8.	CTX coverage . . . . .	27
4.1.	Model of intrusive volcanism . . . . .	31
4.2.	Model of subsurface ice . . . . .	32
4.3.	Model of groundwater migration . . . . .	33
4.4.	Model of density-driven convection . . . . .	34
4.5.	Model of deep-water fault systems . . . . .	35
4.6.	Model of tectonic systems . . . . .	35
5.1.	Geologic map and cross-section of Crater A . . . . .	41
5.2.	Surface features Crater A . . . . .	42
5.3.	Calculated and measured crater morphologies . . . . .	43
5.4.	Fault orientations Crater A . . . . .	44
5.5.	Elevation Crater A . . . . .	45
5.6.	Crater size frequency distribution Crater A . . . . .	46
5.7.	Geologic map and cross-section of Crater Lipany . . . . .	48
5.8.	Surface features Crater Lipany . . . . .	49
5.9.	Elevation Crater Lipany . . . . .	50
5.10.	Crater size frequency distribution Crater Lipany . . . . .	51
6.1.	Map of dichotomy boundary of Mars . . . . .	57
6.2.	Map of chaotic and fretted terrains of Mars . . . . .	58
6.3.	Map of tectonic systems of Mars . . . . .	59
6.4.	Map of volcanic regions of Mars . . . . .	60
7.1.	Automated and user-based tasks . . . . .	68
7.2.	Hierarchical structure for interior classifications . . . . .	69
7.3.	Hierarchical structure for exterior classifications . . . . .	70
7.4.	Tool: Diameter . . . . .	71
7.5.	Tool: Feature Elevation . . . . .	72
7.6.	Tool: Location . . . . .	73
7.7.	Tool: Peak & Pit . . . . .	74

7.8.	Tool: Size . . . . .	75
7.9.	Tool: Feature Depth . . . . .	76
7.10.	Tool: Post-Modification Crater Depth . . . . .	77
7.11.	Tool: Thickness . . . . .	78
9.1.	Correlation map of Crater A and Lipany . . . . .	89
10.1.	Distribution map of 433 FFCs . . . . .	96
10.2.	Diagram of crater diameters and crater types . . . . .	97
10.3.	Diagram of crater depth, post-modification crater depth, and thickness of infilling . . . . .	98
10.4.	Diagram of depressions, fracturing, linear features, mesas, terraces, and uplift . . . . .	99
10.5.	Diagram of crater rim and floor elevation . . . . .	100
10.6.	Diagram of channels, ejecta, fluvial, glacial, tectonic, and volcanic features . . . . .	101
10.7.	Diagram of erosion type and potential paleolakes . . . . .	102
10.8.	Histograms of the six origin types . . . . .	104
10.9.	Histogram of maximum probability for all origin types . . . . .	105
10.10.	Most probable origin type for all FFCs . . . . .	107
10.11.	Global distribution map for FFC origin types . . . . .	108
10.12.	Probabilities of origin types for case study . . . . .	109
11.1.	Three FFC formation models for Mars . . . . .	119
11.2.	Global map of three FFC formation models . . . . .	120

# List of Tables

3.1. Mars missions . . . . .	18
3.2. Instrument overview . . . . .	23
5.1. Overview of depth values Crater A . . . . .	46
5.2. Overview of depth values Crater Lipany . . . . .	51
6.1. Surface features inside FFCs . . . . .	62
6.2. Surface features outside FFCs . . . . .	65



# List of Abbreviations

GIS	Geographical Information System
FFC	Floor-Fractured Crater
ANSI	American National Standards Institute
ASU	Arizona State University
BCC	Buffered Crater Counting
CCD	Charge-Couple-Device
CSFD	Crater Size Frequency Distribution
CTX	Context Camera
DBMS	DataBase Management System
DLR	German Aerospace Center
DN	Digital Number
DTM	Digital Terrain Model
ESA	European Space Agency
FOV	Field of View
GDAL	Geospatial Data Abstraction Library
GUI	Graphical User Interface
HRSC	High Resolution Stereo Camera
IAU	International Astronomical Union
IDLE	Integrated Development Environment
JMars	Java Mission-planning and Analysis for Remote Sensing
JPL	Jet Propulsion Laboratory
LoD	Level of Detail
MEGDR	Mission Experiment Gridded Data Record
MEX	Mars Express
MGS	Mars Global Surveyor
MO	Mars Odyssey
MOLA	Mars Orbiter Laser Altimeter
MRO	Mars Reconnaissance Orbiter
NASA	National Aeronautics and Space Administration
ODE	Orbital Data Explorer
PDS	Planetary Data System
PEDR	Precision Experiment Data Records
SPARC	Standards Planning and Requirements Committee
SQL	Structured Query Language
SRC	Super Resolution Channel
TES	Thermal Emission Spectrometer
THEMIS	Thermal Emission Imaging System
USGS	U.S.Geological Survey
VGIS	Virtual GIS
VICAR	Video Image Communication and Retrieval System
VMS	Virtual Memory System



# 1. Introduction

The introduction covers the purpose of this thesis and the motivation of conducting this research. Additionally, a brief overview of the thesis structure is included.

## 1.1. Motivation and Purpose

Planetary geologists analyze the composition, structure, and processes of a planetary surface and upper crust. Research in planetary science is mostly based on remote sensing data. Data sets often differ in data size, data type, resolution, and coordinate and reference system. The high diversity and variety of these data sets is handled within geographical information systems (GIS). They are used to manage, manipulate, analyze, and visualize geographical information.

On Mars, planetary research is often user-based, not automated, and limited to certain regions. This leads to high quality analyses, including mappings of surface geology and mineralogy, geomorphological features, and age dating obtained by crater size frequency distributions. However, local analyses are of high importance to understand the processes of features that are developed on planetary bodies. This type of research requires considerable skill, time, and effort. Unfortunately, self-defined boundary conditions, definitions, and rules are often not documented or not easy to comprehend due to the complexity of research. This makes a comparison to other research, or an extension of the already existing research, complicated. Comparisons are often distorted, because results rely on different, not well defined, or even unknown boundary conditions.

The purpose of this study is to develop automated analysis tools, focusing on statistical parameters. The tools provide parameters, which are obtained by defined geostatistical techniques. Hence, the tools guarantee a consistent quality of results. This also includes achieving reliable, comparable, and usable results, but also reducing the time and effort of conducting such studies. Time and effort of the user will be reduced if the statistical analysis runs automatically. An automated, statistical analysis can be conducted within a GIS by means of tools. Specific key parameters and boundary conditions are defined for the tool application. With definitions and rules determined and parameters available, a statistical analysis can be conducted automatically. The analysis relies on a database in which all key parameters (and any additional information) are stored. Databases can be adapted to various research questions by neglecting or considering existing parameters. Updates of the database can also be easily applied. The entire database, or just selected entries, can be analyzed by the automated method. This increases the flexibility, reproducibility, and comparability of the research. It is of high importance to obtain comparable and reusable results. To ensure this, the rules and definitions need to be well defined and based on previously conducted case studies. The quality of the database and reliability of definitions will directly influence the results.

The idea of an automated statistical analysis has been tested to prove benefits but also potential problems and limitations of this method. In this study, I adapt automated tools for floor-fractured craters (FFCs) on Mars. These impact craters

have a variety of surface features and also occur in different Martian environments. I discuss several processes (volcanism, tectonics, water, ice) that may be responsible for fracturing development of crater floors. Are those different processes recognizable in the FFCs? Which processes developed the floor-fracturing on Mars? How many FFCs are developed and modified by water, ice, volcanic, or tectonic processes? Is it possible to identify a formation process for the fracturing based on the observed geomorphological features? Is there a relationship between the location of the impact crater and the processes which lead to the fracturing? Spatial data, environmental context, and crater interior data need to be analyzed to answer these questions. FFC distributions must be established and the reason for fracturing classified. For each origin type, key parameters and rules must be defined on which the tools will operate and automatically conduct the classification the FFCs regarding to their origin type.

Automated statistical analysis tools become increasingly important in various scientific fields of research. They have superhuman capabilities due to their intersubjectivity, resulting in consistent quality of results. These tools describe the base for a standardized analysis method, which could be adapted to several research topics. Analysis tools provide additional information and help to the user and are therefore considered assistance systems.

## 1.2. Structure of the Thesis

This project is positioned between geoscientific research and spatial information processing.

To successfully obtain the aim of this research, a concept for the development and implementation of such automated analysis tools is required. The project needs to be split up into smaller work packages to operationalize the method. These work packages are presented in the chapters of this thesis. The technical introduction includes background information about geographical information systems (Chapter 2) and also the data and data processing (Chapter 3). Chapter 4 introduces the geologic research of floor-fractured craters (FFCs), which represents an excellent topic for the tool application.

The next work steps include the methods to finally develop and implement automated tools. Chapter 5 contains a case study that represents a conventional, manual crater analysis. The knowledge gathered in that chapter is used to define boundary conditions and key parameters for the automated analysis tools. It represents the first step of the tool development. After defining key parameters and boundary conditions, a database of FFCs on Mars (Chapter 6) is established. The tools have to be applied to the database, because all required information about the FFCs are stored there. Chapter 7 shows the tool analysis and the development of automated classification, calculation, and measurement tools. These provide the statistical analysis of FFCs and thus, represent an important work package of this research. The methods section closes with the implementation of these tools into a geographical information system (Chapter 8).

The results of the case study are shown in Chapter 9. These results are followed by the tool analysis results in Chapter 10. The differences and resulting advantages and disadvantages between a conventional and an automated statistical tool analysis are discussed in Chapter 11. The outcome of the project is split up into technical and scientific results and summarized in Chapter 12. Different tool applications and potential improvements can be found in Chapter 13.



## Part I.

# Technical and Scientific Background



## 2. Geographical Information Systems (GIS)

This chapter gives an introduction into geographical information systems and their usage. Within GIS spatial and attribute analyses can be performed. For these analyses data storage and management is of high importance and will be discussed in the database section.

### 2.1. Definition

A geographical information system (GIS) is a software for the management and manipulation of geographical information. This term describes a system to process data that have a georeferenced and therefore, defined position in terms of coordinates. It was developed in the 1960s [Gomarasca, 2004] and defined by e.g. Burrough [1986]:

'GIS is a powerful set of tools for collecting, storing, retrieving at will, transforming and displaying spatial data from the real world.'

Several definitions can be found in the literature, they all refer to a GIS as a powerful software including tools to capture, manage, store and present spatial data. Images of different resolution, reference system and projection can be included and adapted to each other in the GIS. The combination of various spatial datasets allows a geoscientific analysis and interpretation. It was originally developed to improve the analysis and interpretation of Earth data, but it can be also adapted to other planetary bodies. Consequently a GIS is a powerful tool for planetary data analysis.

Planetary missions collect large amount of image data by using remote sensing techniques. Every day we receive new data from various planets, moons and asteroids in our solar system. Depending on the resolution high coverage of the surface is available. Overlapping image segments can occur and give more information about short term surface processes. A GIS provides several tools for planetary mapping. The tools allow measuring and calculating of various parameters within the digital images. It is also possible to include or develop new tools that are needed to fulfill specific measurements or calculations. Furthermore, geologic mappings, cross-sections, spatial and attribute queries can be conducted within the GIS, by using georeferenced data.

Several GIS software products are available. They all follow the same purpose, but differ in aspects like quality and amount of analyses tools, or reference system.

### 2.2. ArcGIS and JMars

For this research I selected the two software products JMars 3.0.4 [Christensen et al., 2013] and ArcGIS 10.0 [ESRI, 2013].

JMars is an acronym and stands for Java Mission- planning and Analysis for Remote Sensing. The software is an open source GIS, which was developed by

the Mars Space Flight Facility at the Arizona State University (ASU) [Christensen et al., 2013]. JMars was only developed for the planet Mars and therefore, has a fixed reference system. It provides access to free image data obtained by various Mars missions including Viking, Mars Global Surveyor, Mars Odyssey, Mars Express and the Mars Reconnaissance Orbiter. These image data do not need to be processed, regarding file format and projection, by the user. The images can be loaded directly into the GIS. Multiple data sets can be loaded and compared within JMars. Simple mapping operations and attribute analyses can be also conducted by using scripting in the Structured Query Language (SQL). JMars was mainly used for the global observation and characterization, including measurements and calculations, of surface features on Mars.

The software ArcGIS is developed by ESRI and represents a commonly used and advanced GIS [ESRI, 2013]. It is used by a large community, mainly focusing on Earth science. ArcGIS presents a software with hundreds of tools for geoscientific research and also the possibilities to create and adapt the tools to the users needs. It also supports various programming languages to allow enhanced research. DataBase Management Systems (DBMS) are also available and provide additional support in building and managing databases. ArcGIS was used for the qualitative and quantitative analyses, this also includes database generation and coding for obtaining attribute and spatial classifications.

All obtained files can be accessed in ArcGIS and JMars. Both software systems have advantages and complement one another to perform qualitative and quantitative analyses for planetary science.

## 2.3. Data Models

In general two data types are essential for GIS analyses. Geographic data describe the elements of the real world in terms of coordinates. Attribute data define the semantic characteristics of geographic data and include qualitative and quantitative data. The combination of both data types is the basis for planetary research.

For implementing these data into the GIS two different input formats can be used: vector and raster data (Fig. 2.2). The vector format was established in the 1960s and used for computer-controlled drafting machines. The vector format represents observed features by points, lines and polygons which are geographically referenced by Cartesian coordinates [Burrough, 1986]. Vector data have several advantages. First they do not require large amounts of memory; second they can be re-sized without an information loss. More information regarding advantages and disadvantages are available in Gomarasca [2004], O'Sullivan and Unwin [2010].

Within a GIS new vector datasets can be generated. They are called Shapefiles (in ArcGIS terminology) and contain information about point, line and polygon features, but also about the graphical output and visualization. Within the shapefile the attribute table shows all obtained data (Fig. 2.1). It also provides the ability of managing and manipulating these data.

Geographical space is divided into a grid of identically sized square cells. These cells are pixels. Each pixel shows an estimated or calculated value for a single attribute in that geographic position (e.g. elevation, albedo, temperature). Consequently only one attribute can be associated in each cell. Multiple raster data sets are necessary for different attributes. This file format, also called raster format was developed in the 1970s [Gomarasca, 2004].

FID	Shape	LAT	LOX	D	AREA	REGION	efloor	FFC	FILLED	CHANNEL	DEPRESSION	UPLIFT	LF	EJECTA	VOLCANIC	FLUVIAL	TECTONIC	GLACIAL	M
0	Polygon	29.295877	70.42963	91.099785	6518.168809	Arabia Terra	-610.285726	1	1	2	0	0	1	0	0	1	0	1	1
1	Polygon	29.321817	68.577095	52.715946	2152.603795	Arabia Terra	-334.265652	1	1	2	1	0	1	0	1	1	0	1	1
2	Polygon	30.250521	67.955815	32.092435	808.902627	Arabia Terra	-464.681838	1	1	2	0	0	0	0	0	1	0	1	0
3	Polygon	31.058714	68.34497	72.617811	4141.686286	Arabia Terra	-617.923318	1	1	2	0	0	0	1	0	1	0	1	1
4	Polygon	32.021868	68.889643	47.512964	1773.026166	Arabia Terra	-844.572385	1	1	2	0	0	0	1	0	1	1	1	1
5	Polygon	30.670969	63.323039	95.947582	7230.344045	Arabia Terra	-1004.848108	1	1	2	0	0	0	0	0	1	1	1	1
6	Polygon	30.388691	62.144559	51.422357	2076.800632	Arabia Terra	-987.288879	1	1	2	1	0	1	0	0	1	0	1	1
7	Polygon	31.361617	60.059899	35.49378	989.45355	Arabia Terra	-1010.350726	1	1	2	0	0	1	0	1	1	0	1	1
8	Polygon	31.339297	59.27871	35.497998	989.688728	Arabia Terra	-1138.013989	1	1	2	0	0	0	0	1	1	0	1	1
9	Polygon	32.064751	58.847797	18.748245	276.065514	Arabia Terra	-946.854101	1	1	2	1	0	0	0	0	1	0	1	0
10	Polygon	32.477479	59.25639	22.122184	384.367694	Arabia Terra	-1695.39276	1	1	2	0	0	0	0	0	1	1	1	0
11	Polygon	32.914988	59.35906	27.109767	577.221444	Arabia Terra	-1888.551124	1	1	2	0	0	0	1	0	0	1	1	0
12	Polygon	40.1426	51.618589	55.404046	2410.870348	Arabia Terra	-2011.168462	1	1	2	0	0	0	0	0	1	1	1	1
13	Polygon	38.267903	38.697716	63.361102	3153.089781	Arabia Terra	-1748.950814	1	1	2	0	0	0	0	1	1	1	1	1
14	Polygon	37.343294	37.124177	32.689253	839.268435	Arabia Terra	-1144.862367	1	1	2	0	0	0	0	1	1	0	1	0
15	Polygon	33.13146	29.354251	127.318448	12731.324036	Arabia Terra	-2021.53161	1	1	2	0	0	0	0	0	1	1	1	1
16	Polygon	32.396035	28.433081	38.274607	1150.56823	Arabia Terra	-2702.521752	1	1	2	0	0	0	1	0	1	0	1	1
17	Polygon	32.584704	25.28365	44.960796	1587.665021	Arabia Terra	-2105.833389	1	1	2	1	0	0	0	0	1	0	1	1
18	Polygon	29.739823	20.488502	73.149683	4202.578139	Arabia Terra	-2157.444102	1	1	2	1	0	0	0	0	1	0	1	0
19	Polygon	29.576884	19.371982	16.785501	221.288845	Arabia Terra	-1635.952456	1	1	2	1	0	0	0	0	1	1	1	1
20	Polygon	29.064647	17.135548	16.848061	222.941403	Arabia Terra	-2198.476806	1	1	2	1	0	0	0	1	1	0	1	1
21	Polygon	28.344879	15.337697	24.04107	453.940037	Arabia Terra	-2152.661882	1	1	2	0	0	1	0	0	1	0	1	0
22	Polygon	26.808201	10.509947	28.981344	659.671824	Arabia Terra	-2233.409827	1	1	2	0	0	0	0	0	0	0	1	0
23	Polygon	27.871759	9.48882	127.540522	12775.775571	Arabia Terra	-2526.178694	1	1	2	0	0	0	0	1	1	0	1	0
24	Polygon	28.137335	8.015721	27.879054	610.445593	Arabia Terra	-2185.553667	1	1	2	0	0	0	0	1	1	0	1	0
25	Polygon	28.684759	7.315127	7.712229	46.714396	Arabia Terra	-2144.166078	1	1	2	1	0	0	0	0	1	0	1	0
26	Polygon	27.400943	6.043775	43.553007	1489.797316	Arabia Terra	-2708.465895	1	1	2	0	0	1	0	0	1	0	1	0
27	Polygon	26.749331	7.280263	16.347881	209.900679	Arabia Terra	-2142.723605	1	1	2	0	0	0	0	1	1	0	1	0
28	Polygon	26.003705	10.017796	28.093064	619.853579	Arabia Terra	-2625.269576	1	0	0	0	0	0	0	0	0	0	1	0
29	Polygon	25.486906	10.948529	97.022846	7393.31005	Arabia Terra	-2831.527414	1	1	2	1	0	0	1	0	1	0	1	1
30	Polygon	29.06465	7.644098	17.3917	237.560896	Arabia Terra	-2410.627232	1	1	2	0	0	1	0	0	1	0	1	0
31	Polygon	29.805907	6.639711	95.117299	7105.749917	Arabia Terra	-2939.856035	1	1	2	1	1	1	0	0	1	0	1	0
32	Polygon	26.02667	4.975586	66.580319	3481.630152	Arabia Terra	-2695.362497	1	1	2	0	1	1	0	0	1	0	1	1
33	Polygon	24.751234	5.90526	24.779616	482.258674	Arabia Terra	-2339.844196	1	1	2	0	1	0	0	1	0	0	1	0
34	Polygon	23.078841	2.504987	55.682489	2435.163777	Arabia Terra	-2469.919731	1	1	2	0	0	0	0	1	1	0	1	1
35	Polygon	23.915639	1.868876	38.71999	1177.501208	Arabia Terra	-2507.360645	1	1	2	0	0	0	1	1	1	0	1	1

Figure 2.1.: The attribute table in ArcGIS shows the ID and the SHAPE. These attributes are standard and, therefore, to find in every attribute table. There are additional fields to specify location (LAT, LOX, REGION), morphologic features (e.g. CHANNEL, DEPRESSION, EJECTA).

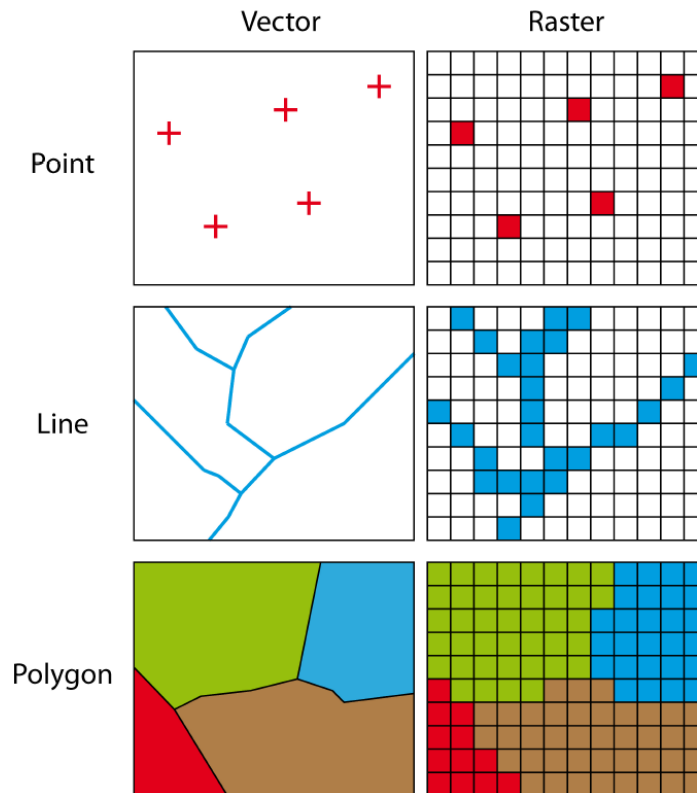


Figure 2.2.: Spatial data are represented by vector and raster data. The figure shows the different appearances of point, linear and polygon features using both data formats [Kneissl et al., 2011].

Digital images have to be included in the GIS. The data accuracy and homogeneity is essential for analyses. All information about the image should be available within the metadata of each image file [Gomasasca, 2004]. Five different working steps are essential concerning the use of data within a GIS. These general principles are data acquisition, input, processing, management, and visualization (Fig. 2.3).

For every particular task the user has to decide which data format fits best, based on the advantages and disadvantages of both formats and already available data.

## 2.4. Coordinate Systems and Projections

Coordinate systems define the position of features (point, line, and polygon) on a planetary surface in relation to a reference system. The knowledge about coordinate systems is fundamental for working with datasets in a GIS. For instance, georeferencing, transformation, integration and analysis of data are related to the coordinate systems [O'Sullivan and Unwin, 2010].

Geographic coordinate systems define the location of features on a reference body in three dimensions [Gomasasca, 2004]. On planetary surfaces latitude lines are running parallel to the equator and range from  $0^\circ$  at the equator to  $+90^\circ$  at the north pole and  $-90^\circ$  at the south pole. Meridians are half a longitude line and run from pole to pole, the values range from  $0^\circ$  at the prime meridian to  $180^\circ$  eastwards and  $-180^\circ$  westwards. Alternatively the longitude can be measured from  $0^\circ$  to  $360^\circ$ . Latitude and longitude are measured in angles and not in distances. As a result their values are expressed in degrees, minutes and seconds. The surface of a planetary

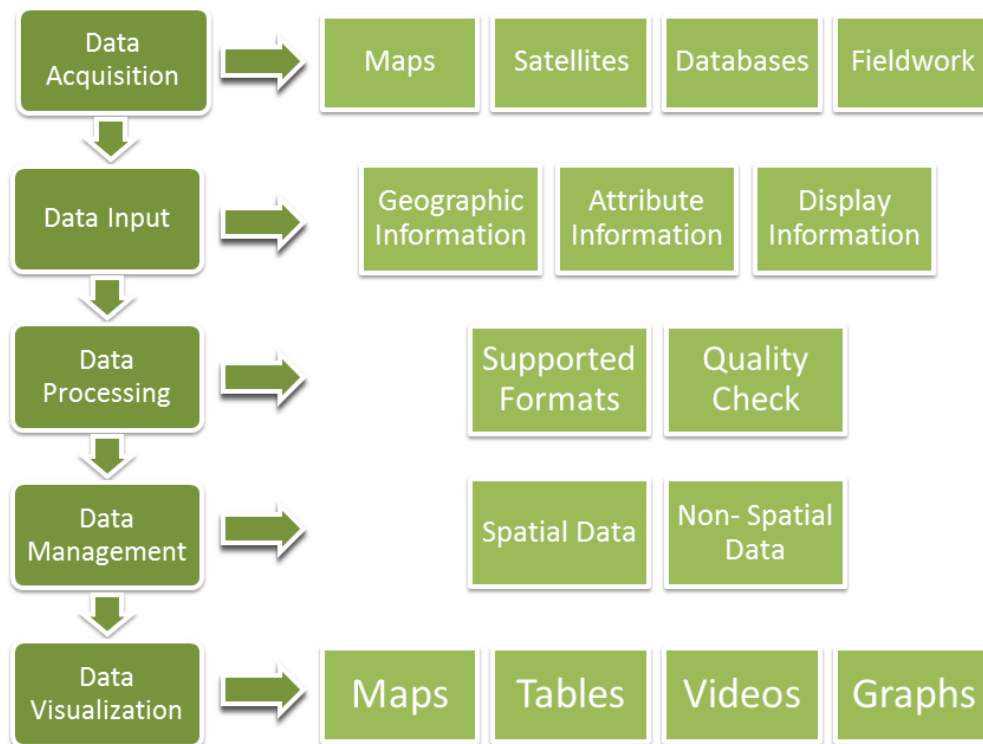


Figure 2.3.: Schematic overview of image data processing for a GIS. Data acquisition is the first working step. Existing data regardless of the format should always be included in this step. Remote sensed data obtained by airplanes or satellites are an important data source. Furthermore, fieldwork can provide high quality data for a small area. All data need to be transformed into an appropriate format that is supported by GIS, hereby the georeferencing of data is essential. The data input can be divided into geographical, attribute and display information. The transformation into GIS-supported formats and a quality check are part of the data processing and are also used to elaborate the input data. Data management is required for a coordinated storage of image data. Thus, the DataBase Management System (DBMS) is an important tool to handle spatial and non-spatial data. After the analysis the visualization in form of maps, tables, graphs or videos can be conducted (modified after Gomarasca [2004]).

body is used for referencing latitude and longitude. Thus, it is essential whether the planet is considered a sphere (rotating circle) or a spheroid (rotating ellipse). The spheroid provides a more accurate model for the Earth and is also used for Mars [Seidelmann et al., 2002]. The spheroid model requires a semi-major and a semi-minor axis. The polar radius describes the minor axis, correspondingly the equator defines the major axis of the reference body. However, some remotely sensed data of Mars were processed by using a spherical reference body. The information about the reference system is included in the meta data of each image and has to be taken into account for the analysis and comparison of the data.

To show the surface of a three-dimensional body on a 2D map, it is necessary to project each feature onto a map by using analytic transformation techniques [Gomarasca, 2004]. The feature locations are systematically assigned to new positions and xy-coordinates on the map. This can be achieved in various ways, resulting in different map projections. Some information is always lost by transferring 3D

information to 2D maps. This fact results in the distortion of spatial properties such as area, angles or lengths. Equivalent (equal areas on map and in reality), isogonic (same angles between directions on the map and in reality) and equidistant (same scaling factor on map and in reality) map projections are common [Snyder and Ashworth, 1987]. The user can choose the map projection and thus, the type of distortion. Depending on the research area and question certain kinds of distortion should be avoided.

The perspective projection defines the point of view onto the map [Gomasasca, 2004]. In regard to the research area, it is advisable to use different perspectives. For observations at or close to the poles a polar perspective should be used, on the contrary a meridian perspective should be used at the equator. A perfect projection does not exist, the projection needs always be adapted to the research area and aim [Snyder and Ashworth, 1987].

## 2.5. Data Analyses in GIS

Data analysis is an important part of the GIS. Planetary data can be analyzed in several ways, after mapping out the surface features of interest. Unfortunately, the symbology used for planetary mapping is rather incomplete. Research on this topic has been done by Nass et al. [2010, 2011a,b]. A symbol catalogue for planetary features has been developed and was used for our research. Obtained information can be measured, calculated and classified regarding to their attributes or location. The analyzing possibilities depend on the used GIS. JMars and ArcGIS do not pursue the same research foci, hence support different types of analyses.

### 2.5.1. Measurements

Both GISs provide a measuring tool. The projection and coordinate system is of high importance for measuring length, areas and angles within a map, as they are able to distort the measurements. Consequently, measurements should not rely on the map projection of the used image data, but on the geographic reference system.

Within JMars the map is always shown in a cylindrical projection, which can be re-centered at any given coordinates [Christensen et al., 2004]. The measurements are conducted by using the Martian geographic coordinate system, resulting in little distortion of the measurements.

The Crater-Tool software was developed for ArcGIS by Kneissl et al. [2010]. It is a user-friendly toolbar that can be implemented into ArcGIS. The software is mainly used for Crater Size Frequency Distribution (CSFD) measurements and provides an input for the Crater Stats software developed by Michael and Neukum [2008], Michael and Neukum [2010]. The tool re-projects the measured areas and lines into individual stereographic and sinusoidal map projection to provide higher accuracy for determining crater sizes and therefore, ages [Kneissl et al., 2010].

### 2.5.2. Calculations

Calculations are conducted easily for any information in an attribute table.

JMars offers several calculation options within the column editor. Equations can be inserted there and afterward conducted for the attribute table. Equations can be also included into scripts and run through the script window.



ArcGIS provides also two options to conduct calculations. Equations can be inserted into the field calculator. Constants, functions, or values from numerous fields in the table can be included in the equations. It is also used for conversions of units and ratios. Similar to JMars, equations can be used within scripts.

### 2.5.3. Attribute & Spatial Analyses

Within a GIS, the user finds objects of interest based on attributes, as well as spatial relationships, leading to an integrated analysis.

The user can select objects of interest manually in ArcGIS and JMars. A manual selection is useful for obtain a cursory overview or selecting only a few objects. Automated queries are faster and more precise, depending on object location or attributes.

In JMars Structured Query Language (SQL) expressions in the script window help to conduct automated selections, these are attribute related. The selected features are marked in the table and map. Spatial queries are not implemented in the software, yet.

The attribute analysis is a group of tools used to manage the attribute table within ArcGIS (Fig. 2.4). The attribute query helps to analyze, edit, and reorganize information and are found within ArcGIS in the select by attribute function. This query function allows to selectively research data concerning all of the available attributes within the table. Binary logical computation laws are used for the queries [Gomasasca, 2004, O'Sullivan and Unwin, 2010]. These allow the user to combine and compare different attributes. Attribute table searches are based on Boolean (true/false) principles [Gomasasca, 2004]. Queries need to be written in SQL or with the Query Wizard integrated into ArcGIS. After a query is specified, features are selected that meet the conditions. Spatial relationships of surface features are crucial for geological analyses. These relationships use the object coordinates within the GIS and, therefore, are based on the geometry of the layers. The user conducts spatial queries to find locations that satisfy specific requirements. Thirteen different approaches are integrated into ArcGIS. They are found in the select by location function [ESRI, 2013]. The toolbox within ArcGIS contains important and fundamental tools for spatial data analysis. There are four main tool sets that are used to extract information, to overlay data, to conduct proximity analysis and to view statistics. In the following section I will describe these tool sets in detail and present the most used tools and their applications.

Extract is a helpful tool to reduce the amount of data in a project. That provides a focus on only required information for the research. The user selects the required data based on spatial or attribute queries. The selected data is stored in a new feature class and attribute table. This is the output of the extraction. Clip allows for a spatial selection of data. The user chooses a specific, already existing feature class or a randomly shaped feature to extract all of the data that is covered by the shape. This tool is applied when the user wants to focus on a certain region within the investigation area. An alternative to the clip tool is the selection tool. A selection is done within the attribute table, or by using a query regarding the attributes of interest. Thus, this tool provides an extraction based on attributes rather than shape or spatial coordinates. Selection is applied when research only focuses on specific information of the available data.

Overlay allows for the overlay of multiple features when performing detailed analyses. This tool produces new feature classes by combining or removing common

information from the overlaid data. There are various types of overlay operations. Union creates a new feature class with all attributes and information of the combined feature classes. This tool is used to gather information from different feature classes into a single, new feature class. The operation intersect generates a new feature class. Instead of storing all of the data of the input features, only the overlapping area and their attributes are output to the new feature class. This tool is used to gather information of all available datasets in a selected area. Erase creates a new feature class that excludes where features are overlapping. For answering specific research questions, it is sometimes necessary to remove certain areas and all related information.

Major research questions within the GIS frequently pertain to the spatial distribution of features, including distances and neighborhood analyses. Various proximity tools exist within the ArcToolbox for addressing these questions. The buffer creates zones surrounding features (points, lines, or polygons). The size of these buffer zones can be set to an absolute distance or can vary depending on the size of the feature. This tool can be used to visualize the areal extent that has been influenced by adjacent surface features or processes. The statistical toolset provides standardized statistical analysis. This includes mean, minimum, maximum and standard deviation values. These values are available for the attribute table of each feature class, as well as for selected records. The information is accessed by the operation statistics. The user can also store selected information within a new attribute table by using the summarize operation.

## 2.6. Automated Systems

Automation is an important aspect of a GIS and data analysis. Part of the automation of tools is also the combination of several tools to perform more complex analyses.

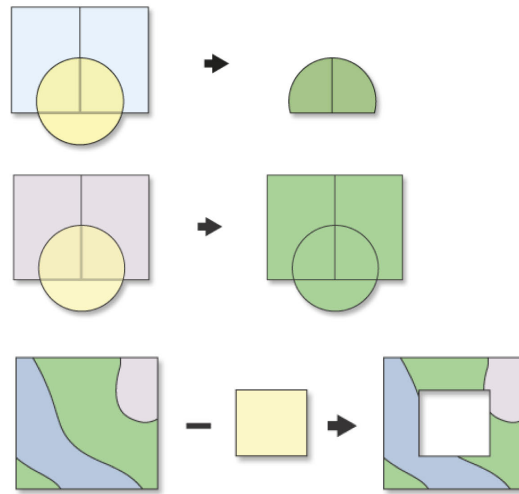
### 2.6.1. ModelBuilder

The ModelBuilder within ArcGIS can be used to create a blueprint of the analysis. The ModelBuilder is a graphical interface for creating models regarding spatial analysis problems. The operation tool, including all necessary values, can be chosen, whereas the input and output format need to be defined in the blueprint. ArcGIS will automatically carry out the predefined procedures. The advantage of using ModelBuilder analysis is the ease of repetition and the change of spatial analysis. That is, parameters and input data can be changed and every analysis can be repeated without reconstructing an entire workflow [ESRI, 2013]. Users can automate their work by using models and the ModelBuilder in ArcGIS. One step further would be the use of Expert Systems, which are described in the next section.

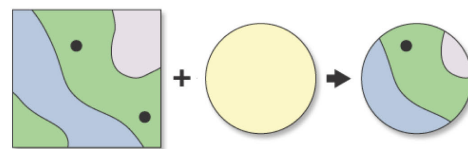
### 2.6.2. Expert Systems

An expert system is a computer system that has the decision-making ability of an expert regarding specific research topics. An expert system allows the user to automatically analyze and interpret vast amounts of data, providing detailed quantitative analyses of surface features. Furthermore, for operating the system no specific knowledge is necessary [Gomarasca, 2004].

### Overlay Tools: Intersect, Union, Erase



### Extract Tool: Clip



### Proximity Tool: Buffer

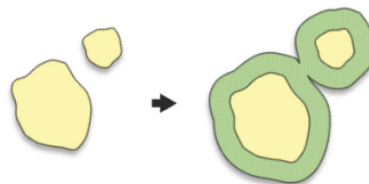


Figure 2.4.: Example of Extract, Proximity and Overlay Tools. These tools are available within the ArcToolbox (after ESRI [2013]).

Since the system operates automatically, the quality of output data is dependent on the quality of input data. The system needs as much information as is attainable in order to make appropriate choices and analyses. The expert system organizes the data in three levels. The first level is the input data, which consist of geographical, attribute, and display information. These provide the basis of the analysis. On the second level, the rules for the management and operations are defined. These rules must be programmed and included into the GIS. Finally, the third level is the control procedures performed by the user. The results of the analysis are presented in detail to the user with classification and interpretations suggested by the expert system. The user can modify the results, interpretations, classifications, and calculations at any time.

The expert system provides several advantages. The data analysis follows set rules and classifications and thus provides objective and repeatable results. Large quantities data can be easily analyzed and compared. This is essential for global

research studies. Furthermore, automated software drastically reduces the time required to produce results.

Expert systems have disadvantages concerning the quality of results. The system operates based on the provided input data and rules set up by the programmer. The quality of input data and the rules directly influence the quality of output data. For some research the expert system might not be feasible, due to a lack of background knowledge or precision for that research. This leads to no specific rules and commands within the second level of the expert system. The expert system cannot operate without these rules.

An approach for automated data management, analyses, and interpretation is included in ArcGIS. The expert system is called Virtual GIS (VGIS). This GIS is designed to help users that are not trained or specialized in GIS operations, to conduct complex analysis functions for large amounts of data. A user friendly Graphical Users Interface (GUI) is designed to support the user regarding data management, such that the focus is set on the research, itself. The analysis includes observations, calculations, and classifications. A workflow of processes, ranging from elementary GIS functions to specific calculations and classifications, is provided for the user. The software will execute the analysis operations where the required input data are available [Gomasca, 2004].

## 2.7. Databases

Databases are organized computer-based collections of data that allow the management of these data including insertion, modification, retrieval, and deletion of data. A database is always an abstract representation of the real world and hence can never contain all elements of the real world. Nevertheless, they provide organized and structured data and yield the following advantages:

- Reliability: consistent services without interruptions are provided.
- Correctness and Consistency: the internal logic is proofed and correct.
- Technology: the DBMS-software is independent to the system and not effected by e.g. updates.
- Security: protection against loss and unauthorized read is guaranteed.

Databases are structured in three levels. The external level is the users view and only contains limited access to the database structure. The user is supported by an operation-interface controlled by a DBMS, which simplifies the management of the database itself. The conceptual level is the storage and organization structure of the data. Within the internal level the aspects of physical data storage can be found, the standards are defined by the American National Standards Institute (ANSI) and the Standards Planning and Requirements Committee (SPARC) [Worboys, 2004].

A certain type of database is the spatial database systems. They can handle geospatial data including geometric and topological operations and queries. They also support the use of raster data [Kresse and Danko, 2012]. Databases support four main data models: hierarchical, relational, networks and object oriented [Gomasca, 2004].

For this research a database with the relational data model is used. The data are stored within a table that exists out of rows and columns. The features in the table

represent an entity of the real world, which can be characterized by the following attributes:

1. Identifier: It is used to clearly identify the entity. A name, number, or label are often used as identification.
2. Position: It is essential for locating the entity. Information about the coordinates (numerical or cartesian), but also the projection type is stored.
3. Attributes: They characterize the entity regarding different parameters (slope, color and structure).
4. Behavior and Function: It shows the behavior (spectral information) and the function (deposition area) of the entity.
5. Spatial Properties: They include data about the size, perimeter, diameter and volume about an entity.

Every feature is assigned to a row and several columns of the table. The attributes, position and spatial properties are stored within these columns. Of high importance is the identifier, which is the primary key in the table and helps to link different tables. A table can be joined partially or entirely to another table within the GIS to provide an increase of information. Besides the already mentioned information types, meta data (e.g. information about instruments, type of documentation, accuracy) can be included in the table.

The information stored in the database can be seen in the attribute table of each shapefile. Features on the map are linked to the information in their attribute table. This allows the user to gather and change information for each feature in the table.



## 3. Data and Data Processing

Images obtained by remote sensing are the basis for the analysis and interpretation of the Martian geology and geomorphology. Remote sensing is described in this chapter, including spacecraft, scanning systems, spectral principles and types of resolution. The image data are published in the raw format. The data quality, pre-processing, and processing software are shown for the used image data. The image data were obtained by different instruments, which will also be introduced in this chapter.

### 3.1. Remote Sensing

Remote sensing offers the identification of objects and the analysis of dynamic surface processes. The quality of digital data has dramatically improved over the last decades because of increased geometric, temporal, spatial, radiometric and spectral resolution. Even for Earth observations remote sensing is of prime importance. A global view provides new insights and information about short and long term changes of planets. Such images are obtained from surfaces, satellite, aerial and ground platforms. For planetary research mainly satellite platforms are available. 41 planetary missions to Mars have been undertaken in the last 50 years (Tab. 3.1). Rover and lander missions on Mars provide ground truth data only for specific sites. Therefore, the obtained remote sensing data need to be reliable and of high quality. Spacecraft orbiting planetary bodies in a certain distance allow observation of surface, atmospheres, gravity, and radiation parameters by various instruments. Each instrument and sensor focus on a specific topic, developed for answering a certain research question. All separately collected information needs to be taken together to obtain a complete dataset. This needs to be analyzed to investigate surface processes and conditions of planetary bodies. Remote sensing does not collect direct information about the environment of planetary bodies. Instead it provides unique electromagnetic values, that needs to be converted and processed further to obtain information on object identification, object properties and spatial arrangements [Gomasasca, 2004, O'Sullivan and Unwin, 2010].

#### 3.1.1. Scanning Systems

A spacecraft in a defined orbit facilitates the acquisition of digital images. Series of surface stripes in one or more bands (depending on the instrument) are conducted. The instruments that measure electromagnetic radiation are called sensors. They are divided into active and passive sensors. Active sensors have a built-in source of radiation, examples are radar (radio detection and ranging) and lidar (light detection and ranging). Passive sensors do not have an own source of radiation. They only collect reflected sunlight or emitted thermal energy. The Charge-Couple-Device detector (CCD) is the most used passive sensor (e.g. Jong and Van der Meer [2004]).

Two different mechanisms for the data acquisition are mainly used and are presented in detail. Whisk Broom and Push Broom Sensors are both able to gather

Number	Spacecraft	Launch	Mission Type	Nation	Success/ Failure
1	Marsnick 1	10.10.1960	Flyby	UdSSR	Failure
2	Marsnick 2	14.10.1960	Flyby	UdSSR	Failure
3	Sputnik 29	24.10.1962	Flyby	UdSSR	Failure
4	Mars 1	01.11.1962	Flyby	UdSSR	Failure
5	Sputnik 31	04.11.1962	Flyby	UdSSR	Failure
6	Mariner 3	05.11.1964	Flyby	USA	Failure
7	Mariner 4	28.11.1964	Flyby	USA	Success
8	Zond 2	30.11.1964	Flyby	UdSSR	Failure
9	Mariner 6	24.02.1969	Flyby	USA	Success
10	Mariner 7	27.03.1969	Flyby	USA	Success
11	Mars 1969A	27.03.1969	Lander	UdSSR	Failure
12	Mars 1969B	02.04.1969	Lander	UdSSR	Failure
13	Mariner 8	08.05.1971	Orbiter	USA	Failure
14	Cosmos 419	10.05.1971	Orbiter, Lander	UdSSR	Failure
15	Mars 2	19.05.1971	Orbiter, Lander	UdSSR	Failure
16	Mars 3	28.05.1971	Orbiter, Lander	UdSSR	Failure
17	Mariner 9	30.05.1971	Orbiter	USA	Success
18	Mars 4	21.07.1973	Orbiter	UdSSR	Failure
19	Mars 5	25.07.1973	Orbiter	UdSSR	Success
20	Mars 6	05.08.1973	Lander	UdSSR	Failure
21	Mars 7	09.08.1973	Lander	UdSSR	Failure
22	Viking 1	20.08.1975	Orbiter, Lander	USA	Success
23	Viking 2	09.09.1975	Orbiter, Lander	USA	Success
24	Phobos 1	07.07.1988	Orbiter	UdSSR	Failure
25	Phobos 2	12.07.1988	Orbiter	UdSSR	Failure
26	Mars Observer	25.09.1992	Orbiter	USA	Failure
27	Mars Global Surveyor	07.11.1996	Orbiter	USA	Success
28	Mars 96	19.11.1996	Orbiter, Lander	Russian Federation	Failure
29	Mars Pathfinder	04.12.1996	Lander, Rover	USA	Success
30	Nozomi	03.07.1998	Orbiter	Japan	Failure
31	Mars Climate Orbiter	11.12.1998	Orbiter	USA	Failure
32	Mars Polar Lander	03.01.1999	Lander	USA	Failure
33	Mars Odyssey	07.04.2001	Orbiter	USA	Success
34	Mars Express	02.06.2003	Orbiter, Lander	Europe	Success
35	MER Spirit	10.06.2003	Rover	USA	Success
36	MER Opportunity	07.07.2003	Rover	USA	Success
37	MRO	12.08.2005	Satellite	USA	Success
38	Phoenix	04.08.2007	Lander	USA	Success
39	Ying Huo 1	08.11.2011	Orbiter	China	Failure
40	Phobos- Grunt	08.11.2011	Sample Return	Russia	Failure
41	MSL	26.11.2011	Rover	USA	Success

Table 3.1.: Missions to Mars in chronological order from 1960 to 2013.



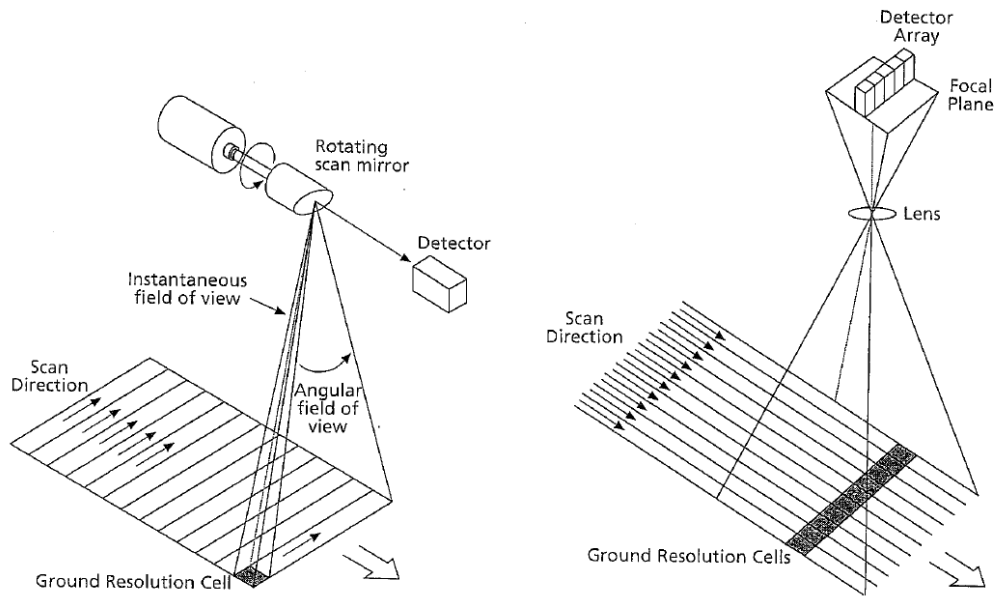


Figure 3.1.: Principles of whisk broom scanner (left) and push broom scanner (right)[Jong and Van der Meer, 2004].

information in series along an array [Jong and Van der Meer, 2004]. The punctual scanning system collects data pixels (Fig. 3.1). A rotating mirror is used to scan the surface within the field of view perpendicular to the direction of the sensor. A second mirror is reflecting the light into the CCD detector. One detector is used for this scanning system. The images need to be pre-processed due to the spatial distortions occurring by the mirrors. These scanners are also used to focus on one part of the array, observing that area in more detail by stopping the scan. The linear scanning system is built up of an array of CCD detectors. The surface is scanned line by line (Fig. 3.1). Due to the use of color filters- red (R), green (G), blue (B)- a complete RGB chromatic acquisition can be achieved simultaneously.

The reflected energy of the surface is measured and stored as a numerical value in form of Digital Numbers (DNs). They represent the level of radiance of certain surface units. By using color filters the sensors are sensitive to radiation at certain wavelengths.

### 3.1.2. Spectra

Every object on a planet scatters, absorbs or reflects solar radiation and emits thermal radiation in a characteristic way according to the chemical, structural and chromatic properties of the object. These radiation principles are used by various instruments. They are operating in the optical reflected and emitted wavelengths, characterized by different spectral intervals (Fig. 3.2). The spectrum ranges from ultraviolet to microwave. Each band is used to study different surface features.

### 3.1.3. Resolution

Resolution is also called Level of Detail (LoD). Remote sensing systems have spectral, spatial, temporal, radiometric and geometrical resolution. Spectral resolution is the sensor capability to resolve details in the spectral signal by the energy mea-

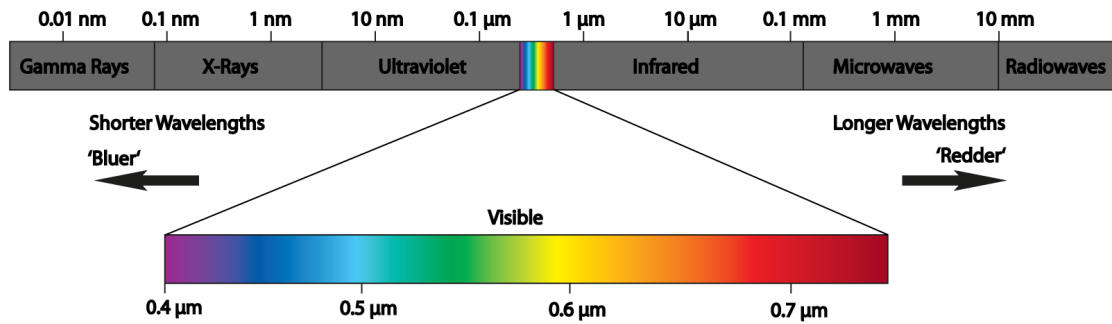


Figure 3.2.: The electromagnetic spectrum (after Hartmann [1985]).

sured within each spectral band of the sensor. If the spectral resolution is too low important information about spectra characteristics are lost, resulting in potential misinterpretation of object composition and properties. Spatial resolution is often equated to the field of view (FOV). It is defined as the area on the ground which is viewed by the instrument. This area depends on the altitude of the spacecraft and varies by decreasing or increasing orbit altitude. Depending on the type of research different resolutions are essential. High resolution is useful for detailed surface observations. Low resolution is sufficient for conducting global research. Temporal resolution defines how often the same area is captured by a sensor. It is essential for the observation and analysis of dynamic systems (e.g. atmosphere) and for detecting surface changes (e.g. liquid water). Radiometric resolution or sensitivity depends on the amount of DN, which are recorded by the sensor. These numbers are representing different grey values. More surface details are visible if the DN is high. The radiometric resolution is usually given in bits (4 bits = 64 grey levels, 8 bits = 256 grey levels, 16 bits = 1064 grey levels). Geometric Resolution is defined by the ground size of the pixels. Detailed concepts of spatial, spectral, temporal and radiometric resolution are discussed by Joseph [2000], Mather and Koch [2011] and Lemmens [2011]. The resolution can vary from centimeters to kilometers, based on the sensor, orbit and type of observation. High resolution allows observing more surface details, but is very time consuming. Low resolution helps to investigate global research by providing global coverage of data. Maps with a scale larger 1:50,000 are provided by geometric resolution of 10-200 m/pix. With a resolution of 0.5-10 m/pix more detailed maps with a scale up to 1:5,000 are generated [Gomasca, 2004, O'Sullivan and Unwin, 2010].

## 3.2. Data Processing

Images are built up by pixels and are described in a three-coordinate system with x and y locating each pixel and z giving the DN and therefore, an intensity value. The recorded information has to be transmitted in electronic form from the spacecraft to a station on Earth. The data are processed from these electronic values into physical units, developing digital images (Fig. 3.3).

The data processing is divided into different steps:

1. Web-based dataset search
2. Selection of needed image data
3. Processing and combination of individual images to form mosaics

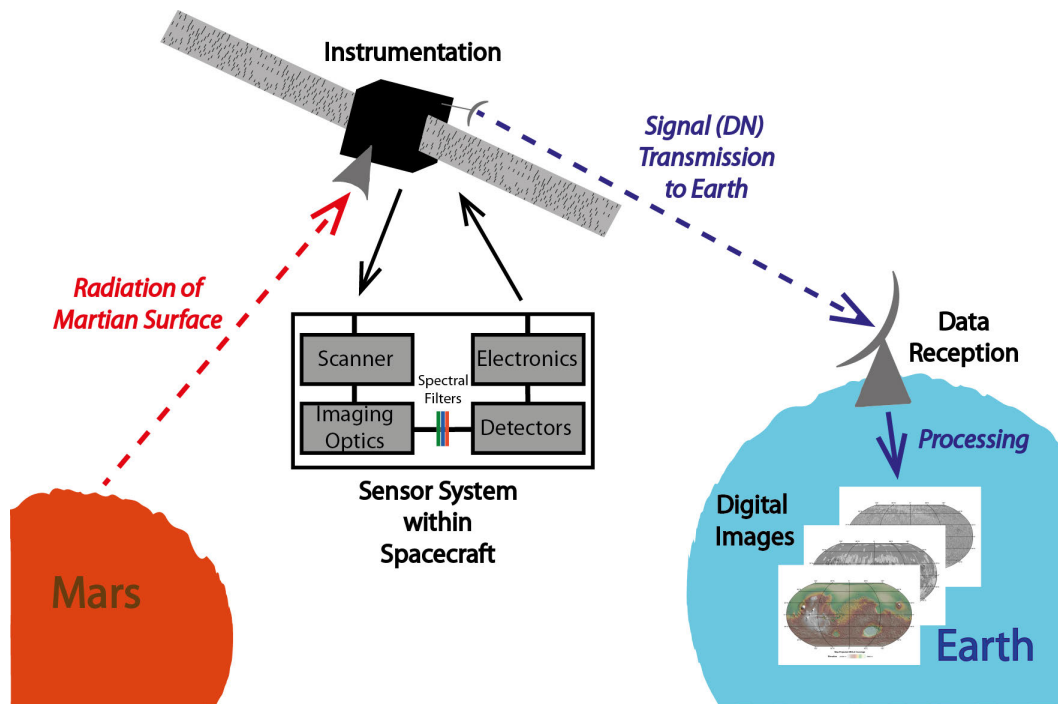


Figure 3.3.: Sketch of remote sensing principles. Radiation of planetary surfaces is collected by sensors on spacecrafts. The sensor system on board the spacecraft is divided into scanner, imaging optics, several spectral filters, detector and electronics. This instrumentation converts the collected radiation data into DN's, which are transmitted to Earth. After the data reception the information will be processed into digital images.

4. Adapting all data to one reference system to ensure comparability and combination of data
5. Import into a GIS that allows analysis and interpretation of data

The data flowchart, including instruments used is shown in Fig. 3.4.

### 3.2.1. Data Quality

The obtained data need to be checked for data quality. All observations contain errors and inaccuracies [Wolf and Ghilani, 1997]. Minimizing the impact of errors or even their occurrence is the principal object to ensure the quality and reliability of data. Errors are described in terms of accuracy and precision. In order to receive reliable data, errors need to be detected and removed - if possible - from the measurements. Detailed classification on error classes, concepts for error recognition and systematic mathematical procedures to determine errors are described in Lemmens [2011] and Wolf and Ghilani [1997, 2006]. The quality of geographical information includes the quality at surveying raw data, but also processing these data [Lemmens, 2011]. The accuracy and precision of the used data need to be known. If errors are present in the input data, they will propagate to the output as well. The pre-processing of image data helps to minimize occurring errors.

### 3.2.2. Pre-Processing

Generally pre-processing of the image data is performed to correct:

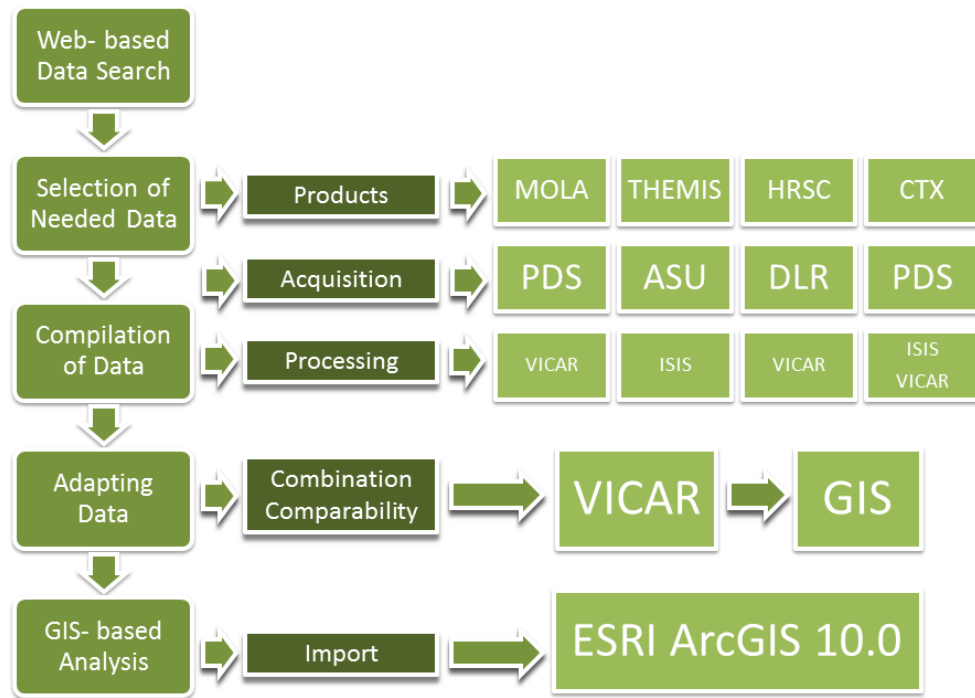


Figure 3.4.: General workflow of data search, available products, acquisition and processing of image data by using different sources and software systems.

- image radiometry
- geometric distortions
- sensor noise
- formatting to standard prescription

These basic corrections are usually necessary due to changes in terrain illumination, viewing geometry, atmospheric conditions and sensor characteristics [Jong and Van der Meer, 2004, Mather and Koch, 2011, Richards, 2013, Schowengerdt, 1997]. The user must be aware of the geometrical properties of the data, because there is no fixed schedule or rule for image pre-processing.

The image processing is split up into four levels:

1. Reformatted raw data
2. Sensor- corrected data (geometric & radiometric corrections)
3. Scene- corrected data (geometric & radiometric corrections)
4. Geophysical data

Specific software is used for the processing. However, each level requires more data and processing than the previous one. Not all raw data are processed into higher levels, due to the effort of time and costs involved [Schowengerdt, 1997].

Instrument	Mission	Resolution	Spectral Range	Coverage
MOLA	MGS	463 m/pix (global), 2 m vertical resolution	1,064 $\mu m$	100 %
TES	MGS	3,000 m/pix	6 - 50 $\mu m$	100 %
THEMIS IR	MO	100 m/pix	6,600 - 14,960 $\mu m$	98 %
HRSC	MEX	10 m/pix (nadir), 50 m/pix (DTM), 10 m vertical resolution	0.400 - 0.995 $\mu m$	39 %
CTX	MRO	6 m/pix	0.500 - 0.700 $\mu m$	75 %

Table 3.2.: Overview about instruments, missions, resolution, spectral range and coverage in 2013.

### 3.2.3. Data Processing Software

The compressed and unregistered raw data can be processed by using two different software systems. They are concurring with each other, but they are also complementary in certain aspects. Both systems are used to get required image formats and projections. The Integrated Software for Images and Spectrometers (ISIS) system is developed and supported by the U.S. Geological Survey (USGS) and open source [Eliason et al., 2001, Gaddis et al., 1997]. The second software is the Video Image Communication and Retrieval (VICAR) system. Licenses are distributed by the developer of the National Aeronautics and Space Administration (NASA) and the Jet Propulsion Laboratory (JPL), which is also responsible for the support and administration [Anderson and Mann, 1989, Hockey and Barnet, 1994]. Both systems are based on UNIX/ Virtual Memory System (VMS)- based command line routines. The software systems can be used to develop applications and scripts based on research topics and certain needs. All obtained data were processed using internal routines at the German Aerospace Center (DLR) within ISIS and VICAR. The available raw image data were downloaded from web databases and transformed to the VICAR file format. The data were translated into different map projections by using the Geospatial Data Abstraction Library (GDAL). It is a free available library for geospatial data formats that processes data into the required projection mode [GDAL, 2013]. The raw data are processed into JP2000 files, which than can be imported to ArcGIS. Images of selected instruments of four different Mars missions were used for this study.

## 3.3. Instruments

The missions and the instruments used for this research, are presented and explained in the following section. Additionally, an overview about the used instruments is shown in Tab. 3.2.

### 3.3.1. Mars Orbiter Laser Altimeter (MOLA)

The Mars Global Surveyor (MGS) was launched on November 7, 1996. The goal was to orbit Mars and map it over the course of approximately three years. The last contact was on November 2, in 2006. The Mars Orbiter Laser Altimeter (MOLA)

was one of the instruments on board of the spacecraft [Smith et al., 2001]. The primary goal of MOLA was to achieve a global digital terrain model (DTM) of Mars.

The instrument operates within a wavelength of  $1,064 \mu m$  and measures the distance between the spacecraft and the Martian surface with an infrared laser pulse. Vertical resolutions of 30 meters on an absolute scale and up to 2 meters on a relative scale have been obtained [Smith et al., 2001]. Single MOLA tracks provide topographic profiles along the track direction. All individual MOLA tracks can be merged together by using the Mission Experiment Gridded Data Record (MEGDR) to form a global map with a resolution of 128 pix/degree in mid-latitudes and up to 256 pix/degree in polar regions [Smith et al., 2001]. The accuracy of the DTM in regions of interest can be improved further, including the topographic point data of single MOLA tracks, by using the Precision Experiment Data Records (PEDR) [Smith et al., 2001].

Within two years of the mission approximately 588 million individual topographic measurements were made. MOLA achieved global coverage and provides a basis for processing of other image data (Fig. 3.5).

The data are available as 30 quadrangle maps covering the entire planet. The images are already converted from the Planetary Data System (PDS) format to VICAR files to simplify further processing. The processed terrain model can be imported into GIS environments and used for studies in geophysics, geology, geomorphology and atmospheric sciences.

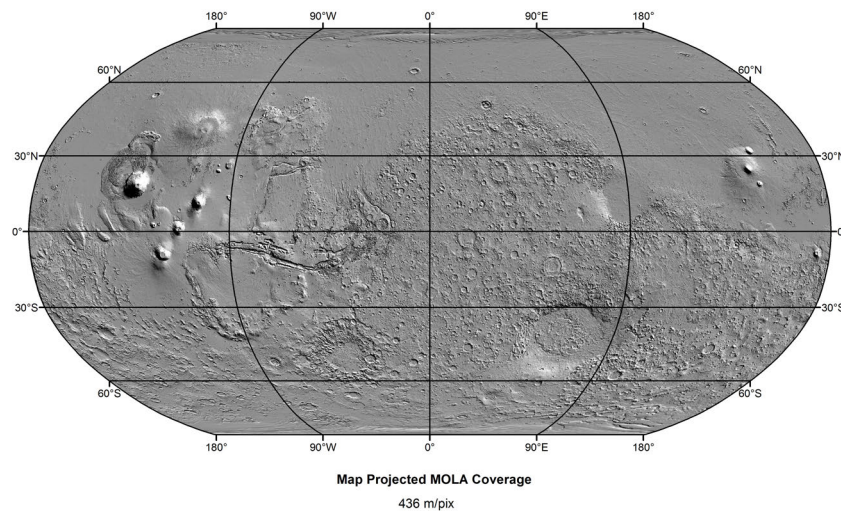


Figure 3.5.: Global MOLA map by using 588,000,000 MOLA PEDR ground measurements.

### 3.3.2. Thermal Emission Spectrometer (TES)

TES is also located on board of the Mars Global Surveyor. The purpose of this instrument is to determine the surface composition of minerals, rocks and ices on Mars, with focus on the polar regions. It was also gathering thermal information of the surface and the atmosphere [Christensen et al., 2001].

TES can be divided into an interferometer, a broadband radiance sensor and a solar reflectance sensor. These instruments allow measuring the incoming infrared

and visible energy. The interferometer covers wavelengths from 6 to 50  $\mu m$ . The broadband sensor operates in wavelengths ranging from 5.5 to 100  $\mu m$ . The brightness of the reflected solar energy is measured by the third sensor in a wavelengths of 0.3 to 2.7  $\mu m$ . TES obtains a spatial resolution of 3000 m/pix [Christensen et al., 2001].

Within two years a total number of 206,219,475 spectra were collected. ASU was in charge of the instrument and is managing the data release. Several global maps of Mars have been produced by using TES data. They provide insights about mineral composition, albedo, thermal inertia and temperature of the Martian surface.

The image data can be downloaded from PDS or directly from the ASU homepage, where global data sets of Mars are available in various file formats. The TES image data provide important information for global research on Mars.

### 3.3.3. Thermal Emission Imaging System (THEMIS)

Mars Odyssey was launched on April 7, 2001 and arrived at Mars 7 months later, due to the short distance between Mars and Earth at that time. The Thermal Emission Imaging System (THEMIS) on board of this spacecraft investigates the surface mineralogy and morphology of Mars [Christensen et al., 2004].

One part of the instrument is an imager (THEMIS-VIS). A resolution of 18 m/pix can be achieved by using five color bands centered at wavelength of 0.423  $\mu m$ , 0.553  $\mu m$ , 0.652  $\mu m$ , 0.751  $\mu m$  and 0.870  $\mu m$ . The thermal infrared imager (THEMIS-IR) operates in 9 bands at wavelength of 6.62  $\mu m$ , 7.88  $\mu m$ , 8.56  $\mu m$ , 9.30  $\mu m$ , 10.11  $\mu m$ , 11.03  $\mu m$ , 11.78  $\mu m$ , 12.58  $\mu m$  and 14.96  $\mu m$ . Day and night images are available for the surface and the atmosphere with a resolution of 100 m/pix.

Until March 2013 Mars Odyssey has completed 50,000 orbits around Mars. The instrument obtained 190,694 VIS-images and 160,178 IR-images (Fig. 3.6). The ASU is in charge of the instrument and the data release. The data are released in three months intervals in form of a web catalog [Facility, 2013].

Image data are processed by using ISIS routines developed by the USGS. The radiometric calibration, mosaicking of individual images and map projecting are conducted.

### 3.3.4. High Resolution Stereo Camera (HRSC)

The European Space Agency's (ESA) Mars Express mission was launched on June 2, 2003 from the Russian space Centre at Baikonur, Kazakhstan. The mission supplies scientists with data about the geology, mineralogy and atmosphere of Mars. Seven different instruments, including a lander, are on board of the spacecraft to achieve these mission goals. The lander was lost in December 2003. The most relevant mission instrument for this research is the High Resolution Stereo Camera (HRSC) [Jaumann et al., 2007, Neukum and Jaumann, 2004].

It is a multi-sensor push broom instrument with nine CCD line sensors mounted in parallel lines operating at different angles of view. The camera operates at wavelengths ranging between 0.400-0.480  $\mu m$  (blue), 0.495-0.585  $\mu m$  (green), 0.585-0.765  $\mu m$  (nadir), 0.725-0.775  $\mu m$  (red) and 0.915-0.995  $\mu m$  (nearinfrared) [Neukum and Jaumann, 2004]. The two stereo and photometry channels are also working within a wavelength of 0.585-0.765  $\mu m$ . A resolution up to 10 m/pix is reached. The image arrays are usually 52x330 km in size [Neukum and Jaumann, 2004]. Additionally, a Super Resolution Channel (SRC) consisting of a CCD frame cam-

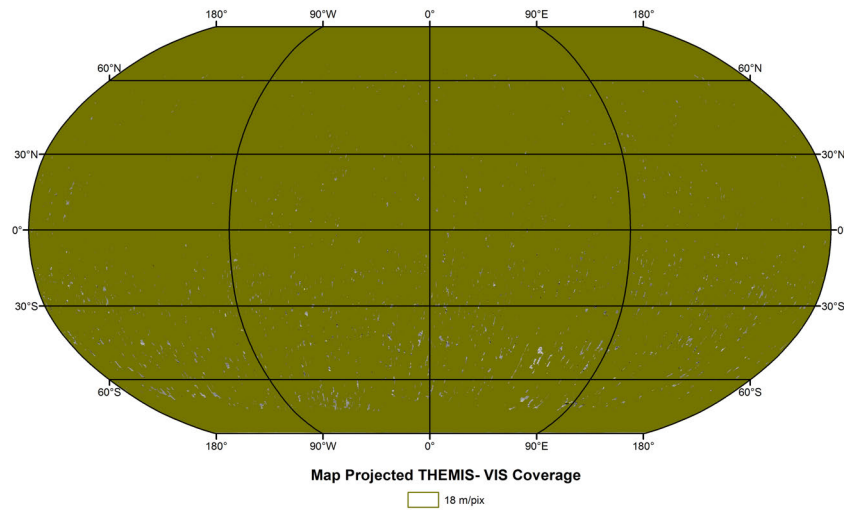


Figure 3.6.: THEMIS- VIS coverage map including 190,694 images (data source: USGS).

era provides a resolution of 2.3 m/pix [Jaumann et al., 2007]. The main task of the project is the generation of DTMs. Therefore, the different angles of view of the line sensors are essential. The two stereo and photometry channels and the nadir channel are used to obtain stereo data of the Martian surface. A resolution of 200 m/pix is achieved for each HRSC orbit by using standardized processes [Scholten et al., 2005]. Additional orientation data can improve the resolution of DTMs up to 50 m/pix [Jaumann et al., 2007].

In March 2014 orbit number 12.954 was surveyed. These data represent the level-4p images and are only available within the HRSC-team. The released level-4 data reach to orbit number 6509 and represent 40% of the surface (Fig. 3.7).

These data are pre-processed and orthorectified by using HRSC- specific VICAR routines done by DLR and the Free University of Berlin. Detailed information about the processing of HRSC images is discussed and described in Gwinner et al. [2005] and Scholten et al. [2005].

### 3.3.5. Context Camera (CTX)

The Mars Reconnaissance Orbiter (MRO) is an American space mission, operated by NASA. It was launched on August 12, 2005. The spacecraft is designed to investigate the habitability for life on Mars. Evidence of stable water on the surface in the Martian past is searched. Relevant mission instruments include the Context Camera (CTX) [Malin et al., 2007].

The camera has a field of view of 5.7 degrees and provides an image swath of approximately 30x160 km [Malin et al., 2007]. The spatial resolution from the mapping orbit at an altitude of 300 km is 6 m/pixel. The CCD line sensor includes 5064 pixels and images are taken in a wavelength between 0.500  $\mu\text{m}$  and 0.700  $\mu\text{m}$ .

About 75% of the Martian surface are covered (Fig. 3.8) at 6 m/pixel in April 2012 [Malin Space Science Systems, 2013]. CTX raw data are published within the Mars Orbital Data Explorer (ODE) of the Planetary Data System (PDS) [University, 2013].

They are processed using the software script CTXcy, developed by the DLR.



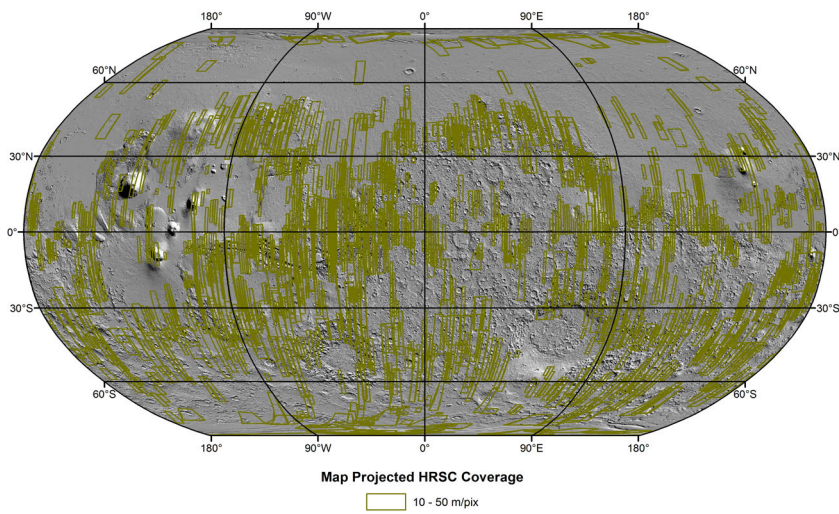


Figure 3.7.: HRSC coverage map up to March 2011 and orbit number 6509 (data source: DLR).

Routines within ISIS for the projection, VICAR to mosaic the individual images and GDAL to convert it into JP2000 were used. The final image format can be imported to a GIS.

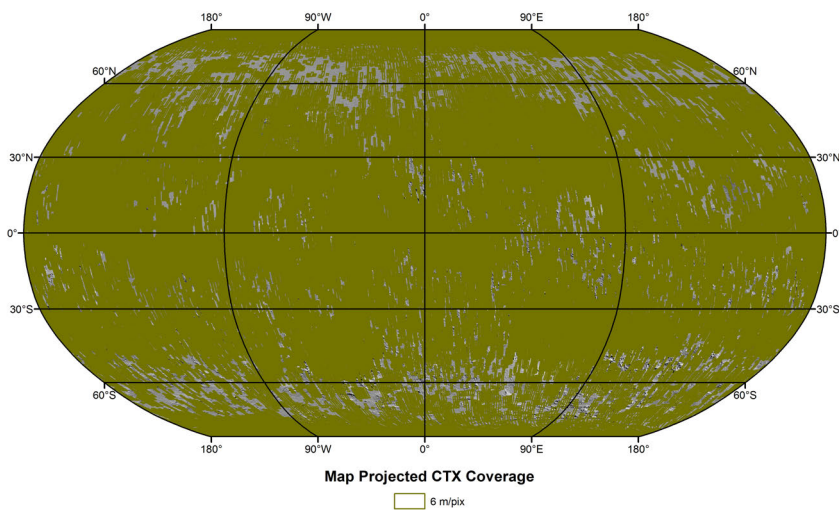


Figure 3.8.: CTX coverage map (data source: NASA).



## 4. Floor-Fractured Craters (FFCs)

In this chapter Floor-Fractured Craters are introduced in terms of discovery, research, and origin processes. They represent a surface feature that can be analyzed by automated tools.

### 4.1. Why Select FFCs?

Impact craters are ubiquitous throughout the solar system. As such, they are an ideal surface feature for which to compare planetary bodies. Floor Fractured Craters (FFCs) represent just one type of impact crater. However, these craters are characterized by the distinct appearance of their floors, which exhibit fractures, mesas, and knobs. The diverse set of surface features associated with FFCs provides the perfect data to develop semi-automated tools for planet-wide analysis. Approximately 400 FFCs have been identified on Mars [Bamberg et al., 2014, Korteniemi, 2003, Korteniemi et al., 2006]. This quantity of FFCs is adequate for developing a database and conducting qualitative analyses with semi-automated tools. The global distribution of FFCs is dispersed amongst many different environments on Mars. Thus various processes may be involved in forming the fractured floors in FFCs. In fact, there are thought to be six main origin types for FFCs on Mars [Bamberg et al., 2014]. The semi-automated tools can be adapted to provide additional information to aid researchers in determining the origin of FFCs (and perhaps other types of craters) on a global scale. FFCs are also present on the Moon [Schultz, 1976]. Consequently, semi-automated analysis on Martian FFCs can be compared to analyses of Lunar FFCs. Before tools may be developed and adapted, the intricacies of FFCs (e.g. the theories of the origin of fractures, the surface features that indicate potential origins) must first be understood so that the tools have information to operate on.

### 4.2. Discovery and Research of FFCs

FFCs were first observed on the Moon in the 1970s. Schultz [1976] investigated the distribution of 206 FFCs on the Moon and classified these structures into six different types according to their appearance and amount of fracturing. Lunar FFCs usually occur near basaltic maria and therefore, may have a volcanic origin.

Research on the global distribution of FFCs on Mars has been performed by using Viking and MOLA data [Korteniemi, 2003, Korteniemi et al., 2006]. The presence of ice in the subsurface and past existence of liquid water on the surface of Mars might have been responsible for the formation of fractures in certain regions on Mars [Andrews-Hanna and Phillips, 2007, Burr et al., 2002, Carr, 1996, Clifford, 1993, Leask et al., 2007, Manker and Johnson, 1982, Pedersen and Head, 2011, Rodriguez et al., 2005, Russell and Head, 2007, Sato et al., 2010, Schumacher and Zegers, 2011, Sharp, 1973, Zegers et al., 2010]. The origin of FFCs is still under debate. At least six different origins for the fracturing of the crater floors have been discussed, including glacial [Hiesinger and Head, 2000, Morris and Underwood, 1978,

Pechmann, 1980], fluvial [Sato et al., 2010, Zegers et al., 2010], volcanic [Brennan, 1975, Jozwiak et al., 2012, Schultz, 1976, Wichman and Schultz, 1996] and tectonic activity [Hanna and Phillips, 2006, Smrekar et al., 2004]. The morphology within the FFCs differs markedly. Fractures, knobs, depressions, linear features, volcanic units, channels, and central peaks can be observed within and around FFCs. For each model of origin, certain surface features should be (or should not be) present. Therefore, some surface features strengthen or weaken the origin models, giving hints for the possible origin process.

### 4.3. Possible Formation Processes

Based on previous research [Bamberg et al., 2014] different scenarios for the formation of FFCs are considered and described.

#### 4.3.1. Intrusive Volcanism

FFCs on the Moon are correlated with intrusive volcanism, as indicated by their distribution along the basaltic mare basin margins [Brennan, 1975, Jozwiak et al., 2012, Schultz, 1976, Wichman and Schultz, 1996]. The driving pressure of the intrusion and the crustal thickness are the most important, as well as the limiting factors for intrusive volcanism. Therefore, uplift and fracturing of crater floors are also controlled by these factors. Two formation processes have been discussed for Lunar FFCs. (1) Floor uplift due to shallow magmatic intrusion including sill formation and (2) thermally driven viscous relaxation [Brennan, 1975, Schultz, 1976, Wichman and Schultz, 1996]. The first model of magmatic intrusion (Fig. 4.1) appears to best explain the origin of FFCs on the Moon [Jozwiak et al., 2012].

Craters that are located close to volcanic areas on Mars could have a similar origin to FFCs on the Moon. Impacts lead to a reduction of crustal thickness beneath the crater. Furthermore, a zone of weakness is developed by the pressure and force of the impact [Melosh, 1989]. Magma could easily rise through this zone, which would explain the preferentially fractured crater floors rather than fractured surrounding units. Rising magma can uplift the crater floor by developing a sill or a laccolith like structure in the subsurface. A sill is a horizontal sheet of igneous rock intruded between different rock layers. A laccolith is a dome-shaped body of igneous rocks formed by intrusion of magma and forcing the overlying material into a dome shape [Press et al., 2003] and fracturing of the crater floor due to the uplift. Lava tubes, volcanic pits, wrinkle ridges in lava sheets, and uplift of the crater floor are features of a volcanically influenced region.

#### 4.3.2. Subsurface Ice

A possible formation model of chaotic terrains on Mars considers the melting of subsurface ice reservoirs. This model is supported by various studies [Burr et al., 2002, Carr, 1996, Leask et al., 2007, Manker and Johnson, 1982, Pedersen and Head, 2011, Rodriguez et al., 2005, Sato et al., 2010, Sharp, 1973]. This hypothesis has been applied to Aram Chaos [Massé et al., 2008, Zegers et al., 2010]. A subsurface ice layer melts according to the overburden material, resulting in increased temperature and pressure (Fig. 4.2). A thick layer of overburden material is essential for an insulating effect. In order to melt a subsurface ice layer the combined total thickness of the overburden material and the ice layer needs to be 3.5- 4.0 km [Schumacher and

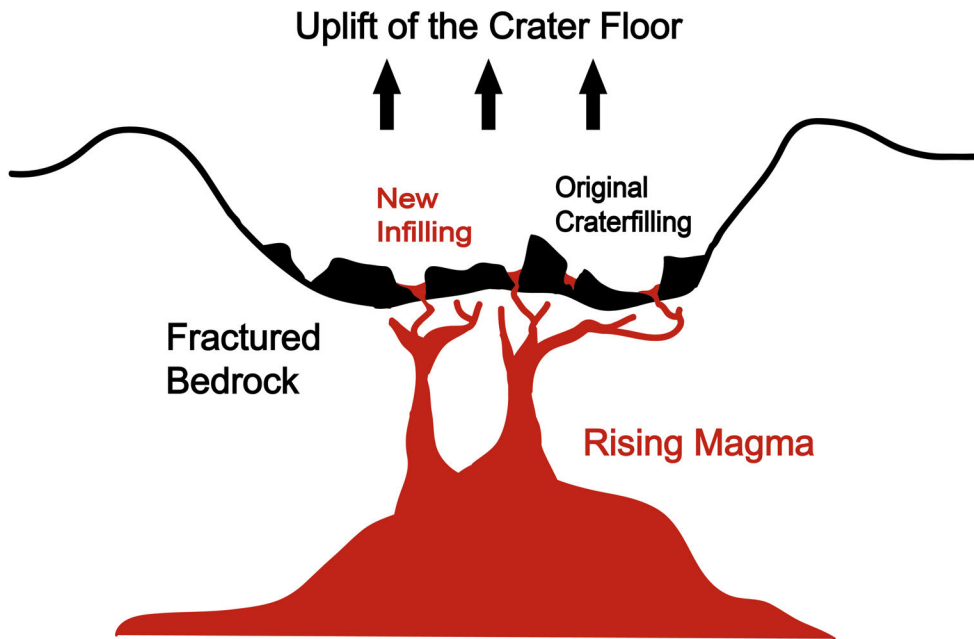


Figure 4.1.: Model of intrusive volcanism. The magma can form sills, dikes, or laccoliths. It can enter the crater and partially or totally fill the floor. These processes will uplift and crack the crater floor. This event could be repeated several times, depending on the volcanic activity of the area and driving pressure of the intrusion itself [Schultz, 1976].

Zegers, 2011]. Furthermore, Schumacher and Zegers [2011] calculated the minimum thickness of the ice layer to be 1.5 km and the maximum thickness up to 2.5 km. If the ice layer or overburden material is too thin, partial melting occurs. The crater floor will be stable until a critical mass of melt triggers outflow [Schumacher and Zegers, 2011]. However, partial melts can refreeze easily, but no evidence for this process is visible in FFCs on Mars. Volcanic activity would have an influence on subsurface temperatures. Melting in a thin ice-layer can be produced by inducted volcanic heat. Floor fracturing can also occur by the presence of water-rich or ice-rich sediments. A high porosity infilling, consisting of eroded materials and volcanic ash, can contain a large quantity of ice particles. Melting of these particles decreases the pore pressure at the surface and the layer collapses, depending on the cohesion of the material. Most of the water would evaporate, but could also produce an outflow depending on the amount of stored ice. The collapse of the layers will result in a chaotic distribution of the fractured surface. The surface exhibits irregular elevations and knobs can be shifted, tilted, and moved by the outflowing water, as observed in parts of Aram Chaos [Zegers et al., 2010]. The withdrawal in subsurface ice will also lead to polygonal fracturing of surface units without chaotic orientation of the knobs as shown by Massé et al. [2008].

### 4.3.3. Groundwater Migration

The formation of outflow channels and chaotic terrains on Mars are linked to regional or global aquifer systems [Andrews-Hanna and Phillips, 2007, Carr, 1996, Clifford, 1993, Russell and Head, 2007] and could also be an explanation for FFC formation. Earth fissuring and internal erosion, so-called seepage or piping, are the

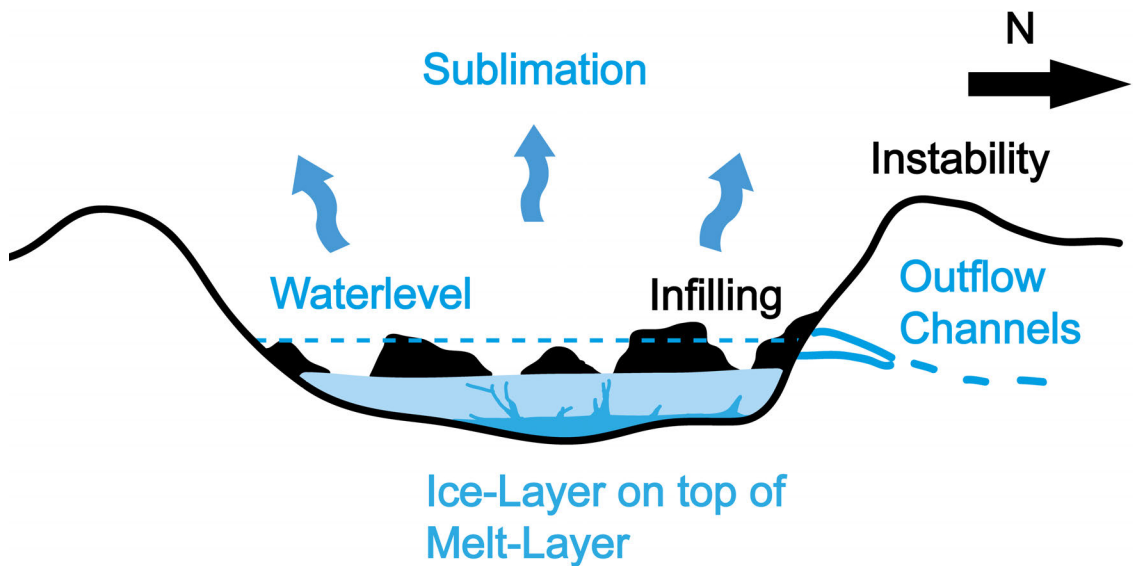


Figure 4.2.: Model of a subsurface ice-rich layer. The model was developed to explain the formation of chaotic terrains on Mars. This model can also work for large FFCs [Schumacher and Zegers, 2011, Zegers et al., 2010]. The subsurface ice layer melts due to the pressure of the overburden Material. This leads to instability and potential fracturing of the crater floor.

two main processes, triggered by an active water drainage system in the late Hesperian in the Xanthe Terra region [Sato et al., 2010]. Earth fissuring is thought to be caused by a rapid drop of the groundwater table [Budhu, 2008, Holzer and Pampeyan, 1981, Sheng et al., 2003]. Seepage and piping occur when the hydraulic gradient in the groundwater reaches a critical value. The flowing water starts to erode and transport soil particles, resulting in the formation of subsurface drainage [Watson and Burnett, 1993]. These processes are linked to the rapid flow velocity of groundwater, which could be explained by the steep slopes in some regions along the Martian dichotomy boundary [Craddock and Howard, 2002, Parker et al., 1993, 1989] and outflow channels (Fig. 4.3).

Topographic observations supporting this model are large crater diameters, deeper fractures than the original crater cavity, inconsistency in the thickness of crater infilling. The crater infilling preferentially fractures along the rim due to structural weakness and flow of groundwater. The fracturing is an ongoing process, developing toward the crater center. The degree of crater modification in the form of fracturing will vary depending on the aquifer system and the number of recharge and outflow events. Tilted blocks are seen as evidence for inhomogeneous collapse inside the crater. Pit chains are interpreted as the initial stages of Earth fissuring [Sato et al., 2010].

#### 4.3.4. Rayleigh Convection

Rayleigh convection is a type of near-surface tensile stress that can result in the development of polygonal terrain. This density-driven, free convection is a model suggested by Wenrich and Christensen [1993] and is often used to explain large-

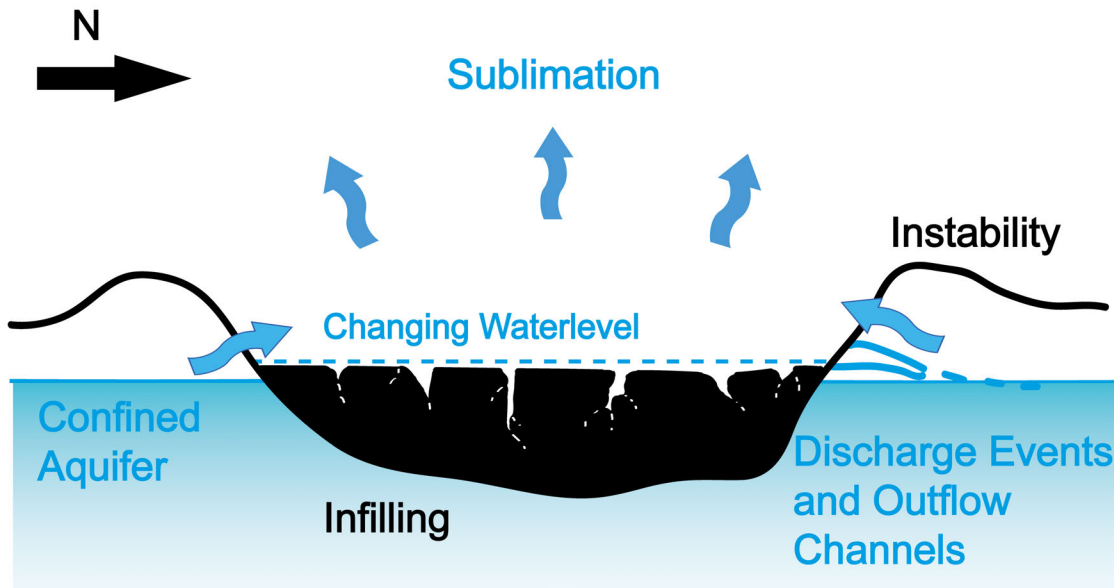


Figure 4.3.: Model of groundwater migration. A confined aquifer and flowing water in the subsurface lead to seepage and piping in the crater filling. Fractures are developed and widened with time. The fluvial activity is not only responsible for weathering and erosion but for the fracturing itself [Sato et al., 2010].

scale polygons on Mars. A saturated sediment layer must be deposited on top of a permafrost layer. The sediment layer begins heating up from the upper surface through solar radiation. Due to the density difference between the warm surface water (277K) and the cold subsurface water (273K), the surface water sinks and Rayleigh convection initiates [Wenrich and Christensen, 1993]. Density-driven convection can only initiate with a stable temperature difference. Numerous convection cells are formed by this process, with the size of the cells determining the size of polygons (Fig. 4.4). Additionally, buried topography has an influence on the size of the polygons [Cooke et al., 2011]. Large scale polygons have been observed in the Martian lowlands that have an average size of 5 km [Cooke et al., 2011, Gasselt, 2007, Hiesinger and Head, 2000, Lane and Christensen, 2000]. A convecting layer between 1,100 and 1,500 m in thickness is necessary to form 5 km polygons on Mars [Lane and Christensen, 2000]. These large scale polygons can be formed near the equator up to  $\pm 40^\circ$  latitude [Luchitta, 1983]. Impact craters can serve as natural sinks and consequently, water concentration points. Therefore, the Rayleigh convection model is reasonable inside craters refilled by ice-rich or water-rich materials. These craters are most likely present in the lowest elevation areas in the Martian lowlands [Hiesinger and Head, 2000, Lane and Christensen, 2000], because of the enrichment of water in the subsurface. Once fractures have been developed, erosional processes, most likely involving wind or water, will enlarge them. However, for this model the fractures would be distributed regularly within the entire crater, assuming a homogeneous crater infilling.

#### 4.3.5. Deep-Water Fault Systems

Deep-water fault systems are another type of near-surface tensile stress. Large scale polygons can be developed in deep-water (Fig. 4.5). On Earth, polygon systems occur in fine grained sediments, within a water depth  $>500$  m and at shallow burial depths [Cartwright et al., 2003]. These show similarities to Martian systems and

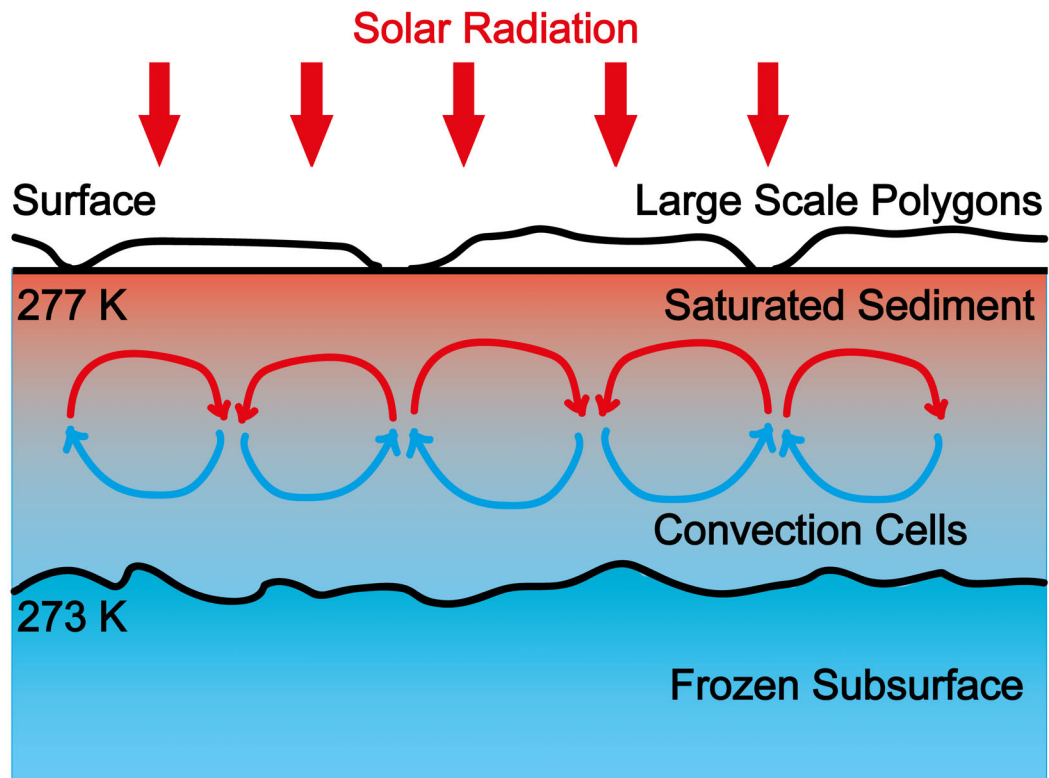


Figure 4.4.: Model of density-driven convection cells. This model has been used to explain large scale polygons on the Martian surface [Wenrich and Christensen, 1993].

might provide another possible formation mechanism for polygon systems on Mars. An average polygon thickness of 500 m and a size up to 3 km can be reached on Earth [Moscardelli et al., 2012]. Based on the geomorphologic similarities between large-scale polygons on Earth and on Mars, the model of polygons developing in deep-water (>500 m) in the Martian lowlands was suggested by Moscardelli et al. [2012]. For this type of fracturing, a crater needs to be filled with at least 500 m of water.

#### 4.3.6. Tectonics

Several tectonic fractures are located close to the dichotomy boundary of Mars. These features are often parallel to the boundary itself [Smrekar et al., 2004]. Fractures are visible in the craters and in the surrounding area (Fig. 4.6). Crater floors are areas of weakness, so fracturing due to tectonics will preferentially occur there [Melosh, 1989]. The large scale of the fractures is easily explained by tectonics. In the case of an ice-rich subsurface, outflows form by tectonic pressurization. Fault movement puts the subsurface drainage under pressure and therefore, leads to outflow events [Hanna and Phillips, 2006].

### 4.4. Importance of FFCs

The understanding of surface processes in the Martian history is limited. Impact cratering is a process which can be found on every planetary body in our solar system and therefore, is of high importance for the understanding of surface processes.



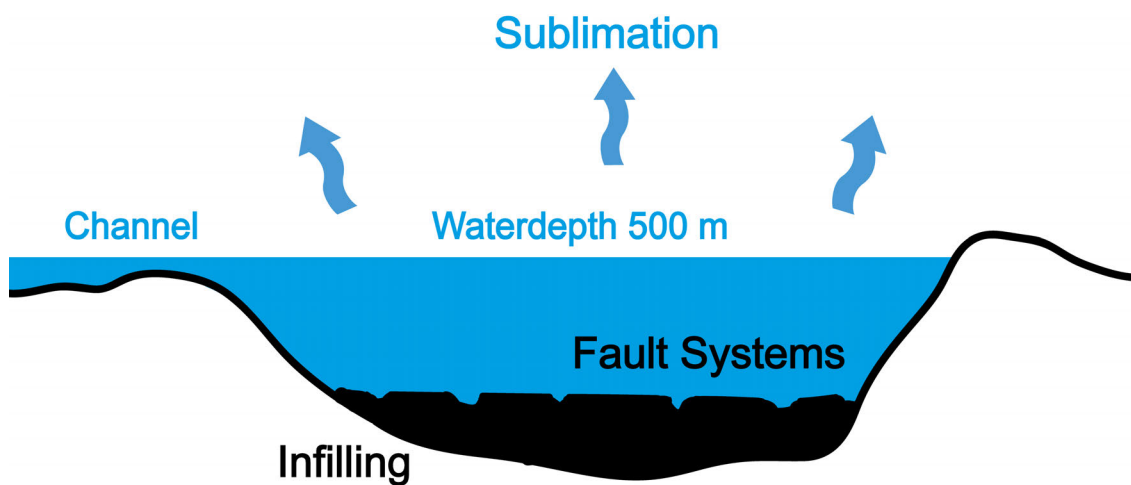


Figure 4.5.: Model of deep-water fault systems. This model is used to explain large scale polygons in the Martian lowlands with a minimum water depth of 500 m [Moscardelli et al., 2012].

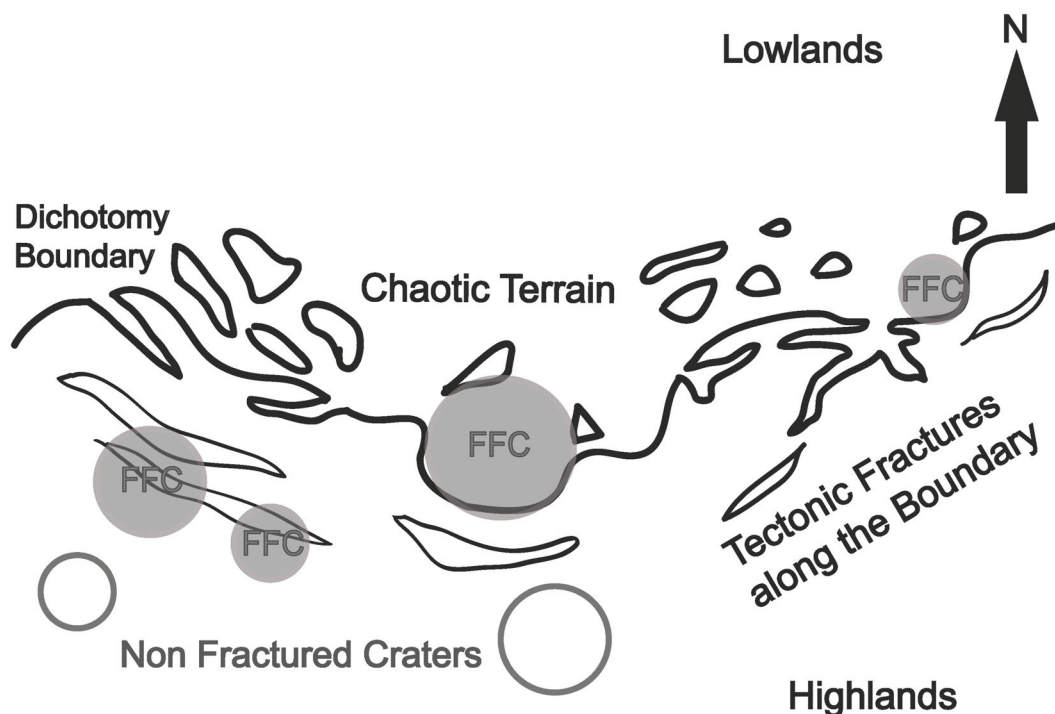


Figure 4.6.: The model for the origin of FFCs due to large scale tectonic systems. Graben systems dissect impact craters and trigger further fracturing within the craters.

The research about FFCs will help to gain a better understanding of the spatial distribution of craters on Mars and the involved processes in FFC formation and evolution. Finding these craters on Mars and identifying different formation processes will improve our knowledge of geologic processes within Martian history. Since water might be involved in the origin of particular FFCs on Mars, these craters could also be important as potentially habitable sites correlated with volcanic, fluvial, and hydrothermal activity. Impact craters are considered to be essential for the development of life on planetary bodies [Lammer et al., 2009, McKay and Marinova, 2001]. On Mars, impact craters can operate as closed environments in the form of paleolakes, which would build habitable zones and likely support the development of life.

# Part II.

## Methods



## 5. Manual Crater Analysis

I analyzed two distinct FFCs and used them as a case study [Bamberg et al., 2014]. They are located in different environments on Mars, resulting in different surface features on the interior and exterior of each crater. Features were analyzed and interpreted to describe the geologic setting and the crater morphology. From these, a geologic map and geologic profile were developed for each crater. Measurements, calculations, and crater counting also provide further information on the stratigraphy and ages for surface units.

### 5.1. Data and Software used for Crater Analysis

Data from the Mars Express (MEX) High Resolution Stereo Camera (HRSC), the Mars Reconnaissance Orbiter (MRO) Context Camera (CTX), the Mars Odyssey (MO) Thermal Emission Imaging System (THEMIS), and the Mars Global Surveyor (MGS) Mars Orbiter Laser Altimeter (MOLA) were used.

The HRSC camera has a resolution of 12.5 m/pix for Nadir observations, 75 m/pix lateral and 11 m/pix vertical for digital elevation models [Gwinner et al., 2010, Jaumann et al., 2007, Neukum and Jaumann, 2004, Scholten et al., 2005]. Digital Terrain Models (DTMs) and Nadir images are used to analyze the surface morphologies of both craters. These data are also used to generate geologic cross sections, as well as slope maps of both craters. CTX images, with a resolution of 6 m/pix [Malin et al., 2007], are available within the investigation area. Nighttime images from THEMIS with a resolution of 100 m/pix are used to analyze the thermal infrared brightness of surface materials [Christensen et al., 2004].

The geoinformation system ArcGIS 10.0 from ESRI is used for geologic mapping. The geoscientific analysis includes slope, elevation, object size, crater diameter, and crater depth measurements, as well as interpretation of lengths and orientation of linear features. Based on these data, topographic cross-sections of the craters are developed [Bamberg et al., 2014] and provide important stratigraphic information. Rose diagrams using the Generic Mapping Tool, psrose [Wessel and Smith, 2013] were produced, for further analysis of linear features. The orientation patterns of those features are indicators for specific geologic processes (e.g. tectonics). Detailed observations are needed to analyze the processes involved in their formation and to classify the craters according to their origins. To identify the age of different surface units crater size frequency distribution (CSFD) measurements are performed [Hartmann et al., 1981, Hartmann and Neukum, 2001, Ivanov, 2001, Neukum, 1983, Neukum and Ivanov, 1994]. In this work the CraterTools software extending ArcGIS for counting and measuring craters [Kneissl et al., 2011], and Craterstats2 for analyzing the CSFD data are used [Michael and Neukum, 2010].

To constrain the formation periods of the fracture networks buffered crater counts (BCC) using a method similar to that described in Fassett and Head [2008] were conducted. The formation time of the fractures is dated by considering craters that formed in the vicinity, superposing the fracture wall either directly or with their ejecta. This is necessary because the surface area of the fracture floors is

small, and they are likely to have been resurfaced by mass wasting from the fracture escarpments. The effective counting area is increased by a buffer zone that represents the area where impacts superpose fractures. The width of the buffer zone depends on the size of the crater and the expected extent of that crater's continuous ejecta deposit. The extent of the ejecta is estimated as a multiple of the crater radius, based on the local observations [Kneissl and Michael, 2013].

## 5.2. Observations of Crater A

### 5.2.1. Geologic Setting and Crater Morphology

The first investigation area is located north of Syrtis Major and in the eastern part of Arabia Terra. The area ranges from 25° to 39°N and from 54.5° to 76°E. This area is of major interest because there are several FFCs in the region. Also, CTX and HRSC have complete spatial coverage of these craters and provide a solid database for geoscientific analysis. The region reveals various types of surface features including: layered materials [Malin and Edgett, 2000], fluvial channels [Sharp and Malin, 1975], relief inversion [Fassett and Head, 2007], mesas [Carr, 2006], linear features, avalanches [Carr, 2006], floor fracturing, fretted terrain [McGill, 2002, Sharp and Malin, 1975, Sharp, 1973], mass wasting landforms, and patterned ground [Carr, 2006]. In Arabia Terra linear escarpments parallel to the dichotomy boundary indicate fault scarps [Carr, 2006]. These features suggest that glacial, tectonic, aeolian, fluvial, and hydrothermal processes played a role in modifying the landscape [Andrews-Hanna et al., 2010, Dohm et al., 2007, Edgett and Malin, 2002, Fairén et al., 2003, Greeley and Guest, 1987, McGill, 2002, Morgenstern et al., 2007, Tanaka, 1986]. The terrain is characterized by a layered mantling unit and inverted relief. Etched terrain pervades the area. The mantling unit was deposited in the late Noachian or early Hesperian [Fassett and Head, 2007] and likely consists of volcanic ash, originating from Syrtis Major in the south. Weathering and removing of the mantling unit occurred at the Noachian-Hesperian boundary [Fassett and Head, 2007]. The Arabia Terra region is a distinct center of tectonic activity [Anderson et al., 2008], has a high crater density consisting mostly of Noachian materials [Barlow, 1988, Greeley and Guest, 1987, Tanaka, 1986], and has the greatest extent of well-developed fretted terrain on Mars [Carr, 2006, Scott et al., 1995, Sharp, 1973]. Furthermore, large outflow channels [Scott et al., 1995] and high concentrations of multiple layer ejecta and central pit impact craters are present. These are indicative of large quantities of volatile rich material [Barlow and Perez, 2003]. Thus, water likely played an important role in the formation and evolution of the surface in Arabia Terra [Dohm et al., 2007, Rodriguez et al., 2005].

The first crater I analyzed (Crater A) is located west of the Nili Fossae region near the dichotomy boundary (29.3°N, 70.4°E) (Fig. 5.1). The impact occurred in highly eroded Noachian- Hesperian basement rock and has a diameter of 90 km. The crater floor is highly dissected and split up into several knobs, ranging in size from a few meters to 10s of kilometers. The mean size of these knobs is ( $w_K$ ) is 1320 m (Fig. 5.2 A,B and 5.3). They appear to be distributed randomly inside the crater.

The knobs in the eastern part of the crater are, on average, 400 m higher than the knobs in the west. The surface of the western knobs is highly eroded, visible in the inverted terrain (Fig. 5.2 B ). Terrain inversion was also identified on the basement material and on the knobs. This process can occur when former depressions are filled

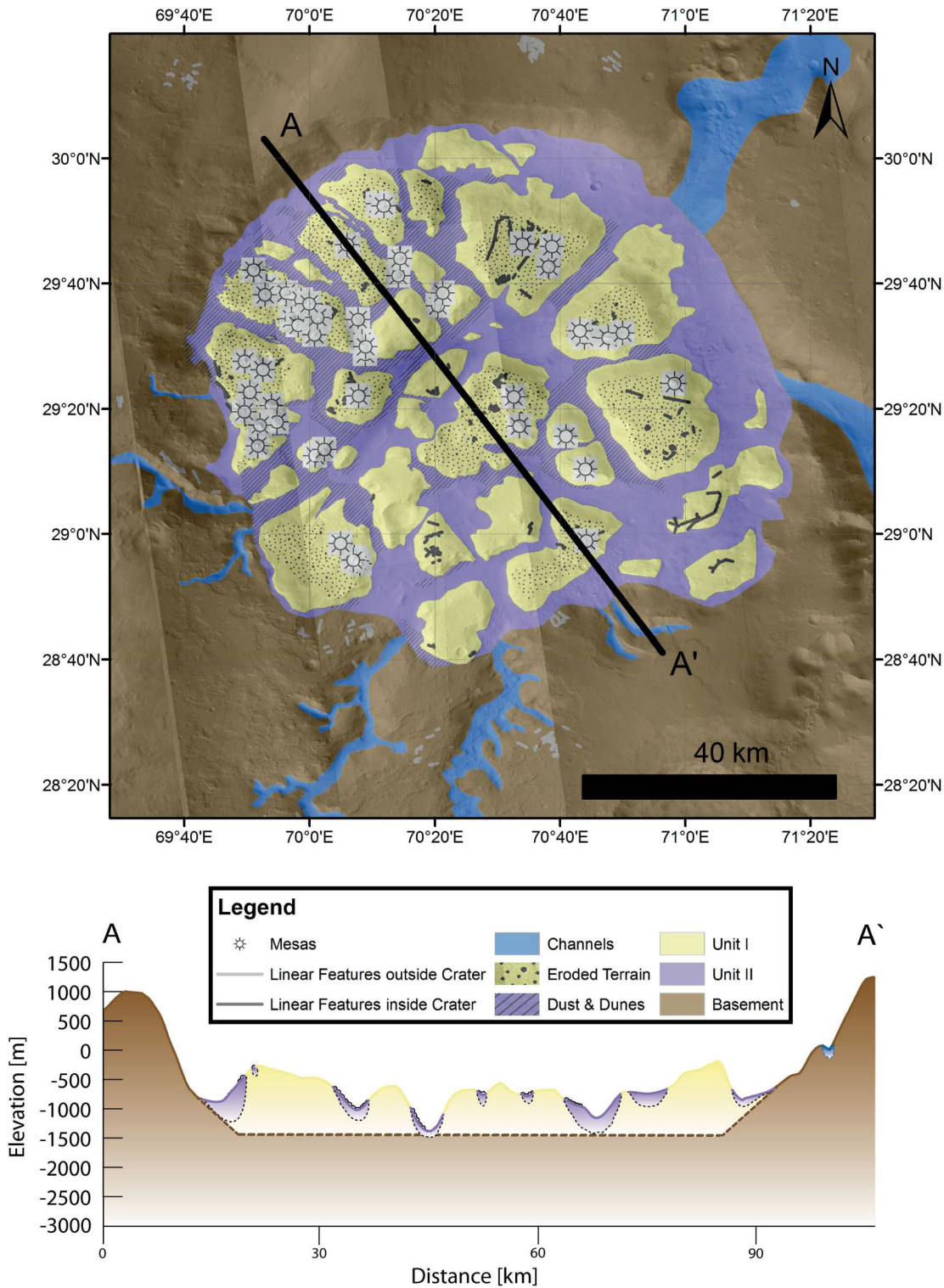
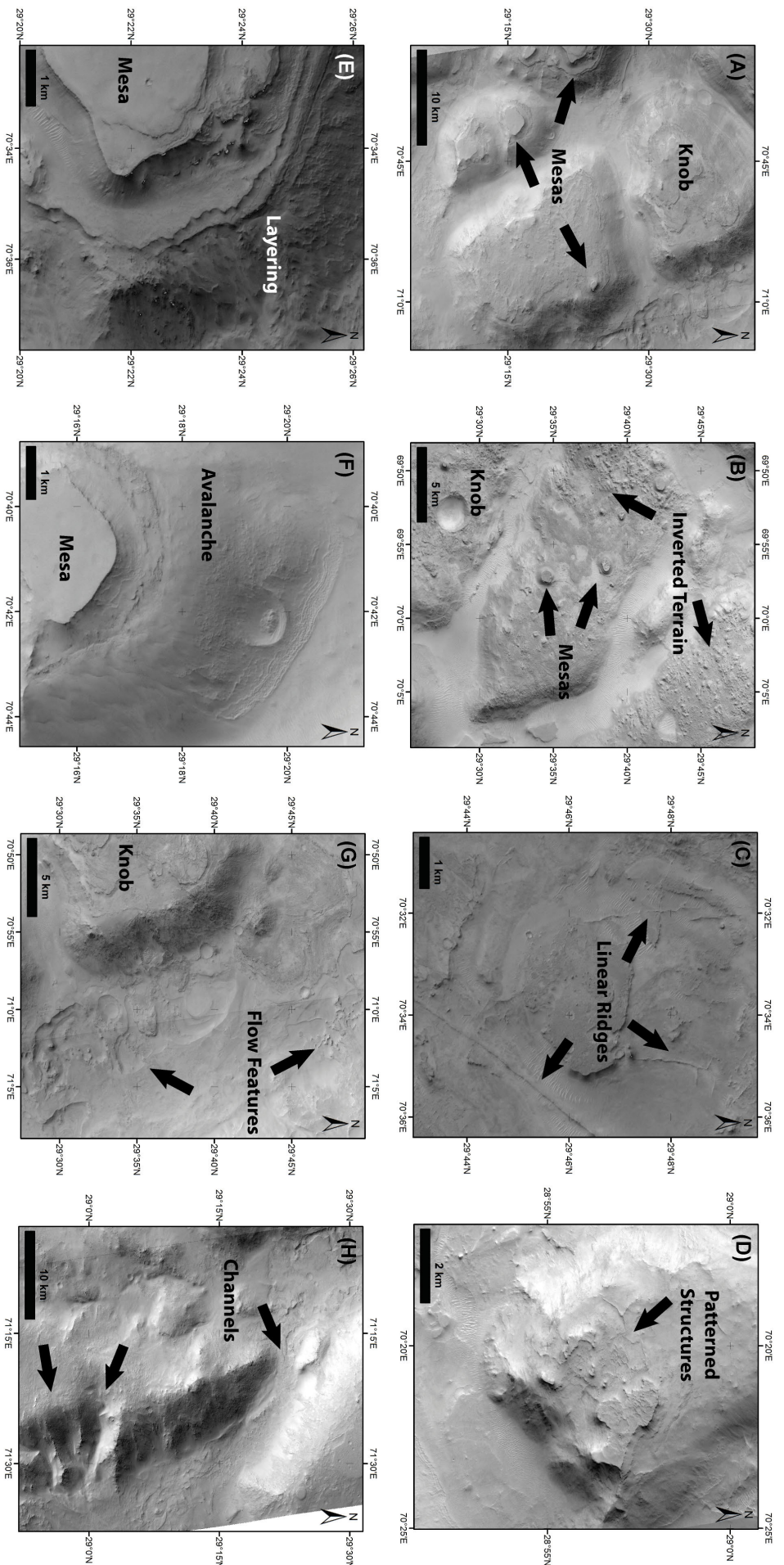


Figure 5.1.: Geologic map and cross-section AA' of Crater A. CTX data are used for the mapping. The elevation profile is obtained from HRSC DTMs.



*Figure 5.2.: Set of CTX images of the interior of Crater A. (A) Knobs in the eastern part of the crater with a size >10 km are separated by fractures. On top of the knobs mesas are observed. They are layered and have a smooth, flat, dust-covered, surface. (B) Large knobs and small mesas located in the western part of the crater. The surfaces of the knobs are inverted and highly eroded. (C) Linear ridges up to several kilometers long are observed on the knobs. (D) Some of the linear ridges form patterned and polygonal structures. They appear solely on the knobs. (E) Horizontal layering and terraces are observed on some knobs and mesas. (F) The northern flanks of the knobs and mesas are often covered by avalanches. (G) The second crater infilling is characterized by flow features and suggests fluvial activity within the crater. (H) Channels are carved into the crater rim and could have provided inflow and outflow of water to and from the crater.*



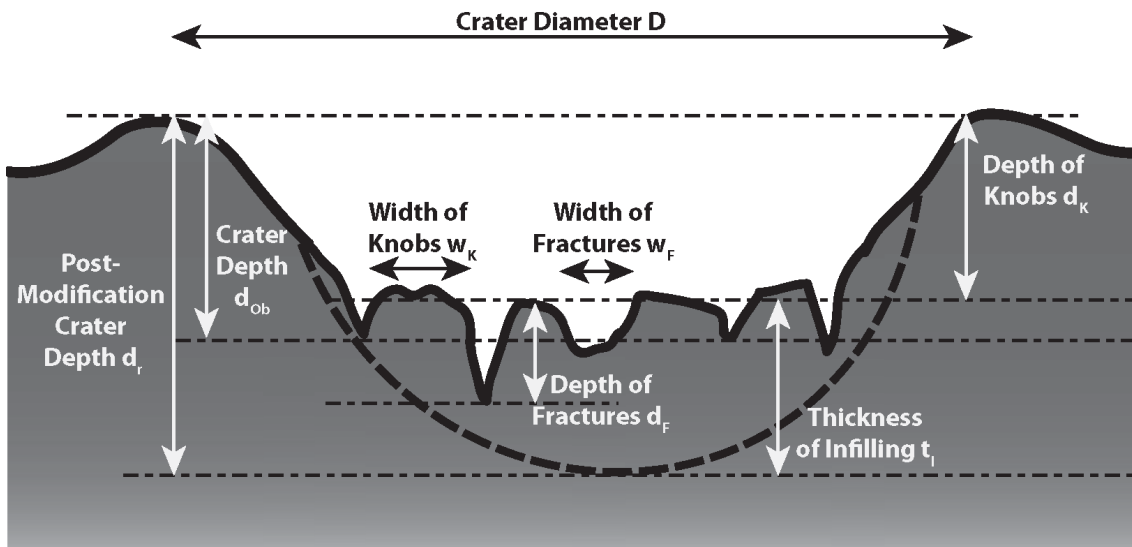


Figure 5.3.: Sketch of an example FFC and the observed and calculated crater morphology. The white arrows show depth measurements, the black arrows display widths and size measurements. The properties (Depth of Knobs, Crater Diameter, Thickness of Infilling, etc.) indicate important characteristics of FFCs. The craters can be compared based on the measured and calculated values.

by material that is more resistant to weathering than the surroundings. Possible infilling processes are fluid mixing during groundwater flow, hydrothermal activity, evaporation and sublimation of surface water [Pain et al., 2007]. In Arabia Terra the overlying mantling unit must have been more resistant than the surrounding units or protected by other materials, leading to the terrain inversion. The most reasonable mechanism for creating large areas of inverted terrain is aeolian weathering [Fassett and Head, 2007]. Terrain inversion in Arabia Terra could also have been formed by sublimation of ice particles in the subsurface, conductive volume loss, and collapse of material as proposed by Fassett and Head [2007]. The knobs evolved from layered materials and terraces, suggesting sedimentation and deposition of material.

47 mesas are observed on the knobs in the crater (Fig. 5.1). They represent the topmost layer of the knobs and, therefore, the maximal infilling height of the crater (Fig. 5.2 B,E,F).

The topographic cross-section of Crater A extends from NE to SW through the crater. The geologic map and cross-section of Crater A suggest a high level of erosion (Fig. 5.1).

In the eroded regions on the knobs, patterned and linear ridges are observed (Fig. 5.2 C,D). The orientations of small-scale linear features on the knobs and in the Noachian basement material are presented in a rose diagram (Fig. 5.4 A). The linear features in the crater are widespread and do not show a preferred orientation trend. The rose diagrams for single knobs do not show any preferred orientations either. These features are only observed within inverted terrain, therefore, it is likely that linear ridges are inverted as well. Some ridges form patterned structures. The ridges are very thin, so their heights are not measurable within the available DTM resolution. 477 ridges inside the crater were counted. The mean length is approximately 420 m (min = 47 m and max = 7,347 m). The rose diagrams indicate that linear features outside the crater have orientation trends toward the northwest and southeast, following the tectonic structures and orientations of the fretted terrain

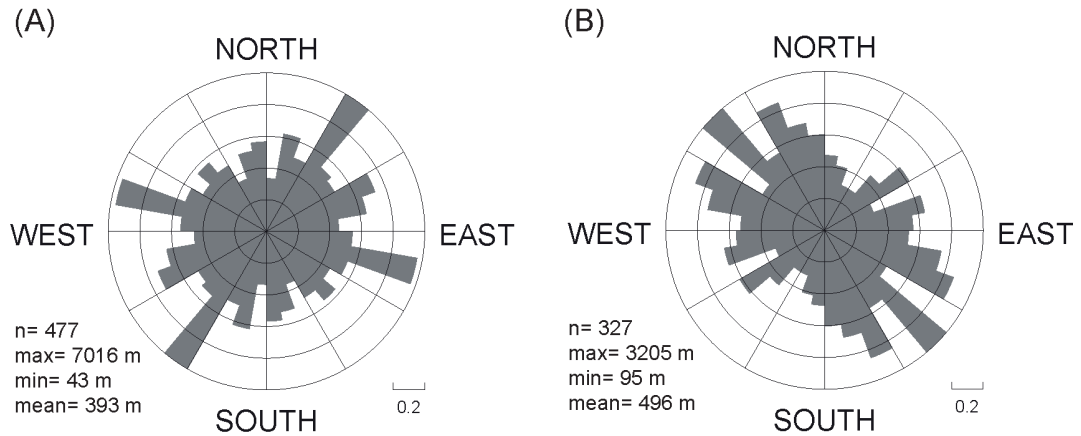


Figure 5.4.: Fault orientations within Crater A (A) and outside Crater A (B). Directions are measured in a local conformal map projection using the start and end point of each fault. Results are weighted linearly by the lengths of the faults.

close to the dichotomy boundary (Fig. 5.4 B).

The material separating the knobs is characterized by flow features and has a very smooth surface, indicating modification by fluvial processes (Fig. 5.2 G). Widening of the fractures could have also occurred by fluvial activity. Supporting this observation, channels lead into the crater in the southwest and run through the crater, connecting it to the lowlands in the northeast (Fig. 5.2 H). The knobs are further defined by the presence of layering. Terraces at different elevations within the crater are also present. These could form in several ways. The withdrawal of magma was suggested as a possible origin for terraces [Leverington and Maxwell, 2004]. The terraces may be remnants of a former level floor that almost eroded away as a result of a lowering of outflow channels. Concentric rings surrounding the knobs may also indicate successive shorelines or stages of removal of crater fill [Carr, 2006]. The knobs are not tilted, as shown in the geologic mapping (Fig. 5.1). The layering appears to be horizontal (Fig. 5.2 E). Several avalanches are located on the northern flanks of the knobs. These are likely due to steep slopes as well as the composition of the flanks and the material (Fig. 5.2 F). The avalanches flow between the knobs and partially infill the fractures. These large scale fractures have an average width ( $w_F$ ) of 4000 m and an average depth ( $d_F$ ) of 322 m. The main fracture is the deepest and extends from the channels in the southwest toward the northeastern channel (Fig. 5.5).

Dunes and dust cover about 15 % of the floor in the northwestern portion of the crater as well as within the fractures.

### 5.2.2. Measurements

The post-modification crater depth can be estimated for craters with a diameter ranging from 7 to 100 km by using the equation:

$$d_r = 0.357 \cdot D^{0.52} \quad (5.1)$$

where  $d_r$  is the crater depth from the rim crest and  $D$  is the rim crest diameter, both measured in kilometers [Tornabene et al., 2013]. The knob depth ( $d_K$ ) is the

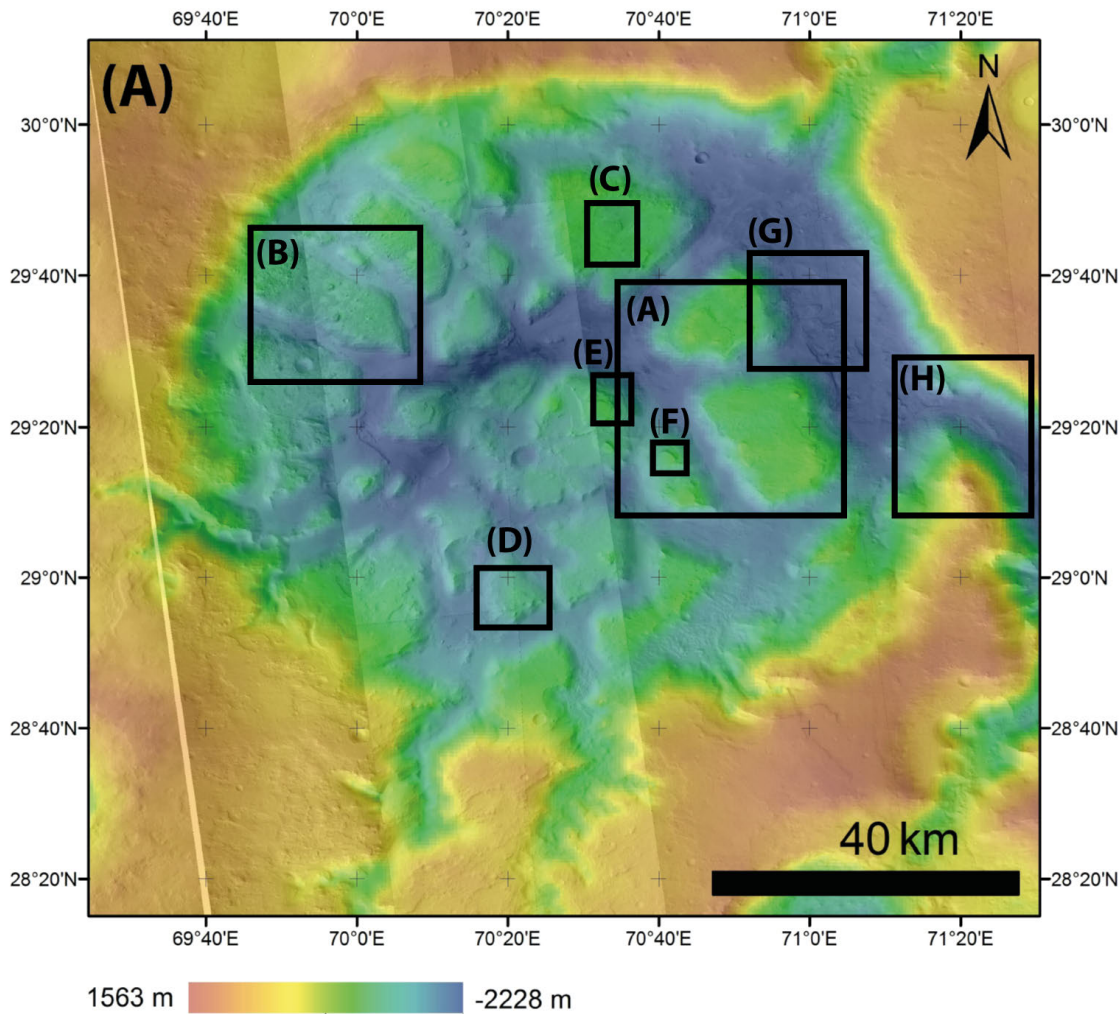


Figure 5.5.: HRSC DTM superposed by a mosaic of HRSC images with a 75 m/pixel lateral and 10 m/pixel vertical resolution of Crater A. Boxes show location of detailed view at Fig. 5.2.

height difference between the crater rim and the average knob elevation (obtained from DTM elevations). The fracture depth ( $d_F$ ) is the difference between the average knob depth and the average measured incision depth of the fractures. The observed crater depth ( $d_{Ob}$ ) is the average of the knob depth ( $d_K$ ) and the fracture depth ( $d_F$ ). To calculate the thickness of the infilling ( $t_I$ ) the post-modification crater depth is subtracted by the knob depth ( $d_K$ ):

$$t_I = d_r - d_K \quad (5.2)$$

$t_I$  represents the highest amount of infilling. The calculated and observed crater features are presented in Tab. 5.1 and Fig. 5.3.

### 5.2.3. Crater Size Frequency Distribution

I counted craters to determine the chronology of geologic events in the Arabia Terra region. Unfortunately, this area is highly eroded due to fluvial, glacial, and aeolian processes. Highly sloped regions were excluded from the crater counting.

Feature	Type	Crater A
Crater diameter $D$	O	90 km
Post-modification crater depth $d_r$	C	3,706 m
Crater depth $d_{Ob}$	O	726 m
Depth of knobs $d_K$	O	645 m
Depth of fractures $d_F$	O	322 m
Thickness of infilling $t_I$	C	2,980 m
Central peak height $h_{cp}$	C	-

Table 5.1.: Overview of important depth values of Crater A. The types are divided into Observation (O) and Calculation (C).

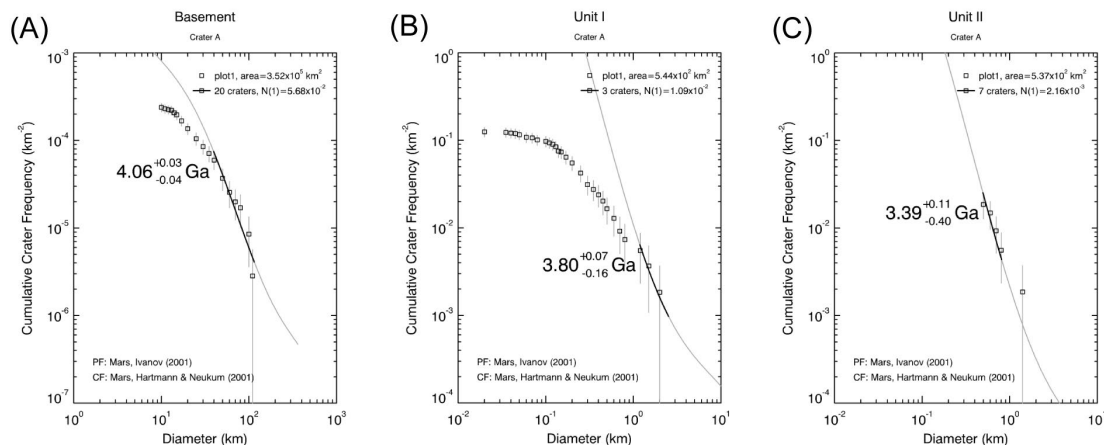


Figure 5.6.: I used Craterstats2 to analyze the crater counts. (A)-(C) show ages for surface units located inside Crater A.

The basement terrain of Crater A was dated to 4.06 Ga and is of Noachian age (Fig. 5.6 A), which matches the ages obtained by Fassett and Head [2007].

The crater counting for the knob unit shows a gentle slope, revealing a high degree of weathering and erosion (Fig. 5.6 B). Inverted and fretted terrain influence the crater counting, since these types of terrain typically remove small impact craters when forming. All knobs comprise the counting area and were dated to 3.80 Ga.

Obtaining an age for the floor of the fractures is difficult due to small channels, steep slopes, flow features, and dune and dust deposits. Small impact craters ( $d < 400$  m) are modified or covered. However, based on 7 craters, a crater floor age of 3.39 Ga was determined (Fig. 5.6 C).

BCC for the fractures of crater A was not feasible, due to the high level of erosion of impact craters on the knobs.

## 5.3. Observation of Crater Lipany

### 5.3.1. Geologic Setting and Crater Morphology

FFCs also occur in areas where indicators for fluvial activity are absent. The second crater I analyzed is Crater Lipany. It is 47 km in diameter and located south of Syrtis Major ( $-0.2^\circ\text{N}$ ,  $79.7^\circ\text{E}$ ) (Fig. 5.7). Syrtis Major was volcanically active during all

periods of the Martian history, as shown by surface ages obtained from CSFD measurements [Jodlowski et al., 2012]. The impact that created Crater Lipany occurred in Noachian-Hesperian basement rocks [Jaumann et al., 2010]. Volcanic plains, originating from the volcanic region, are found at the western and southern flanks of the crater (Fig. 5.8 A). Thermal infrared (6.78 - 14.9  $\mu\text{m}$ ) nighttime observations (acquired from THEMIS) (Fig. 5.8 A) indicate that these plains, along with other lava sheets outside the crater, have thermal brightness values that are similar to the crater infilling [Jaumann et al., 2010]. The ejecta blanket is still visible along the northwestern rim of the crater. This suggests that Crater Lipany has lower weathering rates, or is younger in age, than Crater A.

The Crater is filled with materials that make up two distinct surface units. The first unit exhibits knobs with sharp escarpments that are separated by a radial fracturing system around the central peak (Fig. 5.8 B). Steep slopes lead to mass wasting and downslope movement, which infilled the fractures. Additionally, dust and dunes are located along the fractures and cover  $\sim 14\%$  of the total crater floor (Fig. 5.8 C). Nevertheless, depressions are visible along the fracturing system (Fig. 5.8 D). The second unit is highly structured by secondary impact craters in the form of crater chains and fields (Fig. 5.8 E). It infills the crater and borders the knobs (Fig. 5.8 F). This unit has the same infrared radiances and surface structure as the volcanic plains surrounding the crater (Fig. 5.8 A).

The size of the knobs varies from tens of meters to few kilometers, with a mean size of 620 m. They are separated from each other by a mean distance of 1,230 m. Individual knobs resemble “puzzle pieces” that, when fit together, build up one continuous surface unit. This suggests that the surface unit was connected before fracturing began. The elevation of knobs inside the crater differs, maximally, by 500 m (Fig. 5.9 and 5.7). The knobs are displaced upward near the central peak of the crater where the infilling increases in elevation. This also occurs near the crater rim, suggesting processes occurred in the subsurface after deposition of material (Fig. 5.9 and 5.7). Wrinkle ridges are present in the volcanic units outside and inside the crater. These developed by the cooling and contraction of material. The difference in size of the surface features between Crater A and Crater Lipany is likely due to the smaller diameter of Crater Lipany as well as the, presumably, lower degree of weathering and/or younger age of Crater Lipany. As a result, fractures are neither widened nor rounded by fluvial processes in this crater (Fig. 5.7).

### 5.3.2. Measurements

Crater depth and infilling are shown in Tab. 5.2 and Fig. 5.3.

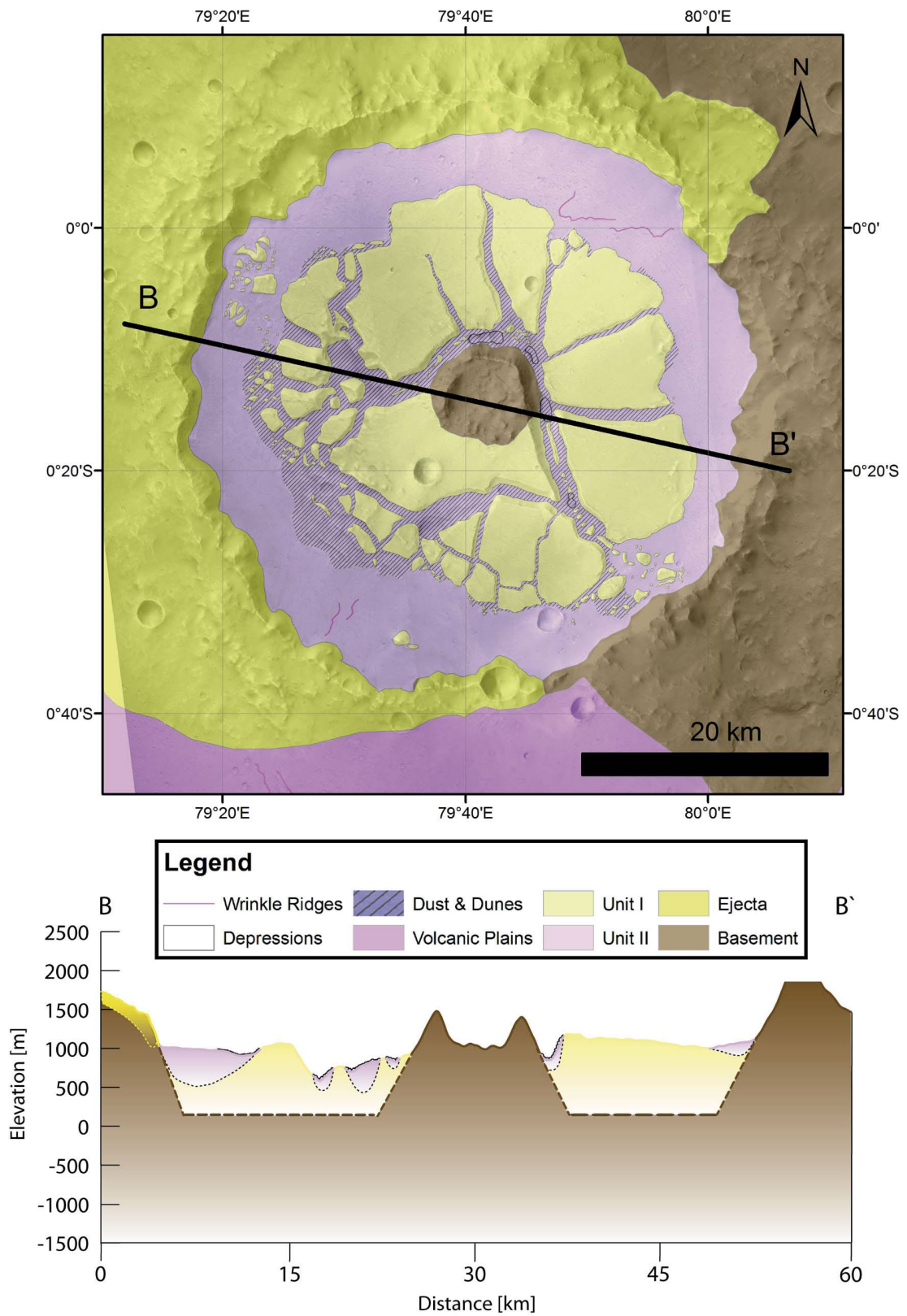
Remnants of the central peak are visible in the center of the crater. The maximum central peak height after formation is calculated by the equation of Garvin et al. [2003]:

$$h_{cp} = 0.04 \cdot D^{0.51} \quad (5.3)$$

A peak height of 0.285 km is calculated for Crater Lipany. The observed mean height is 0.395 km and therefore, about 1.3 times higher than expected.

### 5.3.3. Crater Size Frequency Distribution

Relative ages of the different surface units can be obtained by using the principles of superposition. However, crater counting was conducted to obtain more precise



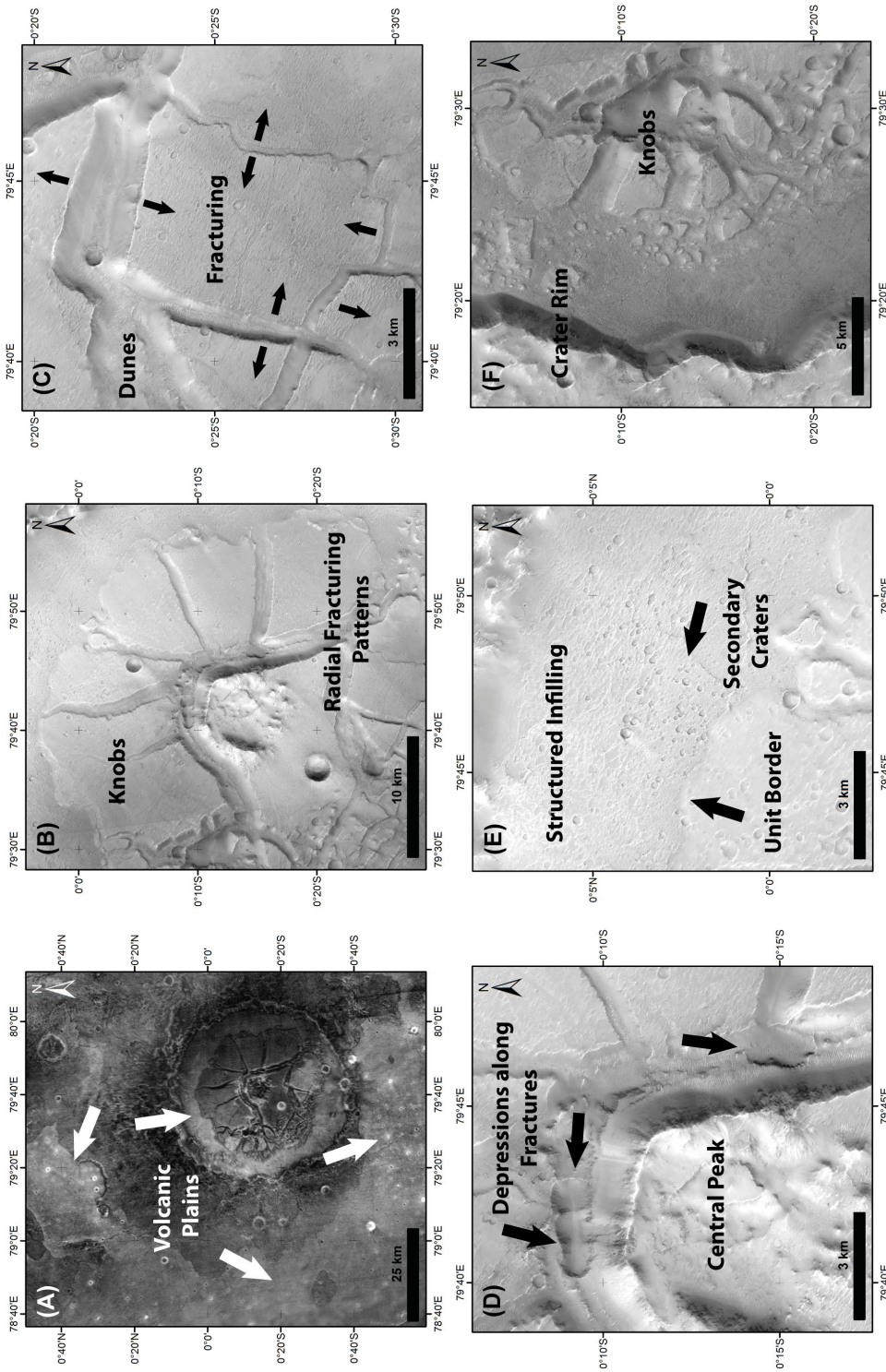


Figure 5.8.: Set of THEMIS nighttime images and CTX images of the interior of Crater Lipany. (A) Several volcanic plains are observed in the THEMIS images. The infrared radiance inside the crater and outside the crater are the same. The lava flows originate from Syrtis Major in the north. (B) Several knobs, separated by a radial fracturing system, are distributed around the central peak. (C) The knobs are separated from each other by fractures of different sizes. Regardless of fracture size, knobs still fit together like “puzzle pieces”. (D) Depressions are observed within the main and largest fractures surrounding the central peak depression. (E) The infilling is highly structured, secondary craters are visible. The border between the different units is easily distinguishable. (F) Well preserved crater rim, fractures, and knobs. Small knobs are randomly distributed in the second crater infilling.

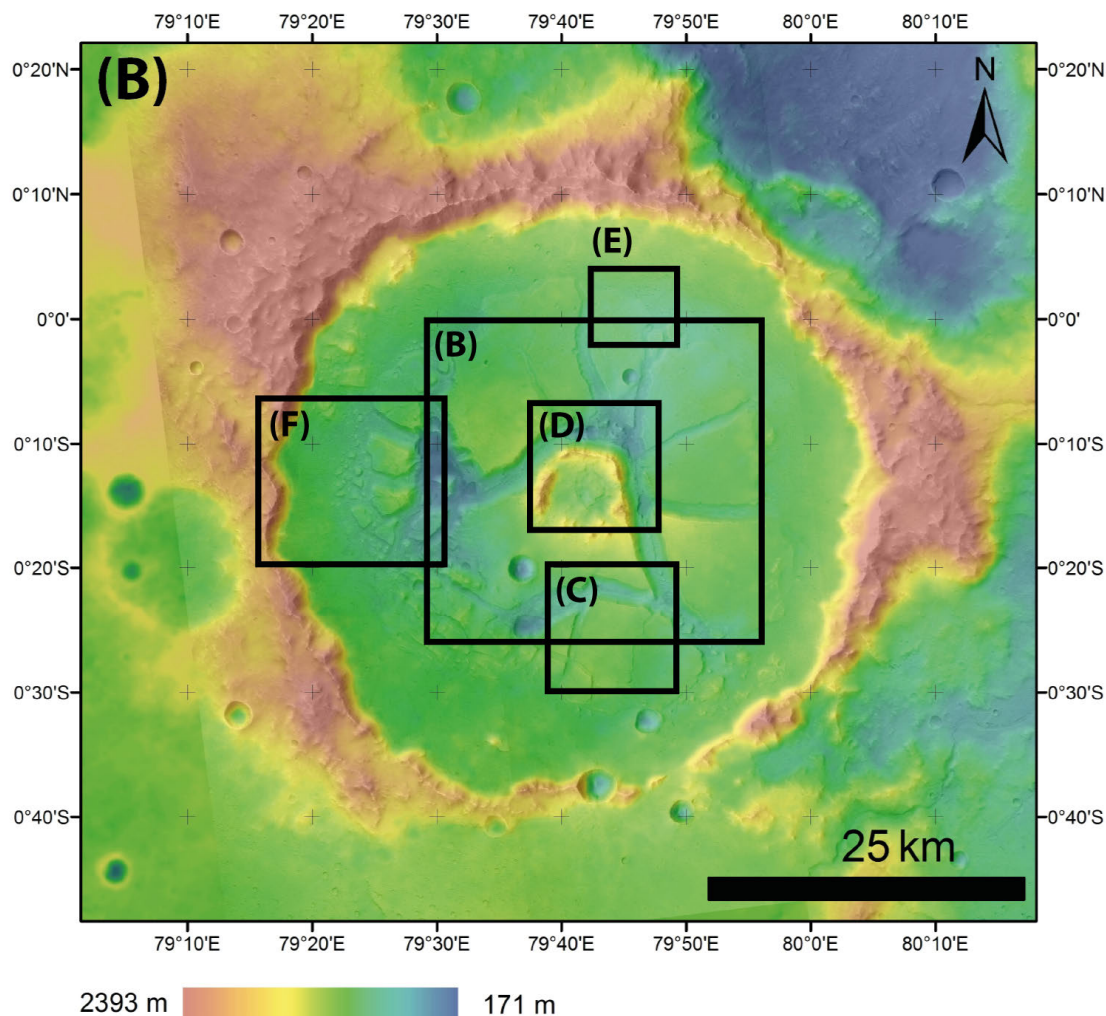


Figure 5.9.: HRSC DTM superposed by a mosaic of HRSC images with a 75 m/pixel lateral and 10 m/pixel vertical resolution of Crater Lipany. Boxes show location of detailed view at Fig. 5.8.

and comparable results of the surface age.

Ejecta of the impact were deposited at the northwestern edge of the crater. Crater counting indicates an age of 3.85 Ga for the ejecta and therefore, for the impact event itself (Fig. 5.10 A).

Six of the knobs represent the counting area for the age determination of the knob unit. Secondary crater fields were excluded from the crater counting (Fig. 5.8 E). The surface unit appears to have karst-like structures, complicating the identification of impact craters. Crater counting yields ages between 2.42 Ga and 3.95 Ga. The black isochron (Fig. 5.10 B) is adapted to the three largest craters in the counting area and indicates the same age as the ejecta. A significant number of craters follow the red isochron (Fig. 5.10 B), yielding a younger emplacement age; resurfacing processes may be responsible for this difference. Large craters are the most important for the determination of the time of formation [Hartmann and Neukum, 2001] and are used for the age calculation of the knob unit.

A second type of infilling was deposited close to the crater walls and borders the knob unit. The unit appears to be highly resurfaced by depressions (Fig. 5.8 E).



Feature	Type	Crater Lipany
Crater diameter $D$	O	47 km
Post-modification crater depth $d_r$	C	2,643 m
Crater depth $d_{Ob}$	O	669 m
Depth of knobs $d_K$	O	664 m
Depth of fractures $d_F$	O	10 m
Thickness of infilling $t_I$	C	1,970 m
Central peak height $h_{cp}$	C	285 m

Table 5.2.: Overview of important depth values of Crater Lipany. The types are divided into Observation (O) and Calculation (C).

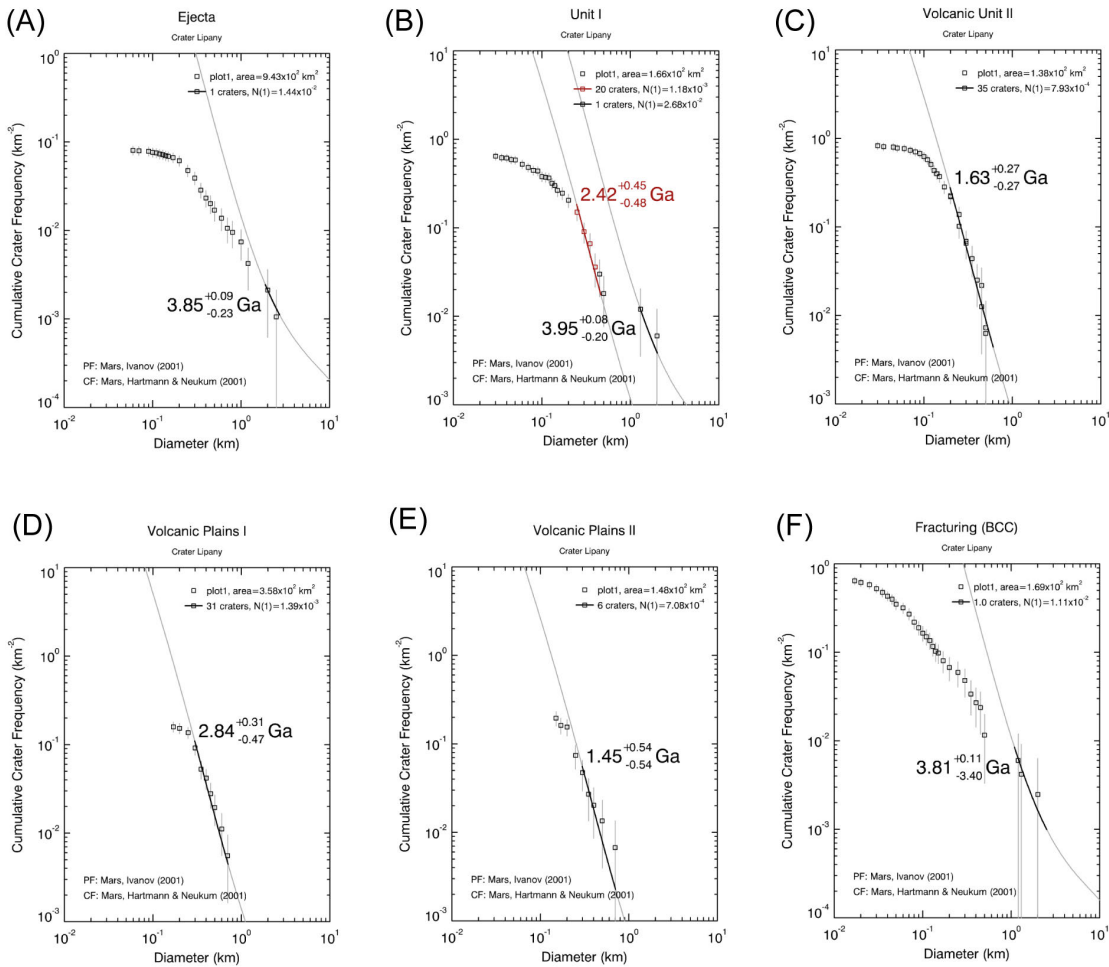


Figure 5.10.: I used Craterstats2 to analyze the crater counts. (A)-(E) show ages for units inside and outside of Crater Lipany. (F) shows the resulting CSFD for the buffered crater counting of Crater Lipany. The ejecta blanket was assumed to extend up to a distance of one crater diameter radially from the crater rim, leading to a buffer size of 1.5 crater diameter around the linear features.

Distinguishing between pits, pseudo craters, and impact craters is difficult, so those areas are avoided for crater counting (Fig. 5.10 C). The countable craters indicate a surface age of 1.63 Ga.

The age of the exterior lava unit on the south side the crater was determined to be 2.84 Ga (Fig. 5.10 D). Another lava unit in the west appears to be younger, yielding ages of up to 1.45 Ga (Fig. 5.10 E). The measured unit ages are consistent within the error bars with the constraints of Jaumann et al. [2010].

To obtain an age for the fracturing itself, BCC was used (Fig. 5.10 F). The larger craters ( $d > 1$  km) indicate an age of 3.81 Ga.

## 6. Databases

The crater analysis (Chapter 5) provided information about important surface features to aid in determining the origin of the 433 FFCs found on Mars. The features are divided into interior and exterior surface features. These surface features must be analyzed for each FFC and the information needs to be stored within a database, which can be used for further analysis.

### 6.1. Parameters for the Database

The origin of FFCs is analyzed according to observed surface features (e.g. Bamberg et al. [2014]). These features provide key parameters for the interpretation of processes involved in formation and modification. The interior analysis focuses exclusively on the crater interior without spatial context. For a more complete analysis, surface features outside the crater were taken into account, as they provide insights about the spatial context.

#### 6.1.1. Interior Surface Features

The following surface features inside the craters were analyzed in the database (Tab. 6.1).

##### Central Peak

The central peak is a mountain or set of mountains in the center of the impact. It is usually the highest point of the crater floor, while still being lower than the rim crest [Melosh, 1989].

##### Depression

Depressions along the fracturing system are developed due to subsurface voids and collapse of overlaying material. They can represent volcanic pits, lava tubes, or sinkholes [Murawski and Meyer, 2004].

##### FFC

FFCs are characterized by the distinct appearance of their floors, which exhibit fractures, mesas and knobs. They represent a particular type of crater and are found on different planetary bodies [Schultz, 1976].

##### Filling

Craters can be filled once or multiple times with material in the modification stage, resulting in a flat crater floor. The filling is dissected by the fractures.

## Fractures

Fractures are crevices that intersect the crater floor and separate it into knobs of different size and shape. Five different types of fractures have been observed. Floors can be fractured preferentially along the rim (0). The fracturing can also start in a specific part of the crater (1). Often “puzzle piece” fracturing is observed (2). The knobs still fit together, but they are separated from each other. The crater has a strong fracturing (3), when the knobs do not coherently fit together. The crater is entirely fractured (4), if most of the floor consists of separated knobs [Schultz, 1976, Survey, 2014].

## Linear Features

Linear features are ridges and polygon-like structures inside the crater, mainly on the knobs.

## Mesas

Mesas are flat-topped mountains on top of knobs within the crater. Landslides can be found at their edges due to steep slopes [Press et al., 2003].

## Terraces

Terraces are stair-like surface features. They consist of rather flat surfaces and steep slopes that descend (ascend) to a lower (higher) part of the terrace [Survey, 2014].

## Uplift

Uplifted crater floors have increased elevation towards the center of the crater. The knobs are often tilted and partially raised towards the center. The central peak itself is no indicator for the uplift process. Craters with and without a central peak can be uplifted [Melosh, 1989, Press et al., 2003].

## 6.1.2. Exterior Surface Features

The following features are found outside the craters and are indications for the environment (Tab. 6.2).

### Boundary Area

The global dichotomy boundary region is located between the Martian highlands and lowlands. The boundary is defined by three parameters: elevation, crater density, and crustal thickness. The dominant surface elevation of the lowlands is -4 km. The elevation at the highlands peaks at 1.5 km. The abruptness of the elevation change varies along the boundary (e.g. Carr [2006]). The surface elevation between -3 and -1 km is the transition zone between the Martian highlands and lowlands and defined as the boundary region (Fig. 6.1). The boundary region is only defined by elevation for this research. The boundary region ranges in width from 250 km around Isidis up to 2,500 km in Arabia Terra. In the database, craters are considered to be influenced by the boundary area if they are located within this region.

## Channel

Channels are defined as intersections of the crater rim. They can be dendritic channels, sapping channels, outflow channels, tectonic grabens, and/or volcanic flows.

## Chaotic & Fretted Terrain Region

Chaotic terrains are areas defined by fractures and knobs. The knobs appear arc-shaped, tilted, and jumbled with respect to one another. The formation process involves collapse of material induced by removal of ice and water in the subsurface [Sharp, 1973, Zegers et al., 2010]. Large outflow channels and fluvial landforms originating from chaotic terrains support this hypothesis. A list of chaotic terrain regions is available by the International Astronomical Union (IAU). Fretted terrains are defined by Sharp [1973]. They show steep-walled and flat-topped upland remnants and fractures separating those units. These terrains formed likely due to water or ice on the surface and in the subsurface and subsequent collapse of material [Carr, 2006]. Chaotic and fretted terrains are shown in Fig. 6.2. In the database craters are considered to be influenced by chaotic or fretted terrain if they are located within the region of their occurrence.

## Ejecta

Ejecta is material that was ejected during the formation of an impact crater. Buried material is deposited around the crater in inverted stratigraphic order, due to the excavation [Melosh, 1989, Murawski and Meyer, 2004].

## Fluvial

The environment is considered fluvial [Murawski and Meyer, 2004] if outflow channels [Carr, 1996], gullies [Malin and Edgett, 2000], valley networks [Carr, 2006], flooding areas [Burr et al., 2002], dendritic systems, or fluvial channels can be found in the area surrounding the crater.

## Glacial

Indicators for a glacial [Murawski and Meyer, 2004] environment are terrain smoothening [Squyres and Carr, 1986], glaciers, lineated valley fills and pitted terrain between 30° and 60° longitude [Carr, 2006], fretted terrain [Sharp, 1973], and small-scale polygon fractures [Lachenbruch, 1970].

## Tectonic

The surrounding of the crater is influenced by tectonic activity, if tectonic structures (e.g. grabens, pit chains [Press et al., 2003]) can be found in immediate vicinity.

## Tectonic Areas

Tectonic areas contain geological features like graben systems, fossae, wrinkle ridges, and thrust faults. Coordinates for fossae on Mars are available within a database of IAU. Large graben systems were mapped based on the mapping done by Robert Anderson and published in Barlow [2008]. Tectonic areas are shown in Fig. 6.3. In the database, craters are considered to be influenced by tectonics if they are located directly in the tectonic area or within a distance of 100 km.

## Volcanic

A volcanic environment shows volcanoes, volcanic plains, flows, and ridges [Murawski and Meyer, 2004, Press et al., 2003] close to the crater.

## Volcanic Areas

Volcanic areas on Mars are summarized by Grott et al. [2013], that include ancient volcanism [Xiao et al., 2012], shield volcanoes [Baratoux et al., 2009] and low shield volcanoes [Hauber et al., 2009]. Additionally, TES basalt concentration data were used to identify basaltic materials [Bandfield et al., 2000]. These were used as proxy for recent volcanic events that have undergone extreme weathering. All information was collected in a volcanic map for Mars (Fig. 6.4). In the database craters are considered to be close to a volcanic region if they are located directly in the volcanic area or within a distance of 100 km.

## 6.2. Generating the Database

The spatial resolution and coverage of image data are essential for the observations of FFCs. This is because raw data quality directly affects the quality of the results. For each surface feature the most desirable instrument for each feature is shown in Tab. 6.1 & 6.2.

Complete spatial coverage of the surface is imperative for a global study. Here I use THEMIS, HRSC, and CTX data. The visual images help to identify properties of surface features. The accuracy of measurements and calculations will increase with a higher spatial resolution of images. For very small features (<25 m), CTX images must be utilized to acquire reliable results. This is especially true for the interior of the craters since HRSC cannot always provide the required resolution.

DTMs are required for analyzing the crater morphology. For the automated global research MOLA DTMs are used. To increase the quality of the results and the traceability for the user, it is necessary to record which input data are used for each tool (Tab. 6.1 & 6.2).

FFCs were surveyed on Mars by using THEMIS, HRSC and CTX data and were stored within the database as polygon and point features. Each FFC automatically received an ID, which is used as an identifier within GISs. Additionally, a NUMBER was assigned to every crater. The latitude (degree) and longitude (degree) of the crater center were also stored in the attribute table. If craters were already included in the official nomenclature of Mars, the NAME and REGION were added to the attribute table.

Observation of every crater was done manually in JMars. The feature definitions were leading parameters in assigning values to every column of the table (see Chapter 7). The data were stored in the shapefile format, which is also accessible with ArcGIS.

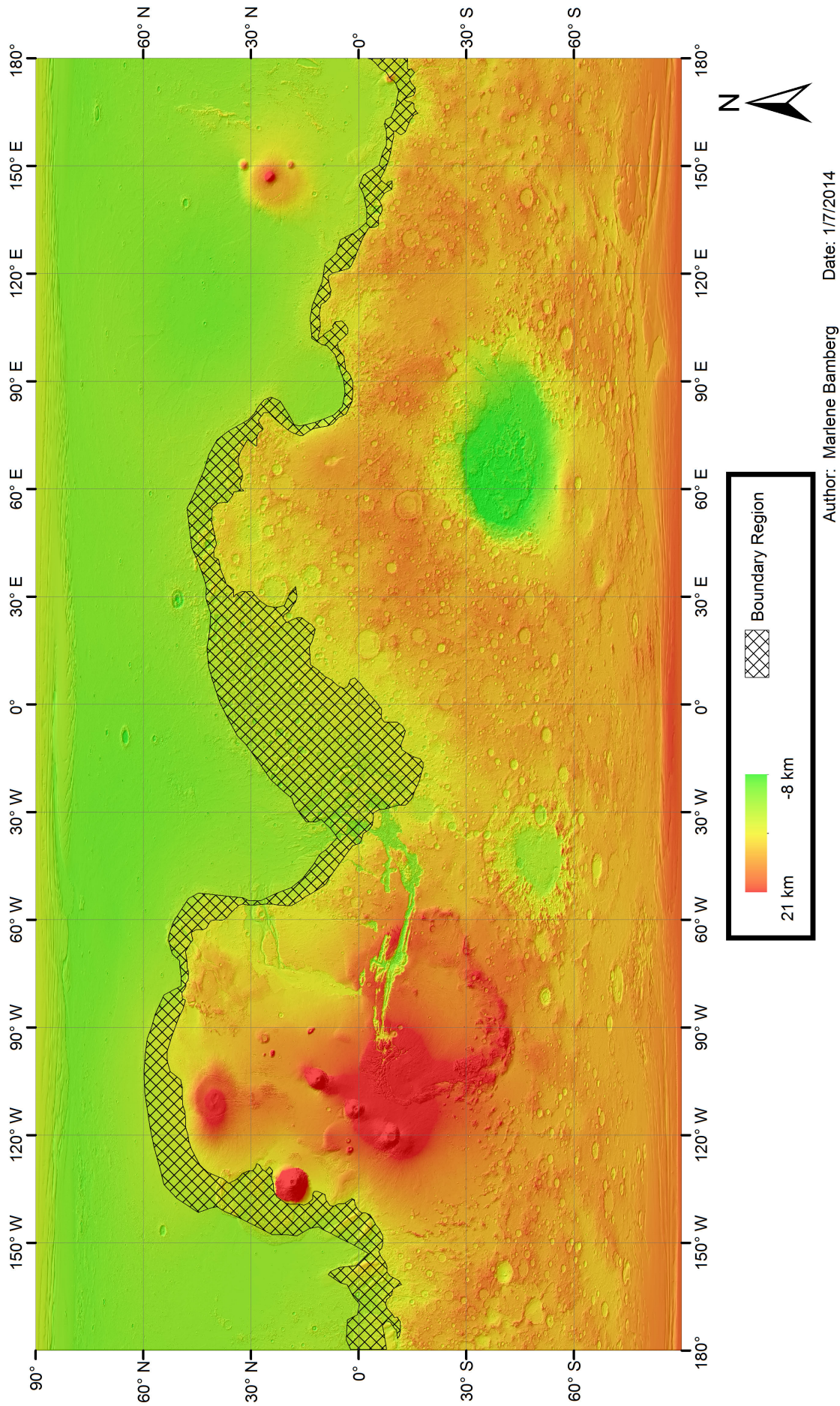


Figure 6.1.: The boundary region between -3 and -1 km is shown in a colored MOLA elevation map.

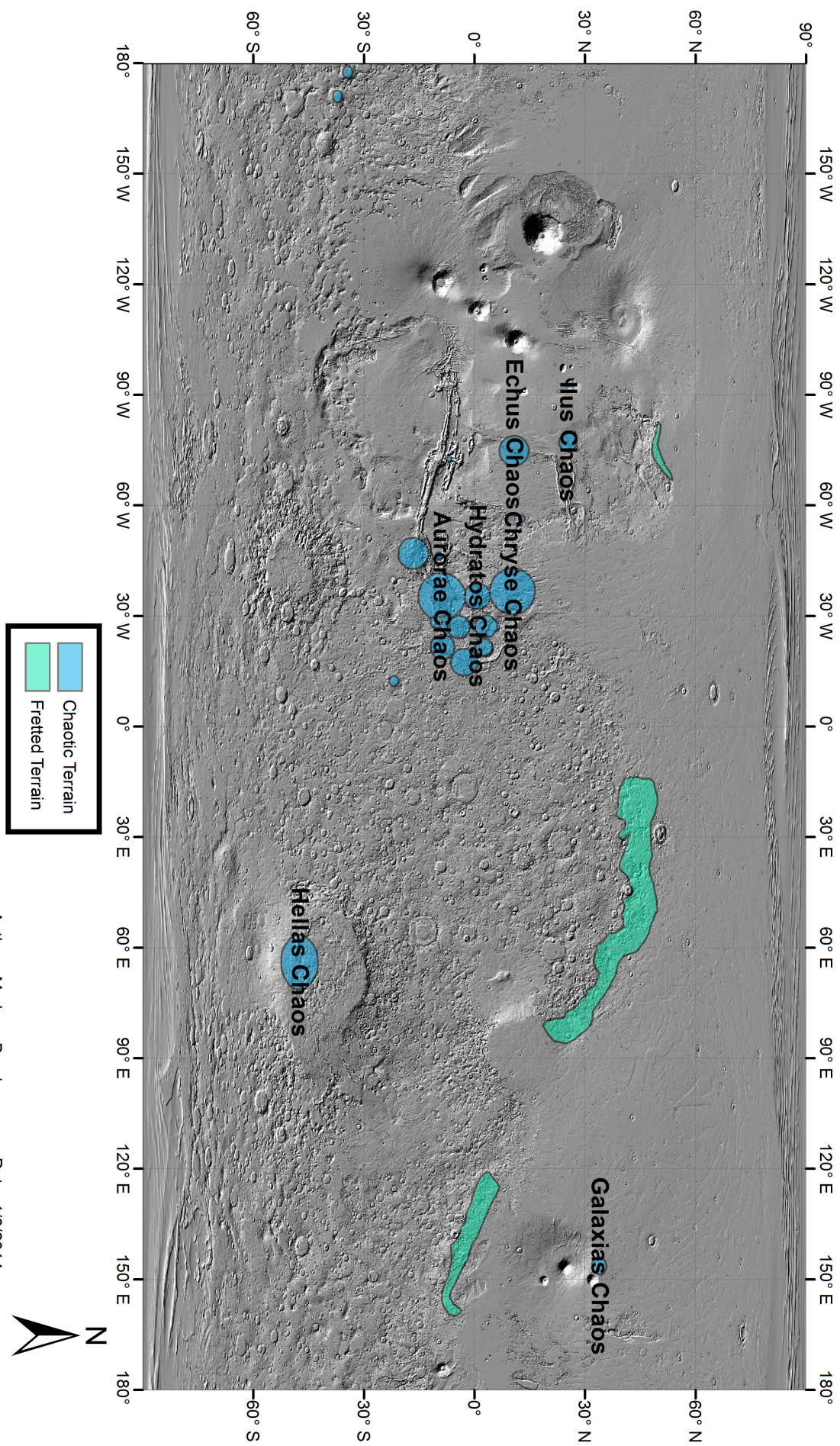


Figure 6.2.: Spatial distribution of chaotic and fretted terrain on Mars based on published lists of surface features of the IAU.

Author: Marlene Bamberg

Date: 1/6/2014



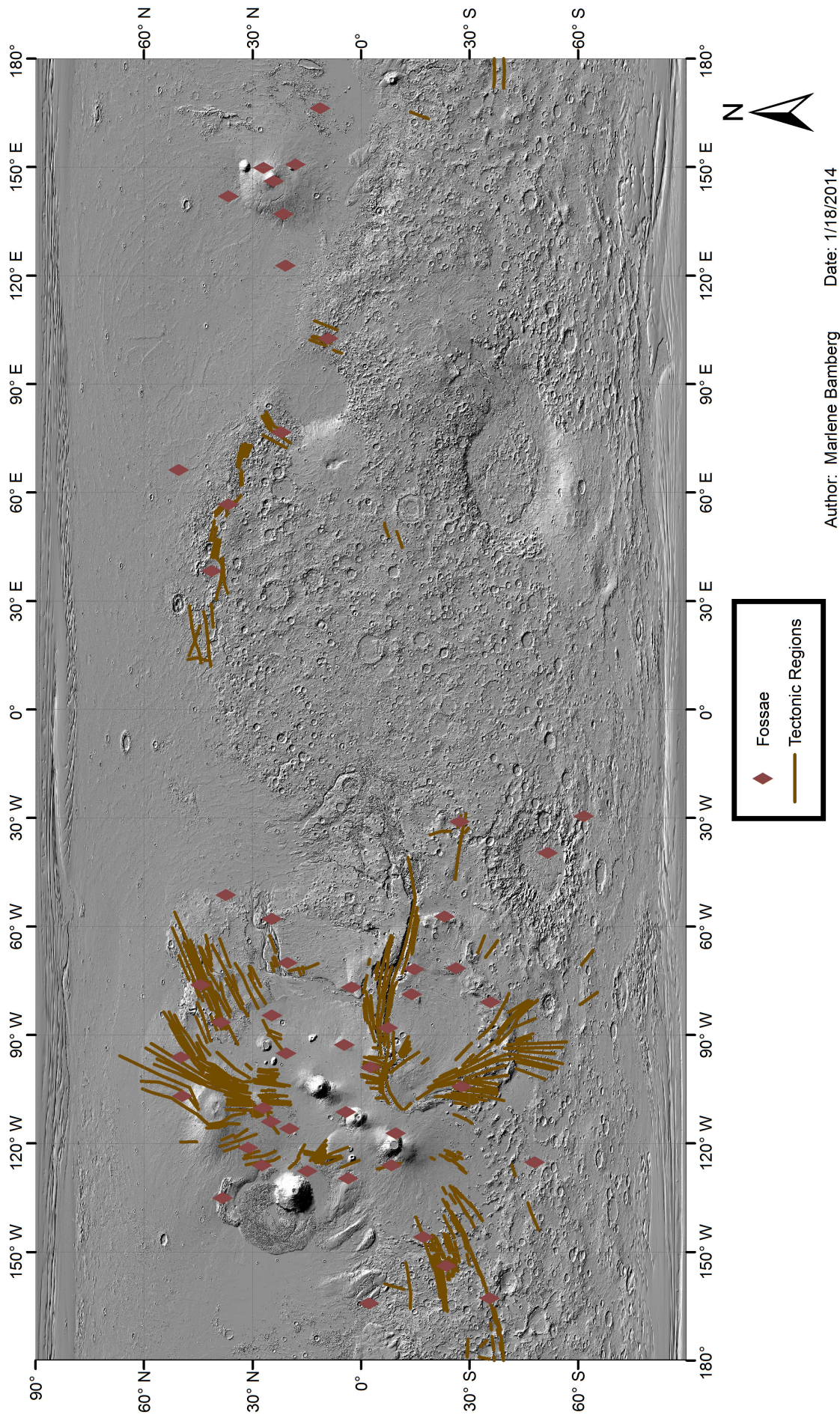


Figure 6.3.: The location of the fossae and the main graben systems of Mars.

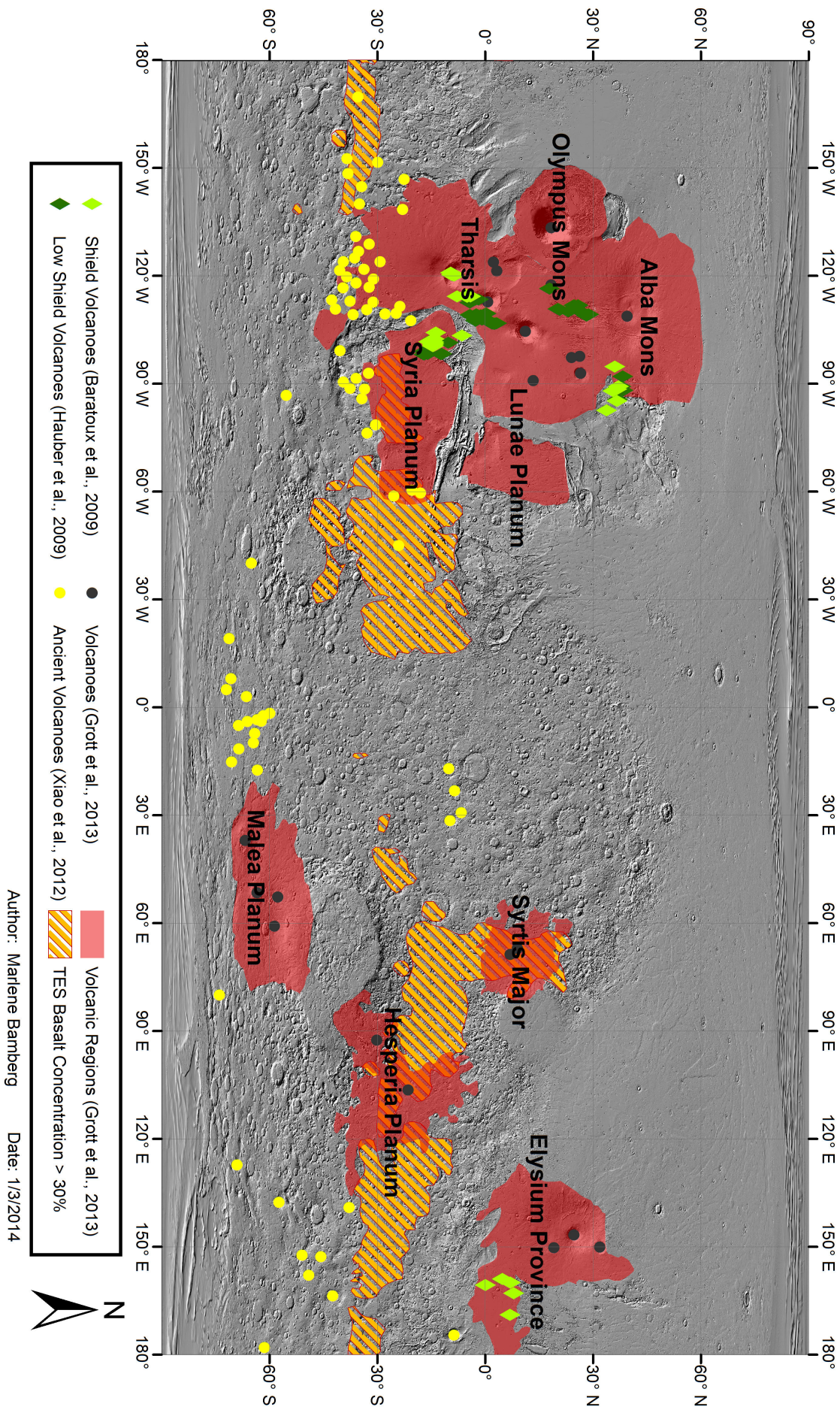
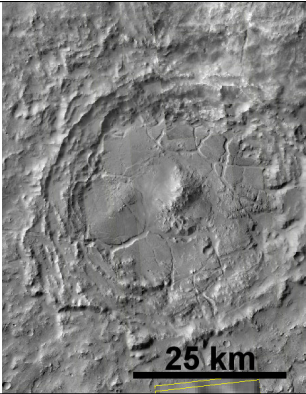
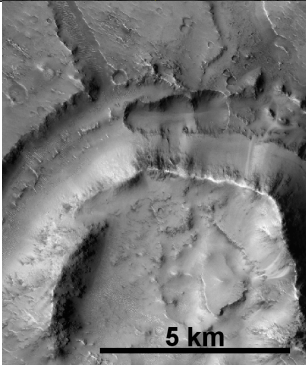
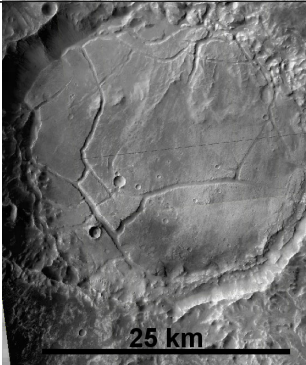
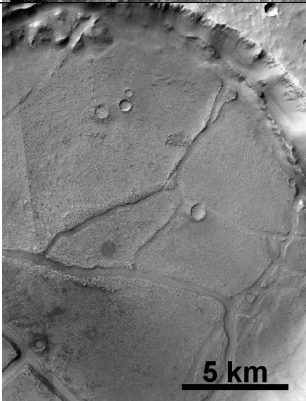

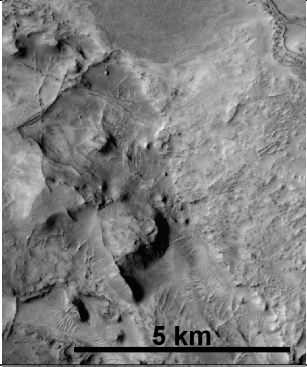
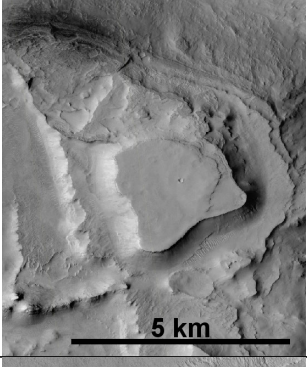
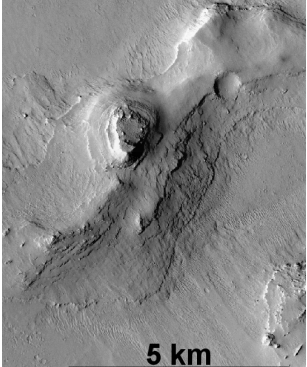
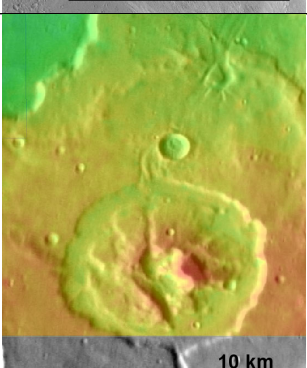
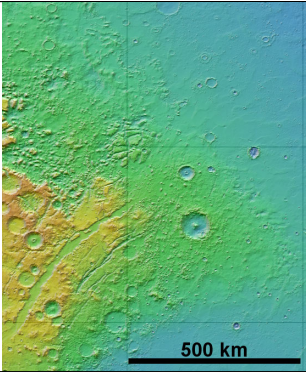
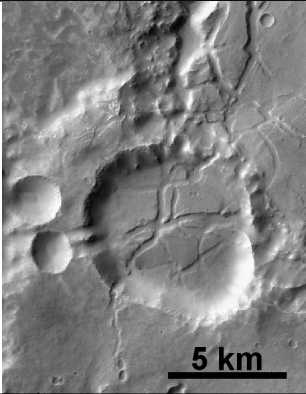




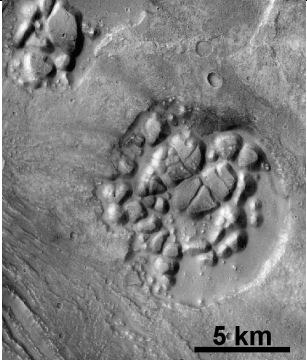
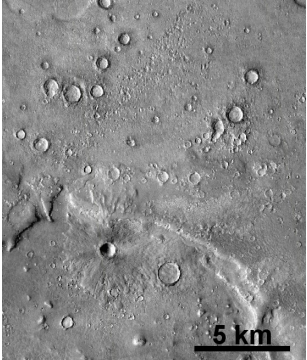
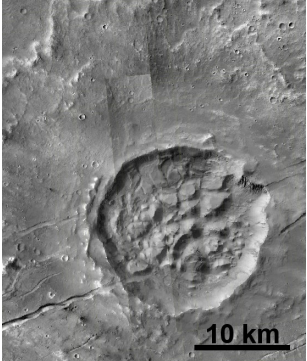
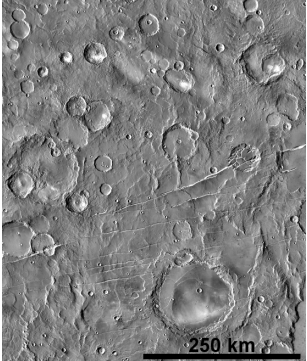
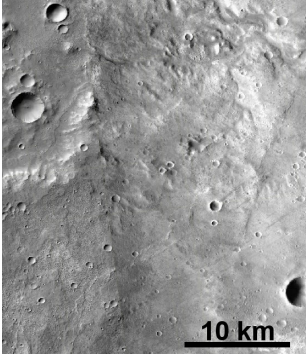
Figure 6.4.: Spatial distribution of volcanic areas on Mars. Shield volcanoes, low shield volcanoes, volcanoes, and ancient volcanoes are shown as point features. The volcanic regions and TES basalt concentration >30 % are represented as polygon features.


Feature	DB Name	Values	Source	Example
Central Peak	CENTRAL_PEAK	0 - no 1 - yes	THEMIS HRSC CTX	 A grayscale image of a Mars crater showing a prominent central peak. A scale bar at the bottom right indicates 25 km.
Depression	DEPRESSION	0 - no 1 - yes	CTX	 A grayscale image of a Mars crater with a distinct depression in the center. A scale bar at the bottom right indicates 5 km.
FFC	FFC	0 - no 1 - yes	THEMIS HRSC CTX	 A grayscale image of a Mars crater showing a feature with a flat floor and a central peak. A scale bar at the bottom right indicates 25 km.
Filling	FILLED	0 - no 1 - yes	HRSC CTX	 A grayscale image of a Mars crater with a flat, filled floor. A scale bar at the bottom right indicates 5 km.
Fractures	FRACTURING	0 - rim 1 - partial 2 - puzzle 3 - strong 4 - total	HRSC CTX	 A grayscale image of a Mars crater showing a complex fracture pattern on the rim and floor. A scale bar at the bottom right indicates 10 km.

Feature	DB Name	Values	Source	Example
Linear Features	LF	0 - no 1 - yes	CTX	
Mesas	MESAS	0 - no 1 - yes	HRSC CTX	
Terraces	TERRACES	0 - no 1 - yes	CTX	
Uplift	UPLIFT	0 - no 1 - yes	MOLA HRSC DTMs	

*Table 6.1.: Nine surface features inside the craters are stored and analyzed in the database. The corresponding column names in the database are listed. The values represent absence (0) or presence (1) for the surface features. The different types of fracturing are listed as numbers 0 to 4. Source indicates which image data have been used for the analyses (MOLA, THEMIS, HRSC, CTX). The image gives an example for each important surface feature.*

Feature	DB Name	Values	Source	Example
Boundary Area	B_AREA	0 - no 1 - yes	DB	
Channel	CHANNEL	0 - no 1 - one 2 - >one	HRSC CTX	
Chaotic & Fretted Terrains	CF_AREA	0 - no 1 - yes	DB	
Ejecta	EJECTA	0 - no 1 - yes 2 - N/A	THEMIS HRSC	

Feature	DB Name	Values	Source	Example
Fluvial	FLUVIAL	0 - no 1 - yes	HRSC CTX	
Glacial	GLACIAL	0 - no 1 - yes	HRSC CTX	
Tectonic	TECTONIC	0 - no 1 - yes	HRSC CTX	
Tectonic Area	TEC_AREA	0 - no 1 - yes	DB	
Volcanic	VOLCANIC	0 - no 1 - yes	THEMIS HRSC CTX	

Feature	DB Name	Values	Source	Example
Volcanic Area	VOL_AREA	0 - no 1 - yes	DB	

*Table 6.2.: Ten surface features outside the crater are stored and analyzed in the database. The corresponding column names in the database are listed. The values represent absence (0), presence (1), or lack of data and uncertainty (2) for the surface features. Source indicates which image data (or DB for a database) have been used for the analyses (THEMIS, HRSC, CTX). The image gives an example for each important surface feature.*





# 7. Automated Tools for Analysis of FFCs

This chapter includes the development of automated classification, calculation, and measurement tools, which are needed for the statistical analysis of FFCs. These automated tools are combined with user-based decisions, resulting in a semi-automated geoscientific analysis.

## 7.1. Purpose

The origin of FFCs on Mars will be determined by using an automated, statistical analysis based on an existing database.

The tools provide parameters that were obtained by defined geostatistical techniques. Hence, the tools guarantee a consistent quality of results. This also includes achieving reliable, comparable, and usable results, but also reducing the time and effort. The analysis should be uniform for all craters to obtain comparable and meaningful results. It should also be reproducible to perform the same analysis multiple times in order to increase the reliability and quality of the results. Additionally, the analysis should be faster than the qualitative analysis, in order to achieve higher performance in analyzing large amounts of data. It should also be applicable on a global scale, so that results for all FFCs on Mars are achieved.

## 7.2. Automation and User-Based Analysis

In order to perform global analyses fast, different automation principles and approaches are discussed here.

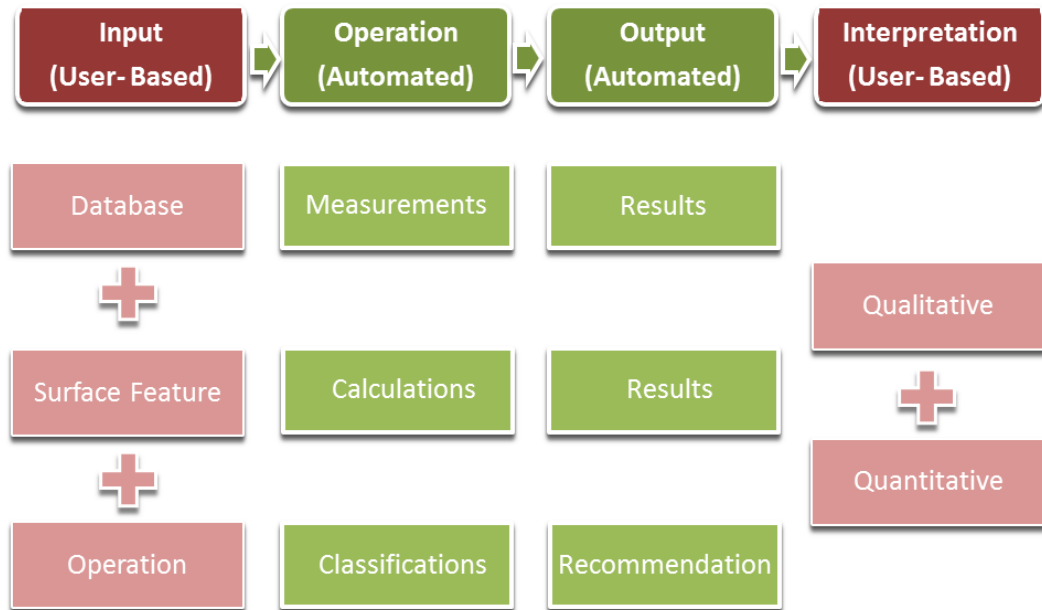
Analysis and interpretation of geological and geomorphological surface features in planetary science are often user-based only. As a result, the analysis is a subjective view of the user and difficult to reproduce and compare to other analyses. The process of analyzing also consumes time, effort, knowledge, and workforce [O'Sullivan and Unwin, 2010].

For these reasons, automated tools are becoming more and more important in data analysis. At the same time, automation is not considered to be the best option for data analysis, due to the loss of quality and potential for error [Gomasca, 2004, O'Sullivan and Unwin, 2010].

Semi-automation is a solution to these problems. By combining automated parts with user-based decisions, tasks become much easier and faster, but the user is still able to include personal expertise.

Based on this idea, I developed analytical tools for ArcGIS (Fig. 7.1). The tools are based on definitions and rules for the classification of FFCs. The definition of important key parameters and setup of rules requires background knowledge and hence, needs to be done by an expert. The defined tools do not operate automatically, the user must decide which tools are the most useful on which surface

features. Once the decision is made, the tools conduct their analyses automatically and provide independent results. The tools combine user-based decisions and knowledge with automated surface analyses. Time-consuming measurements, calculations, and classifications are done automatically, providing a fast, comparable and reproducible, quantitative analysis of surface morphologies. Classification tools are also used in Earth-based research (e.g. Horacio and Ollero [2011]).



*Figure 7.1.: User-based and automated tasks are shown here. The input is user-based. The user has not only to provide the database, but decide which surface feature should be analyzed with which operation. The operation itself is automated. This means the measurements, calculations, and classifications are done automatically by the program. The output is also presented automatically in table format; results and recommendations for the classification are provided to the user. The interpretation is, again, user-based. Qualitative and quantitative analyses are used to support geoscientific interpretation.*

### 7.3. Hierarchic Structure

The tools are organized in a hierarchic order and follow the principle of dependency. There are three dependency levels. These can be seen for each tool in section 7.4. The tools are divided into classifications (level III), calculations (level II), and measurements (level I).

#### Classifications

Classifying the surface morphology is the primary objective of our quantitative research. The features can only be classified if there are defined rules for classification. The tools compare the feature parameters to the required parameters for the classification. According to the results the features are classified. The classification is

the final level (level III) of the quantitative analysis, because it requires information of level I and II.

## Calculations

The calculations provide more information about the surface morphology. Formulas, based on modeling done by various researches, are used to calculate ratios and feature parameters, which are not visible on the surface. The calculations are level II: they provide input for level III, but also rely on level I values, which need to be measured first.

## Measurements

Measurements characterize the surface features and are also the basis for geoscientific analysis. Measurements are shown with dependency level I, because they rely on the image data, but no further information.

For a better overview measurements, calculations, and classifications for surface features inside and outside the crater are separated from each other and shown in Fig. 7.2 and 7.3. There are tools that are used both inside and outside the craters, but there also inside-specific, as well as outside-specific, tools.

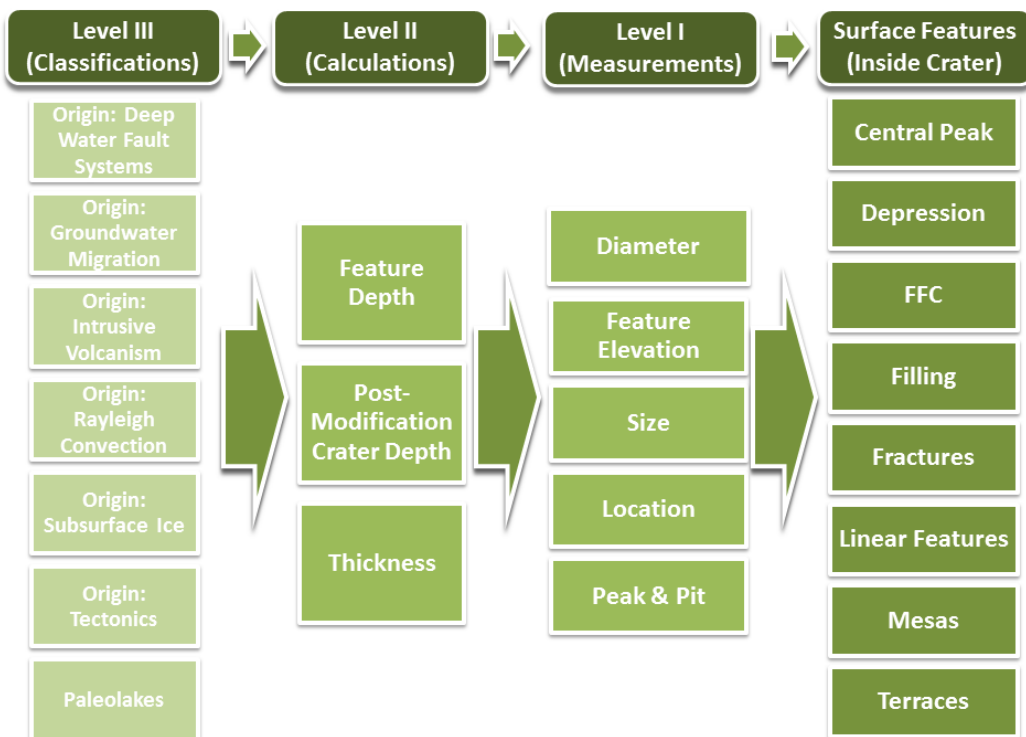


Figure 7.2.: Hierarchical structure for interior classifications. In order to obtain the classifications certain calculations and measurements for the surface features are required.

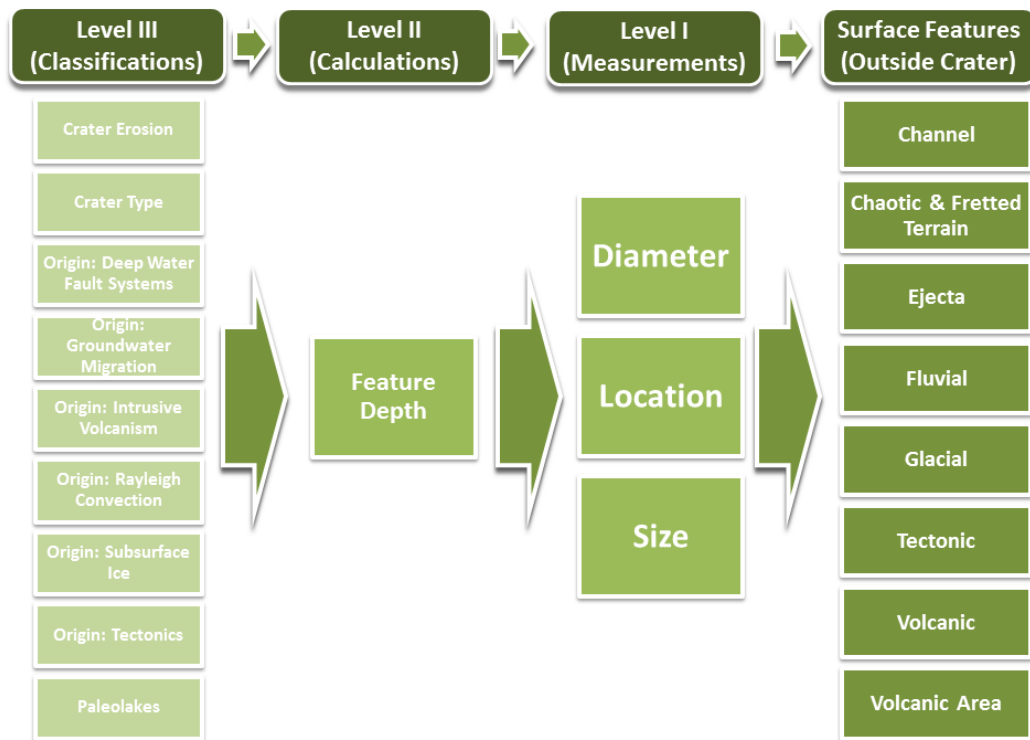


Figure 7.3.: Hierarchical structure for exterior classifications. In order to obtain the classifications certain calculations and measurements for the surface features are required.

## 7.4. Tools

The developed tools are listed and important parameters are shown here. The list contains the name of the tool and a detailed description of the purpose, usage, and explanation of the tool. The definition sets the rules that the tool is based on. The tools can be applied to certain surface features for analyzing FFCs. The input lists the data needed for the tool. Without these data the tool cannot be run. The output shows the results of the tools, which are stored in the database. The dependency levels are shown for each tool and can be divided into measurements, calculations, and classifications. The database name shows the abbreviation of the parameters within the database. The source gives the reference for already existing tools or formulas used.

### 7.4.1. Measurements

#### Diameter

**Description** The diameter of a surface feature is measured with this tool. It is a simple measurement, but very important for classifications concerning impact crater size. The crater diameter is measured based on the polygon size. The value is stored in the attribute table.

**Definition** The diameter is a straight line that passes through the center of a circle connecting two points on the circumference. The diameter of a crater is obtained by fitting a circular polygon to the crater rim (Fig. 7.4). If the area ( $A$ ) is known, it can be also calculated by:

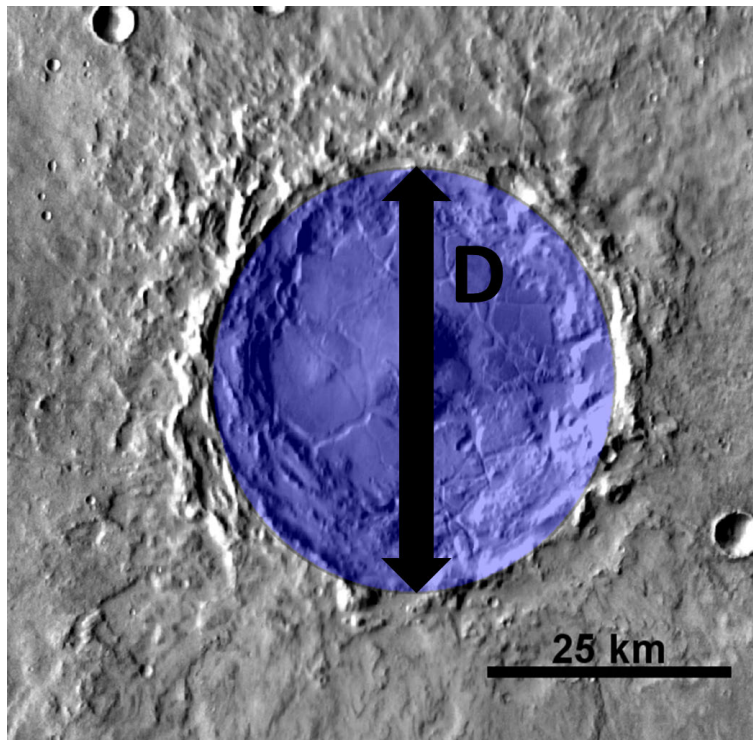


Figure 7.4.: The diameter of the impact craters are measured based on the polygon size.

$$D = 2 * \sqrt{\frac{A}{\pi}}$$

Applied to	Impact Crater
Input	Polygon
Output	km
Level	I
Database	D (Diameter)
Source	ESRI [2013]

### Feature Elevation

Description	This tool calculates the average feature elevation in an area by using DTM elevations. The average elevation is a basic parameter for other calculations, e.g. thickness and volume. It also provides the possibility to compare features to each other. The averaged value is stored in the database.
Definition	The average feature elevation is measured within the GIS. In the ArcToolbox within the spatial analyst tool set a zonal statistics tool can be found. The tool links the raster DTM to the polygon and calculates the mean values for the elevation (Fig. 7.5).
Applied to	Crater Rim, Crater Floor, Knobs, Fractures, Central Peak
Input	DTM, Polygon

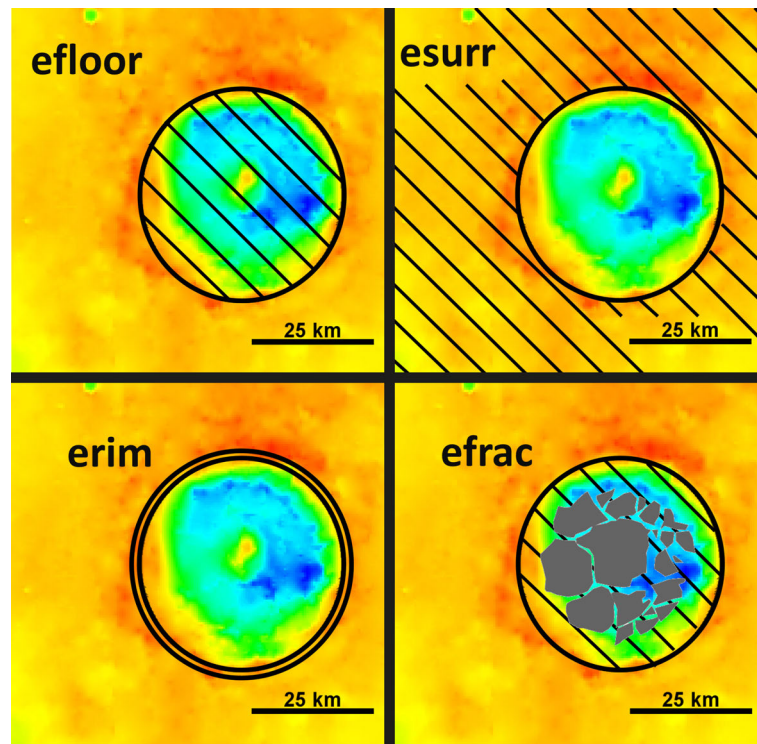


Figure 7.5.: The average elevation of the crater floor, surrounding area, crater rim, and the fractures are measured from the DTM.

Output	m
Level	I
Database	efloor (Crater Floor Elevation), erim (Crater Rim Elevation)
Source	ESRI [2013]

### Location

Description	The location of surface features is measured and shown in decimal degree coordinates with this tool. Coordinates are used for spatial distribution analyses. The latitude and longitude values at the centroid of every feature are obtained and stored in the database.
Definition	Within the ArcGIS toolbox and the data management tool set. A tool for adding xy-coordinates is available. For every feature of a shapefile new columns containing the latitude and longitude coordinates are created (Fig. 7.6). The image data must be georeferenced to obtain the correct latitude and longitude values.
Applied to	Impact Crater
Input	Polygon, Point
Output	Decimal Degree
Level	I
Database	LAT (latitude), LON (longitude)

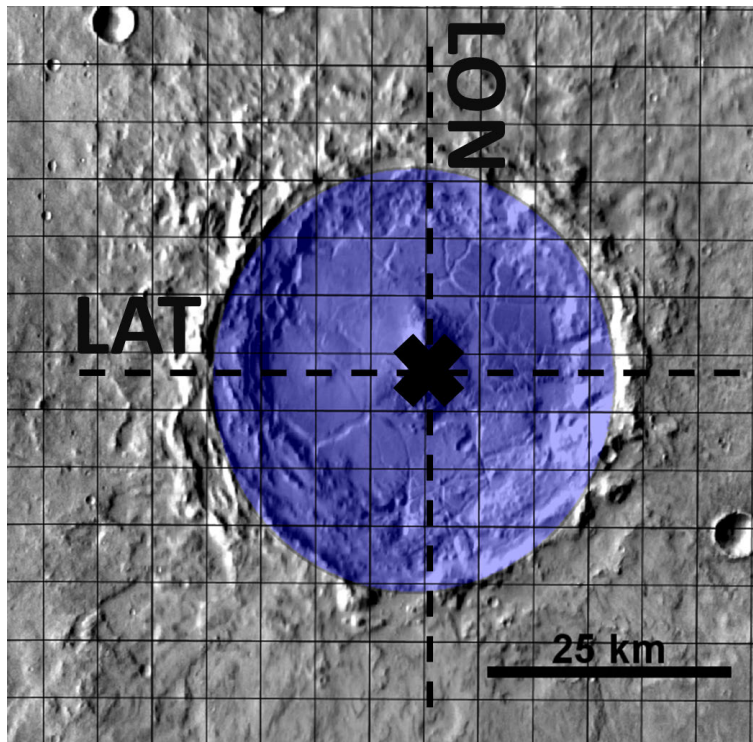


Figure 7.6.: The latitude and longitude are measured in decimal degree at the center of the crater polygon.

Source ESRI [2013]

### Peak & Pit

**Description** This tool finds the lowest and highest point in a surface unit or within parts of a unit. It identifies the minimum or maximum elevation of the surface. Knowledge about minimum and maximum elevation is important for the geoscientific analysis. The tool also shows variations in surface elevation compared to the averaged values. The highest point can provide information about maximum infilling elevation. In contrast, the lowest point can give hints about the erosion depth and deposited material. Depending on the surface feature, the knowledge of the highest or lowest location is more important. For some features just one of the measurements will lead to useful information. The minimum and maximum values are stored in the database.

**Definition** The highest and lowest position by raster tool is available within the spatial analyst in the ArcToolbox. The tool will find the lowest and highest value of the raster data set (Fig. 7.7). It is possible to crop the raster image to the size of the polygon of interest and automatically measure the highest or lowest position within.

**Applied to** Crater Floor, Crater Rim, Fractures, Knobs

**Input** DTM, Polygon

**Output** m

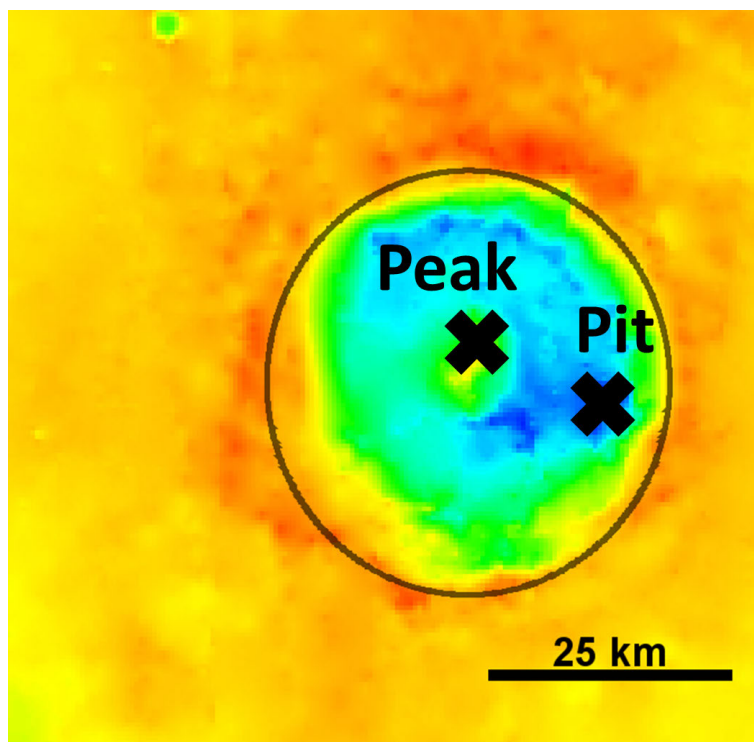


Figure 7.7.: The maximum (*peak*) and minimum (*pit*) elevation within the crater is measured in the DTM.

Level	I
Database	minfloor (Minimum Crater Floor Elevation), maxfloor (Maximum Crater Floor Elevation), ...
Source	ESRI [2013]

### Size

Description	This tool measures the area covered by a specific surface unit. Size measurements are needed for various calculations and give additional information about the surface features. The area is calculated and shown in the attribute table.
Definition	The area is the space covered by the impact crater (Fig. 7.8). It is measured within the GIS.
Applied to	Impact Crater, Crater Floor, Fractures, Knobs, Channels
Input	Polygon
Output	km <sup>2</sup>
Level	I
Database	AREA
Source	ESRI [2013]



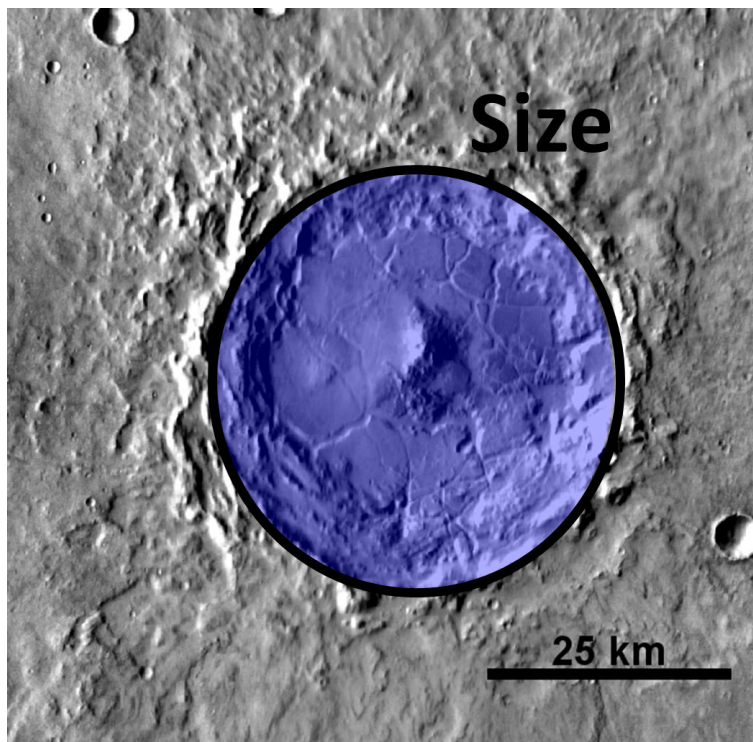


Figure 7.8.: The area that is covered by the impact crater is measured.

## 7.4.2. Calculations

### Feature Depth

**Description** This tool calculates the average feature depth in an area by using elevation values measured within the DTM. The average depth is a basic parameter for other calculations, e.g. thickness and volume. It also provides the possibility to compare features to each other. The output is presented within the attribute table.

**Definition** The depth of the crater floor needs to be calculated based on elevation measurements (Fig. 7.9):

$$d_{Ob} = e_{rim} - e_{floor}$$

**Applied to** Crater Rim, Crater Floor, Knobs, Surrounding Area, Fractures, Central Peak

**Input** erim, efloor

**Output** m

**Level** II

**Database** dOb (Crater Floor Depth), ...

**Source** ESRI [2013]

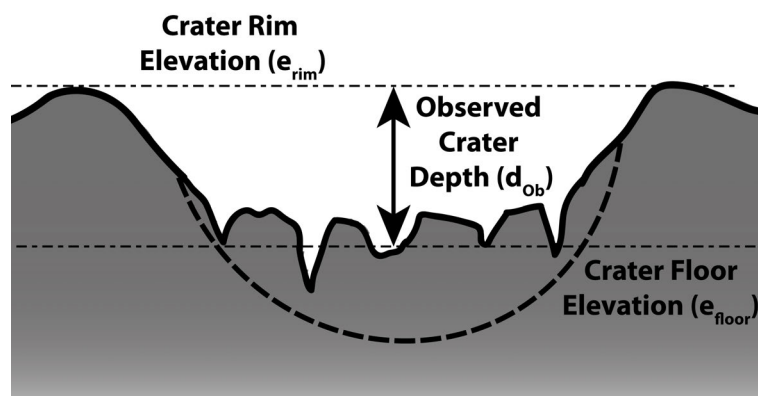


Figure 7.9.: The depth of surface features is calculated based on the measured surface feature elevations.

### Post-Modification Crater Depth

**Description** This tool calculates the post-modification crater depth, which is the depth of the impact crater shortly after it was formed. This depth can be used to analyze the crater morphology relating to erosion, degradation, and deposition of materials inside craters. The post-modification crater depth is stored in the database for each crater.

**Definition** The post-modification crater depths depends on the crater diameter. The transition between simple (<7 km) and complex (>7 km) crater diameters is a key parameter for calculating the original crater cavity (Fig. 7.10). I used the results and equations of previous research [Boyce and Garbeil, 2007, Melosh, 1989, Tornabene et al., 2013].

The depth of a simple crater is calculated with the equation:

$$d_r = 0.276 * D^{0.68}$$

With complex impact craters the equation changes to:

$$d_r = 0.357 * D^{0.52}$$

**Applied to** Impact Crater

**Input** D

**Output** km

**Level** II

**Database** dr (Post-Modification Crater Depth)

**Source** Author, Boyce and Garbeil [2007], Melosh [1989], Tornabene et al. [2013]

### Thickness

**Description** This tool calculates the thickness of deposited materials. In relation with surface age, it can provide information about deposition or erosion rates as well as surface processes that have occurred. The

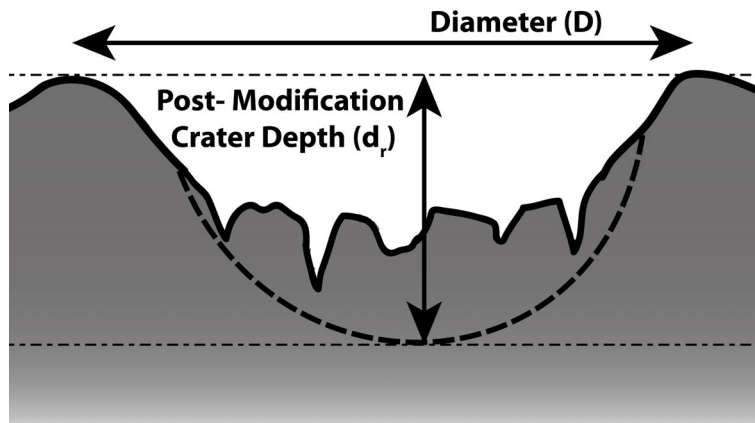


Figure 7.10.: The post-modification crater depth is calculated based on the measured diameter and the equations established by Tornabene et al. [2013].

tool only provides a rough estimate of the thickness of the deposited materials. The morphologies covered by sediments in the subsurface are not visible and, therefore, cannot be taken into account. The values are stored within the database.

**Definition** The calculation for the depth of infilling is based on modeling by Boyce and Garbeil [2007], Tornabene et al. [2013]. To calculate the thickness of the infilling, ( $t_I$ ), the average crater floor height, ( $d_{Ob}$ ), is subtracted from the post-modification crater depth, ( $d_r$ ) (Fig. 7.11):

$$t_I = d_r - d_{Ob}$$

**Applied to** Infilling

**Input**  $d_{Ob}$ ,  $d_r$

**Output** m

**Level** II

**Database**  $t_I$  (Thickness of Infilling)

**Source** Author, Tornabene et al. [2013]

### 7.4.3. Classifications

#### Crater Erosion

**Description** This tool classifies craters into five different erosion types based on the presence of fluvial erosion and the ejecta blanket. The tool helps to identify highly eroded craters, but can also identify craters that have undergone almost no weathering. All the required parameters are stored in the database and they are classified by an attribute query.

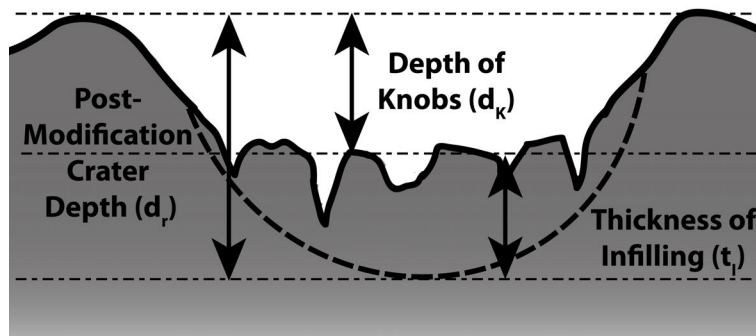


Figure 7.11.: The thickness of infilling is calculated based on surface feature depths.

**Definition** The crater erosion is based on the ejecta and fluvial erosion around the impact crater. The research was done for two regions on Mars by Craddock and Howard [2002] and Mangold et al. [2008]. They introduced three types of crater erosion levels.

Strongly degraded craters are classified as type I. Fluvial erosion has weathered the crater and no ejecta blanket is present, due to highly eroded terrain. Type II represents gently degraded craters with a high level of fluvial erosion, but the ejecta blanket still exists. Type III are fresh craters. There is no evidence for fluvial activity and the ejecta blanket is un-eroded. The crater erosion levels have been slightly adapted to fit Martian craters for global research. I added the option of having no fluvial erosion and no ejecta blanket and defined it as type IV. With missing information or uncertainties regarding the ejecta or fluvial erosion the crater is classified as type V.

Applied to	FFC
Input	EJECTA, FLUVIAL
Output	1 (Type I Crater), 2 (Type II Crater), 3 (Type III Crater), 4 (Type IV Crater), 5 (Type V Crater)
Level	III
Database	EROSION
Source	Author, Craddock and Howard [2002], Mangold et al. [2008]

### Crater Type

**Description** The tool shows if the craters within the database are considered simple, complex, or multi-ring craters. The diameter is important to conduct further analysis, e.g. Post-Modification Crater Depth.

**Definition** The classification of impact crater sizes was done by [Melosh, 1989]. Simple craters range to a diameter of 7 km and are marked as type 1 craters in the database. Complex craters have a diameter ranging

from 7 km to 100 km and are marked as type 2 craters. Multi-ring complex craters are considered to have a diameter larger than 100 km and are defined as type 3 craters.

Applied to	FFC
Input	D (Diameter)
Output	1 (Simple Crater), 2 (Central Peak Complex Crater), 3 (Multi-Ringed Complex Crater)
Level	III
Database	C_TYPE
Source	Author, Melosh [1989]

### Origin: Deep-Water Fault Systems

**Description** Polygonal deep-water fault systems are a possible origin for floor fracturing. This tool uses statistical prediction to obtain the probability of this origin model. The probability helps the user identify the potential origin of fracturing based on operational values and rules. For this model, a glacial and fluvial environment, including a paleolake of at least 500 m water depth is essential. The more key parameters are present inside and outside a crater, the higher the index value for this origin type is. Consequently, the probability for this origin is also higher.

**Definition** Polygonal deep-water fault systems occur in the following environment: For this model a standing body of water (closed basin lake) with a water depth >500 m is needed [Moscardelli et al., 2012]. Terraces support the existence of a paleolake and linear features inside the crater show potential small scale polygons. The crater infilling must to be fine grained material, which forms regularly distributed knobs and polygonal fracturing patterns (fracturing type III, IV).

Channels intersecting the crater rim are necessary for the water supply. Glacial and fluvial features should be found outside the crater to support this model. A high level of erosion is also needed for increasing the fracturing size. Tectonic and volcanic features should be absent.

This tool has a maximal index value of 12, which corresponds to a 100 % probability that fracturing occurred according to this model.

Applied to	FFC
Input	FRACTURING, LF, PALEOLAKE, TERRACES, CHANNEL, EROSION, FLUVIAL, GLACIAL, TECTONIC, VOLCANIC, erim
Output	Index, %
Level	III
Database	O_DWFS, O_DWFS_PR

Source Author, Moscardelli et al. [2012]

### Origin: Groundwater Migration

**Description** This tool uses statistical prediction to obtain the probability of a groundwater migration origin for the fracturing within the FFC. The probability helps the user to identify the potential origin of fracturing based on operational values and rules. For the origin type of groundwater migration fluvial features and channels are important. Every parameter that is in agreement to the classification rules increases the index value for this origin. The higher the index value, the higher the probability of this origin type.

**Definition** For the groundwater migration origin type crater depressions and a potential paleolake should be present. Fracturing starting at one part of the crater (type I), or being present in most (type III) or the entire (type IV) crater, supports this model. The observed minimum fracturing elevation should be smaller than the post-modification crater depth.

Outside the crater channels, fluvial features and fluvial erosion should be present. Tectonic features must be absent to clearly identify fluvial features. The crater should be located close to volcanic areas and the dichotomy boundary of Mars, to ensure a rapid water flow in the subsurface. The crater should have a diameter larger than 100 km and is, consequently, defined as a multi-ringed complex crater.

This tool has a maximal index value of 11, which corresponds to a 100 % probability that fracturing occurred according to this model.

**Applied to** FFC

**Input** DEPRESSION, FRACTURING, PALEOLAKE, B\_AREA, CHANNEL, EROSION, FLUVIAL, TECTONIC, C\_TYPE, minfloor, erim, dr, VOL\_AREA

**Output** Index, %

**Level** III

**Database** O\_WATER, O\_WATER\_PR

**Source** Author, Sato et al. [2010]

### Origin: Intrusive Volcanism

**Description** This tool uses statistical prediction to obtain the probability of a volcanic origin for the fracturing within the FFC. The probability helps the user to identify the potential origin of fracturing based on operational values and rules. For this origin type volcanic features are of high importance. Each crater in the database will be analyzed regarding set surface parameters. The more required features found, the higher the index value is and thus the probability of this origin is also higher.

Definition	<p>The parameters inside the crater that support intrusive volcanism are depressions within the fractures, “puzzle pieces” fracturing (type II), and uplift of the crater floor.</p> <p>Outside the crater there should be no signs of erosion, fluvial, glacial, tectonic structures, or a potential paleolake. The basalt concentration, based on the TES-instrument data, should be higher than 5 %. Volcanic features should be present around the crater and the crater should be located close to a volcanic area.</p> <p>This tool has a maximal index value of 11, which corresponds to a 100 % probability that fracturing occurred according to this model.</p>
Applied to	FFC
Input	DEPRESSION, FRACTURING, PALEOLAKE, UPLIFT, EROSION, FLUVIAL, GLACIAL, TECTONIC, VOLCANIC, TES_BASALT, VOL_AREA
Output	Index, %
Level	III
Database	O_VOL, O_VOL_PR
Source	Author, Jozwiak et al. [2012], Schultz [1976]

### Origin: Rayleigh Convection

Description	<p>This tool uses statistical prediction to obtain the probability of the Rayleigh convection model. The probability helps the user to identify the potential origin of fracturing based on operational values and rules. For this model not only are glacial and fluvial environments essential, but also the location of the crater. It needs to serve as a natural water sink between <math>\pm 40^\circ</math> latitude. The more key parameters present inside and outside a crater, the higher the index value for this origin type is. Consequently, the probability for this origin is also higher.</p>
Definition	<p>With this model, regularly distributed knobs (type III), linear features and/or polygonal patterns should develop. An open or closed basin lake also supports this model. The crater infilling and surrounding should consist of water-rich sediments with a thickness between 1,100 and 1,500 m. A permafrost layer must also be present in the subsurface.</p> <p>The crater should be located between <math>\pm 40^\circ</math> latitude. A glacial and fluvial environment supports this model. A high level of erosion is necessary to increase the fracturing size. Tectonic and volcanic features should be absent.</p> <p>This tool has a maximal index value of 10, which corresponds to a 100 % probability that fracturing occurred according to this model.</p>
Applied to	FFC

Input	FRACTURING, LF, PALEOLAKE, EROSION, FLUVIAL, GLACIAL, TECTONIC, VOLCANIC, LAT, tI
Output	Index, %
Level	III
Database	O_RCON, O_RCON_PR
Source	Author, Wenrich and Christensen [1993]

### Origin: Subsurface Ice

Description	<p>This tool uses statistical prediction to obtain the probability of a subsurface ice origin for the fracturing within and around the FFC. The probability helps the user to identify the potential origin of fracturing based on operational values and rules. For this origin type fluvial features and the crater infilling need to be analyzed in detail. The more required features found, the higher the index value is and thus the probability of this origin is also higher.</p>
Definition	<p>This model is supported by the occurrence of the following surface features: the fracturing differs from “puzzle pieces” to fracturing that destroyed most or the entire crater floor (type 2,3,4), due to subsurface melting. Outflowing water can move and tilt the knobs within the crater, resulting in a chaotic distribution of knobs.</p> <p>The crater should be located close to the boundary area and chaotic or fretted terrains on Mars. Channels and fluvial or glacial erosion should be present close to the crater. Volcanic and tectonic features should be absent. The infilling material should consist of high porosity infilling, and therefore, water or ice-rich sediments. Furthermore, the infilling layer must have a thickness of 3.5 to 4.0 km [Schumacher and Zegers, 2011]. This fracturing type is more probable at large crater diameters (type 3).</p> <p>This tool has a maximal index value of 10, which corresponds to a 100 % probability that fracturing occurred according to this model.</p>
Applied to	FFC
Input	FRACTURING, B_AREA, CHANNEL, CF_AREA, FLUVIAL, GLACIAL, TECTONIC, VOLCANIC, C_TYPE, tI
Output	Index, %
Level	III
Database	O_ICE, O_ICE_PR
Source	Author, Massé et al. [2008], Schumacher and Zegers [2011], Zegers et al. [2010]



**Origin: Tectonics**

Description	This tool uses statistical prediction to obtain the probability of a tectonic origin for the fracturing within and around the FFC. The probability helps the user to identify the potential origin of fracturing based on operational values and rules. For this origin type, large scale fractures due to tectonic features are important. The more required features found, the higher the index value is and thus the probability of this origin is also higher.
Definition	<p>Inside the crater, depressions and various types of fracturing (type I, II, III, IV) support the model of tectonic origin of FFCs.</p> <p>Tectonic systems and large scale fractures must be present both inside the crater and in the surrounding area. Channels due to out-flowing material and a fluvial environment also fit into this model of fracturing. Volcanic features should be absent to clearly identify this type of origin.</p> <p>This tool has a maximal index value of 7, which corresponds to a 100 % probability that fracturing occurred according to this model.</p>
Applied to	FFC
Input	DEPRESSION, FRACTURING, CHANNEL, FLUVIAL, TECTONIC, TEC_AREA, VOLCANIC
Output	Index, %
Level	III
Database	O_TEC, O_TEC_PR
Source	Author, Hanna and Phillips [2006], Smrekar et al. [2004]

**Paleolakes**

Description	This tool classifies the crater according to the amount of channels ranging into or out of the crater. This information supports the user to easily identify craters which could have supported the development of closed and open basin lakes. The required information is stored in the database and an attribute query classifies the craters accordingly.
Definition	Impact crater basins can be classified by the amount of channels ranging into and out of the crater [Aureli et al., 2013, Cabrol and Grin, 1999]. I assume there was no paleolake present if there are no channels around the crater. This is shown as type 0 in the database. If there is one channel, the crater is considered to be a closed basin lake and, therefore, may have had a paleolake. This is marked as type 1 in the database. If there are multiple channels leading into or out of the crater, then it is considered an open basin lake and recorded as type 2 in the database.
Applied to	FFC

Input	CHANNEL
Output	0 (no basin lake), 1 (closed basin lake), 2 (open basin lake)
Level	III
Database	PALEOLAKE
Source	Author, Aureli et al. [2013], Cabrol and Grin [1999]

## 8. Implementation in ArcGIS

For the implementation of the analytic tools (Chapter 7) into ArcGIS, a programming language is needed. I selected Python as a useful programming and scripting language for this task. Python is already included in ArcGIS, since it provides the ability of managing and manipulating spatial and attribute data. The analytic tools must first be coded as Python scripts, which can then be transformed to tools usable in ArcGIS.

### 8.1. Programming Language: Python

The open source programming language Python Version 2.7 is used to implement the developed tools in ArcGIS. Python was created by Guido van Rossum in the Netherlands in 1991. Python is considered a programming language, but is also useful for scripting. A programming language focuses on the development of sophisticated applications. The user builds new multi-functional tools. In contrast, a scripting language is based on automating functionalities, even within other programs. Already existing tools can be connected to achieve new, but related tools. Therefore, scripting yields the possibility to put existing or self programmed tools together to answer more complex research questions. Python provides both options to a certain extent [Jennings, 2011, Lawhead, 2013, Lutz et al., 2000, Zandbergen, 2013]. All codes can be changed, copied, and new codes can be distributed freely with Python. It can be also used with various platforms, such as Windows, Mac, or Linux. There is no limitation regarding hardware equipment. As Python is an interpretive language, it does not need a compiler. This means that the written code can be directly run, which makes it easier and faster to work with compared to other programming languages [Jennings, 2011, Zandbergen, 2013].

### 8.2. Python in ArcGIS

ArcGIS 10.0 supports the scripting language Python, moreover it is part of the ArcGIS installation itself. All functions and tools within ArcGIS are accessible by Python. This provides an efficient and direct method for automating tasks [Jennings, 2011, Lawhead, 2013, Zandbergen, 2013]. In general, Python scripting has become a fundamental tool for the development of automated processes in GIS. Several tools in ArcGIS are based on Python scripts, resulting in easy implementation and operation of user written scripts.

Python is accessible in several ways. The Python command line is the most basic approach for working with this programming language. A more assistive method is through Python script editors. These provide helpful tools and clearly arranged interfaces. The editors do not change the Python syntax and therefore, choosing an editor is a matter of preference. Several editors are available for Python scripting. For this work, I used the editor Integrated Development Environment (IDLE) that is automatically installed in combination with ArcGIS. IDLE is also known as the

Python shell [Jennings, 2011, Zandbergen, 2013]. Python can also be directly run within ArcGIS 10.0. When opening Python in ArcGIS a window appears that acts as an interactive interpreter for Python. The code can be integrated into this window, allowing for more efficient testing of code lines.

Python is exceptionally good for exploring spatial data [Lawhead, 2013]. This includes the research about and management of existing data within the database. Scripts can be used to analyze every feature of the list, providing fast and easy data handling. Python functions can create new columns and fields in a table. The scripts automatically fill these fields with newly acquired information, so tables within ArcGIS can be manipulated and further developed easily. It is also possible to manipulate text files with Python, allowing to output text as final result. Python is also able to obtain parameters (e.g. lengths, coordinates, and areas) of points, lines, and polygons. Geometric information is essential for the feature analysis. Furthermore, it provides input for automated measurements and calculations. Automated applications are used as scripts or tools within ArcGIS.

### 8.3. ArcGIS Tools

A developed script can be run in two different ways. Firstly, it can be run as a stand-alone script. A Python editor is required, but no ArcGIS application needs to be open at the same time. However, ArcGIS needs to be installed if the script is using a geoprocessing tool that is contained in the ArcToolbox of ArcGIS. The second option is to turn the Python script into a tool that can only be run within ArcGIS. Such a tool has the same properties as all of the tools available in the ArcGIS toolbox. Consequently, it can be used with other tools, for other scripts or within the ModelBuilder. In the following section the advantages of turning the script into a tool, instead of using a stand-alone script are presented [Zandbergen, 2013].

- A tool is shown in a tool dialog box, providing easy handling of the tools.
- The tool parameters are set and defined by a certain data type, preventing wrong input parameters and resulting errors.
- The tool can be used for other scripts.
- The tool can be easily documented for users.
- The tool is easy to share.
- The users do not need to have knowledge about the programming language Python to use the tool.

## Part III.

# Quantitative and Qualitative Analysis



## 9. Result of Case Study

This chapter gives an overview of the results of the case study (Chapter 5) that is not supported by the established tools. The chronology of both craters was detected based on crater size frequency distribution and the six different origin models (Chapter 4) were discussed to determine the origin of fracturing.

### 9.1. Chronology

A chronology plot for Crater A and Crater Lipany is obtained from the estimated surface ages (Fig. 9.1). Values including the error bars for the CSFDs do not support a distinct age determination and chronology of the surface activity. Some ages for different surface units overlap in their error bars. In those cases, CSFDs do not provide clear results. Geologic principles of superposition are used for age determination instead.

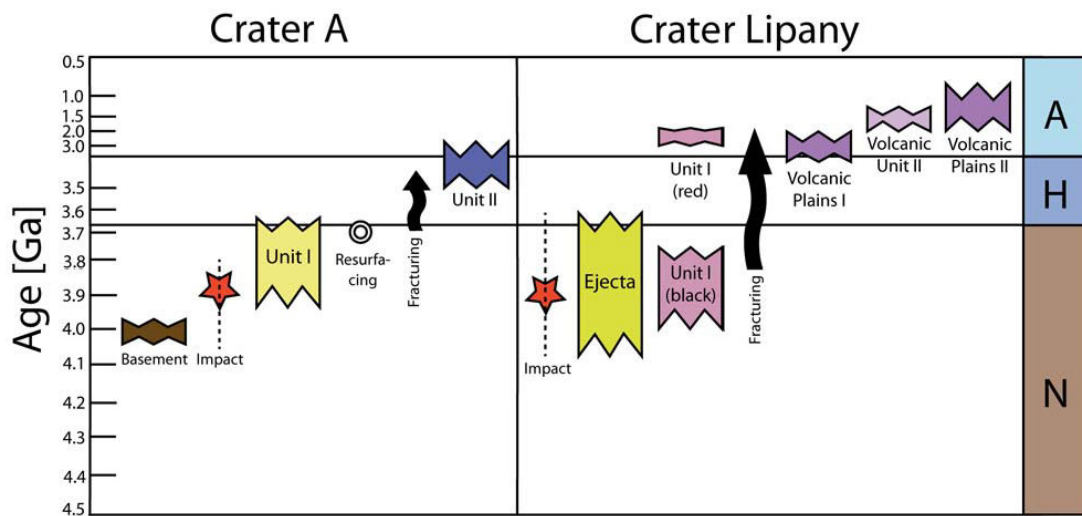


Figure 9.1.: Correlation map of surface units. Ages, including errors, of the different surfaces for both craters and the fracturing process.

#### 9.1.1. Crater A

The impact must have taken place close to the Noachian-Hesperian boundary. After the impact various materials refilled the crater. Layering indicated fluvial or eolian sedimentation and ash deposition, likely to have originated from Syrtis Major [Fassett and Head, 2007]. The upper surface units of the infilling were removed, leading to the terrain inversion and development of fretted terrain. The removal of surface material in Arabia Terra occurred at the Noachian-Hesperian boundary [Fassett and Head, 2007]. The fracturing process cannot be dated precisely, but

it must have taken place between the first (3.80 Ga) and the second (3.39 Ga) infilling. The first infilling is modified by the fractures and separated into knobs of different sizes. Subsequent and ongoing erosion softened the edges of the knobs and widened the fractures in the crater. The second infilling is deposited in the floor of the fractures and is covered by material, which appears to have been deposited there under fluvial conditions. Dust and dunes accumulated in the crater thereafter and represent the youngest surface unit.

### 9.1.2. Crater Lipany

Crater Lipany is well preserved compared to Crater A, so the surface units can be dated more precisely. Age determination of the ejecta indicates that the impact crater is of late Noachian and early Hesperian age and was filled soon after the impact, itself. Due to the overlapping error values of the BCC for the fractures and CSFD, the crater counting cannot be used for the distinct determination of the order of surface processes. However, the geologic principle of superposition suggests that fracturing happened after the first infilling of the crater, but also ended before the second infilling in the Amazonian. The fracturing process could have been continuous, only limited in time (until 1.63 Ga) by the age of the second, non-fractured infilling. Lava sheets outside the crater originating from Syrtis Major indicate that the volcano was active in the Hesperian and Amazonian.

## 9.2. Origin of Fracturing in Observed Craters

The six formation models (Chapter 4) are discussed for Crater A and Lipany based on the observed surface features. The very diverse surface features indicate different surface processes and formations.

### 9.2.1. Crater A

No evidence for volcanic activity that would support the model of intrusive volcanism is found at Crater A, although the high level of fluvial and glacial erosion might have removed potential volcanically induced structures. The center of Syrtis Major is about 1,100 km to the south (closest lava sheets about 500 km) and it is the only volcanically active region close to Crater A. The size of the magma chamber of Syrtis Major is 300x600 km [Kiefer, 2004]. Thus, the eastern part of Arabia Terra could have been influenced by subsurface heat sources. Surface features that indicate this origin model are uplift of the crater floor, “puzzle piece” fracturing, or depressions. Non of these features is observed within the crater. As a result, the model is unlikely for Crater A.

The model of tectonic systems is supported by the location of Crater A, because it is located close to the boundary and large-scale tectonic systems. Nevertheless, no tectonic fracture cuts directly through the crater. Fracturing of the crater floor can be influenced by the boundary, but no direct evidence for this is found. The crater rim is dissected by channels indicating the presence of fluvial activity. The small-scale linear features inside the crater do not have a tectonic origin, because of the absence of common orientation trends. No depressions as potential evidence for subsurface voids are present in the crater. Surface features that indicate a tectonic origin are absent.



The environment of Crater A supports all fracturing models due to water and ice related processes. An ice-rich layer is present on the surface in Arabia Terra; fretted terrain in this area supports an ice-rich and glacial environment [Fassett and Head, 2007]. Evidence for fluvial activity are found due to outflow channels ranging through the crater. Crater A is located close to the dichotomy boundary and to fretted and chaotic terrain. Volcanic and tectonic surface features are absent.

For the subsurface ice model very large crater diameters and a thickness of infilling between 3,500 and 4,000 km are required [Schumacher and Zegers, 2011]. For this FFC a total infilling of less than 3,000 m was calculated. This infilling is not thick enough to melt the deposited ice-rich material. An additional heat source is required. Heat from the Syrtis Major magma chamber could increase the subsurface temperature. However, the magma chamber of this volcano is about 800 km to the south, so the influence of this heat source is questionable [Kiefer, 2004]. The knobs of Crater A show an increase in elevation of about 400 m from the west to the east. This trend is present across the crater. The knobs, themselves, are not tilted because the observed layering is horizontal. The observations relating to knob distribution and appearance make a collapse event by a melting subsurface ice-layer possible. Nevertheless, the estimated infilling depth is too thin to melt an ice-rich layer. Therefore, the model of subsurface ice can be ruled out for this crater.

The surface features in the crater vicinity and the slope of the terrain close to the dichotomy boundary support the model of groundwater migration. The Arabia Terra region appears to be covered by highly porous and, ice-rich materials, which likely led to the terrain inversion. The channels leading into the crater in the south and west appear to be short sapping channels, which were formed by erosional retreat from the crater rim toward the surroundings. Within the crater terraces are observed, which can be developed by the presence of water. These observations support the model of seepage and piping. The entire crater is fractured, so no development of fracturing is visible. Furthermore, the knobs are not tilted. They are deposited horizontally and no pit chains are observed, although these features could be covered by the fluvial infilling. Deeper fractures than infillings are an important hint for the formation due to groundwater migration. The average fracturing depth is 322 m. The calculated maximal infilling reaches a thickness of 1,970 m. Consequently, the fractures are within the crater filling and do not serve as indicator for this origin model. No indicators for or against the groundwater migration model have been found.

Rayleigh convection is supported by the geological context and the location of Crater A. For this model, a permafrost layer is needed beneath a water-saturated sediment layer [Wenrich and Christensen, 1993, 1996]. The Arabia Terra region reveals surface features which indicate a permafrost subsurface. The impact crater itself serves as natural sink, which has been substantially modified by fluvial activity. The deposited infilling and knob material is considered to be ice-rich [Fassett and Head, 2007]. The infilling for this fracturing model needs to be between 1,100 and 1,500 m. The calculated infilling is about 300 m thicker. Regularly distributed knobs and the linear features inside the crater support this model. The observed fractures within Crater A may have developed as Rayleigh convection patterns, which have been highly modified and eroded by fluvial and eolian processes after fracturing formation.

Crater A is located close to the dichotomy boundary and in a low elevation area. This supports the model of deep-water fault systems. Furthermore, fluvial activity and channels ranging through the crater also increase the probability for this ori-

gin model. The channels in the southern crater rim are potential inflow channels, suggested by the overall slope of the area. They could have supplied the crater with water. The channels leading to the northern lowlands were possibly outflow channels. They likely formed by incising the crater rim when the water level in the crater reached a critical depth. The small amount of remaining water inside the crater drained into the subsurface or evaporated. A standing body of water with variations in water level over time can create terraces [Cabrol and Grin, 1999], which are observed on the knobs in the crater. A standing body of water with a water depth larger than 500 m is required to form deep-water polygon [Moscardelli et al., 2012]. Filling the crater up to the crater rim would result in a water depth of 645 m. In order to achieve a water depth of 500 m, the crater must have been filled to 80 % of its depth. The model of deep-water fault systems could explain the fracturing in Crater A.

For Crater A the model of intrusive volcanism and subsurface ice have been clearly excluded. No evidence for the model of tectonic systems have been found. Indicators for fracturing due to groundwater migration and against this model are found. Observed surface features inside and outside the crater support the fracturing models of Rayleigh convection and deep-water fault systems.

### 9.2.2. Crater Lipany

Crater Lipany is located close to the southern edge of Syrtis Major, which is a volcanic province of Mars. This supports the origin model of intrusive volcanism. Furthermore, no evidence for fluvial, glacial, or tectonic activity is found in the vicinity of the crater. The crater rim is not dissected, which results in a closed crater system. This closed system and also uplifted crater floor indicate an infilling process due to intrusive volcanism. The “puzzle piece” fracturing dissects the crater infilling into knobs of different size and shape. The shape of the knobs supports also a volcanic origin, because the crater interior was not modified by any fluvial processes. Volcanic pits, lava tubes, or sinkholes are visible along the fracturing system in the crater interior. These can result from the collapse of near surface materials into subsurface voids. All observed surface features in the crater vicinity and interior support the model of intrusive volcanism.

The origin model of tectonic systems for floor fracturing is not applicable for this crater. Crater Lipany is neither located close to large-scale tectonic systems, nor are any tectonic features observable around the crater. The crater rim is not dissected by any kind of channels and no evidence for fluvial activity is found. Those features would indicate a fracturing origin due to tectonic systems, but they are not present at Crater Lipany.

The environmental context of Crater Lipany does not support any model of fracturing related to ice or water activity. No glacial and fluvial features are found in the crater vicinity. Furthermore, channels do not dissect the crater rim and the crater interior does not show any evidence for water or glacial processes, either.

The model of subsurface ice would require an ice-rich infilling thicker than 3,000 m. The basaltic filling of Crater Lipany could contain some ice in the subsurface, but the total infilling of the crater is 915 m and therefore, too thin for subsurface ice melting. Thus, the model of a subsurface ice-layer is not plausible for the development of fractures at Crater Lipany.

The groundwater migration model cannot be applied to Crater Lipany, due to the absence of glacial or fluvial surface features. Pit chains are located in the fractures

of the crater, but they are most likely developed by collapse due to tectonic and volcanic activity in the subsurface [Ferrill et al., 2004]. Furthermore, the shape of the fractures is sharp and does not appear to have been modified by piping or seepage.

Rayleigh convection is not a potential fracturing process for Crater Lipany. The environment of Crater Lipany does not show glacial, fluvial, or any erosion features, which are needed for Rayleigh convection. The surface features inside the crater do not fulfill the requirements for the model either. An infilling thickness between 1,100 and 1,500 m is needed for the development of convection cells. Within Crater Lipany the infilling thickness was calculated to 915 m, which is below the required thickness. The “puzzle piece” fracturing is unlikely to be formed by convection cells, due to the sharp edges of the fractured knobs.

Fracturing due to deep-water polygons can be also excluded. A standing body of water is required for this origin model. The surface features in the crater vicinity do not show evidence for fluvial or glacial activity. The crater represents a closed system: no paleolake was ever present in the crater interior. This is supported by the absence of any erosion features and terraces inside the crater.

For Crater Lipany all glacial and fluvial fracturing models have been clearly excluded, because of the absence of water and ice related features. No indicators for the tectonic origin model were found either. The fracturing of Crater Lipany developed most likely through intrusive volcanism.



# 10. Result of Tool Analysis

In this chapter we present results of the statistical analysis obtained by the tools (Chapter 7). The results are divided into general attributes of FFCs, crater interior, crater context, and, finally, the origin types.

## 10.1. General Attributes of FFCs

Location, size, and depth are general attributes of impact craters. The statistics for these parameters of the analyzed FFCs are introduced here.

### 10.1.1. Location

In total, 433 FFCs were identified within 50°S and 45°N (Fig. 10.1). Three clusters were identified: along the dichotomy boundary, close to chaotic terrains and outflow channels, and in the Martian highlands. Within the northern lowlands, at the poles, and on volcanic regions, FFCs are absent.

The coordinates of every crater in the database is checked to determine if it is in or near a tectonic area, volcanic area, the dichotomy boundary, or chaotic and fretted terrains. 189 FFCs are located close to the dichotomy boundary region. 135 craters are close to volcanic areas, while 64 craters are found nearby chaotic and fretted terrain regions. Just 31 FFCs are located close to tectonic areas on Mars.

### 10.1.2. Size

The crater diameter distribution peaks at a diameter range between 20 and 30 km, with 100 FFCs (Fig. 10.2) in this bin. The majority of FFCs have a diameter between 10 and 50 km. The curve inclines rapidly to the maximum at 30 km and dips more slightly toward higher diameter ranges (up to 90 km). At diameter ranges between 90 and 100 km the curve rises slightly before dropping again. At larger diameter ranges there are only individual FFCs. The largest craters observed had diameters between 140 and 150 km. The average FFC size is 36 km. In relation to the diameter, the craters are divided into three types (Fig. 10.2). There are 8 simple craters with a diameter 7 km. 96 % of the FFCs are central peak complex craters and have diameters between 7 and 100 km. In total, 7 craters are multi-ringed complex craters with a diameter >100 km.

### 10.1.3. Depth

The observed crater depth is the measured depth between the crater rim and the crater floor. For all FFCs, the average is 430 m. The minimum value is 0 m and the maximum observed depth is 1900 m. The overall trend of the observed crater depth is that it increases with crater diameter, as shown by the linear curve (Fig. 10.3). The post-modification crater depth is calculated for each crater. The average calculated post-modification depth is 2,210 m, with a maximum value of 4,700 m for the largest

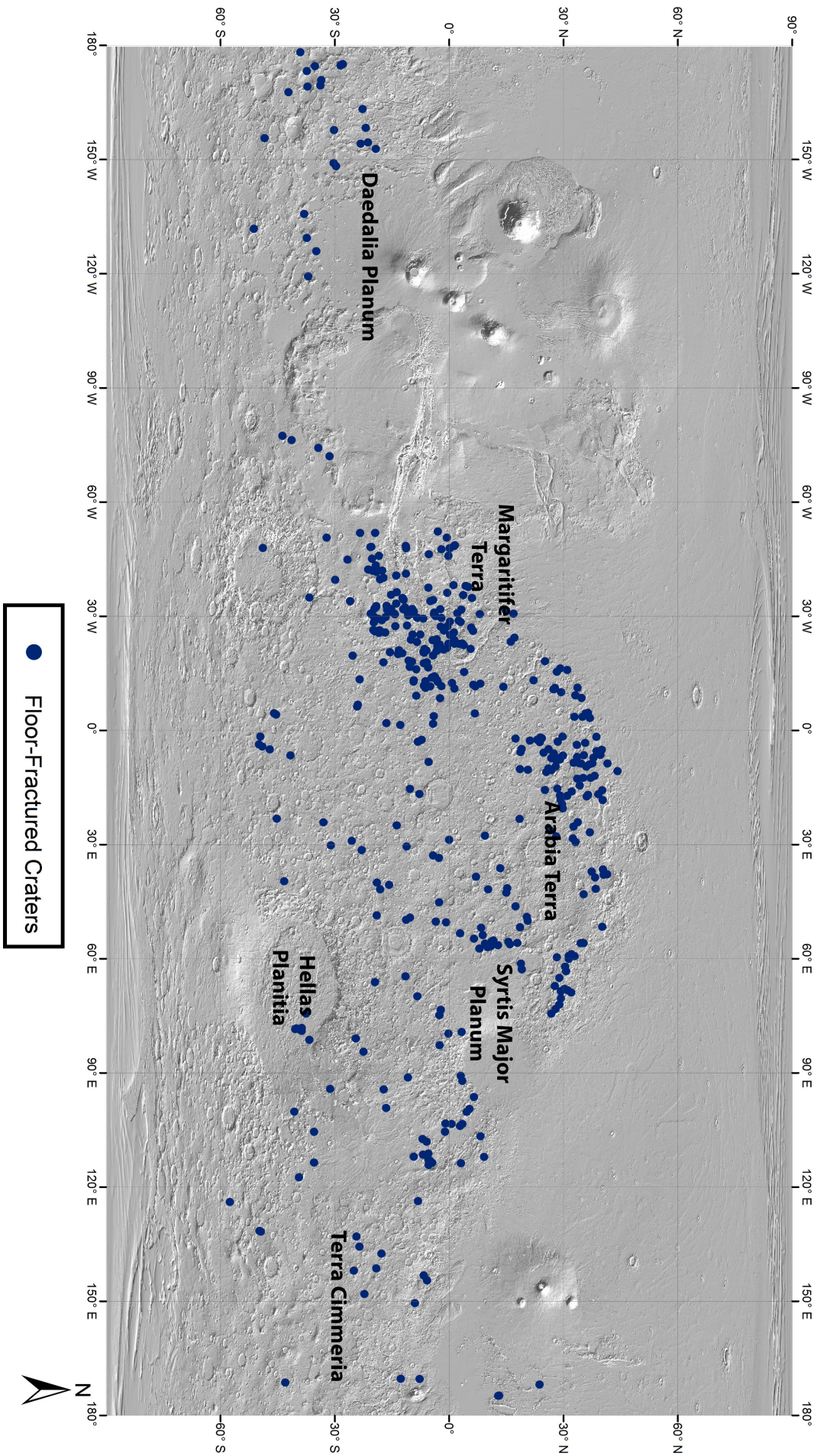


Figure 10.1.: The location of 433 FFCs and the names of the main regions with FFC occurrence are listed on a MOLA map.

Author: Marlene Bamberg

Date: 1/24/2014

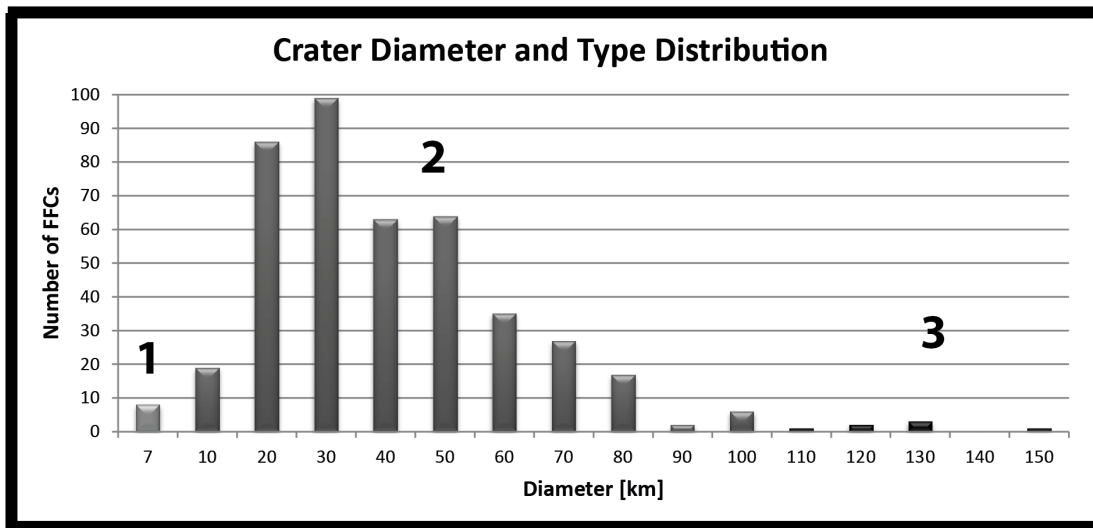


Figure 10.2.: The crater diameters are arranged into 16 bins ranging from 0 to 150 km. Based on the diameter distribution, the crater type is defined as one of three classes (1, 2, 3). The first bin represents type 1, the following 10 bins type 2 and the last 5 bins type 3. The classification scheme is explained in Chapter 7.4.

diameter (150 km) and a minimum of 740 m for crater diameters smaller than 5 km. Based on the observed crater depth and the post-modification crater depth, the thickness of infilling is calculated. The minimum infilling thickness for the FFCs is 670 m, while the maximum thickness is nearly 4,000 m. These values result in an average infilling thickness of 1,800 m. In the diagram (Fig. 10.3) the observed crater depth (dOb), the calculated post-modification crater depth (dr), and the calculated thickness of infilling (tI) are shown for all crater diameters in ascending order. The post-modification crater depth increases monotonically in relation to the diameter. The crater depth is always larger than the post-modification crater depth, whereby the depth difference of those values results in the thickness of infilling, which takes on various values for each FFC.

## 10.2. Crater Interior

The statistics presented here are based on the case study and the analysis of surface features inside the FFCs, as well as measurements and calculations for the interior of the craters.

### 10.2.1. Surface Features

The statistics for the surface features inside the crater are presented in Fig. 10.4. In 280 FFCs no depressions are observed. 150 craters show depressions within the fractures in the crater floor. The fracturing diagram (Fig. 10.4) is divided into 5 bins, representing the different types of fracturing. Fracturing along the crater rim (type 0) is observed within 29 FFCs. The minimum of the distribution is 10 craters that are fractured in one part of the crater (type I). 96 FFCs show a “puzzle piece” like crater floor (type II). A large portion of the floors is fractured in 75 craters (type III). The curve reaches its maximum in type IV fracturing. Most FFCs, nearly 50 %, show fracturing that destroys the entire crater floor. 360 craters do not have linear

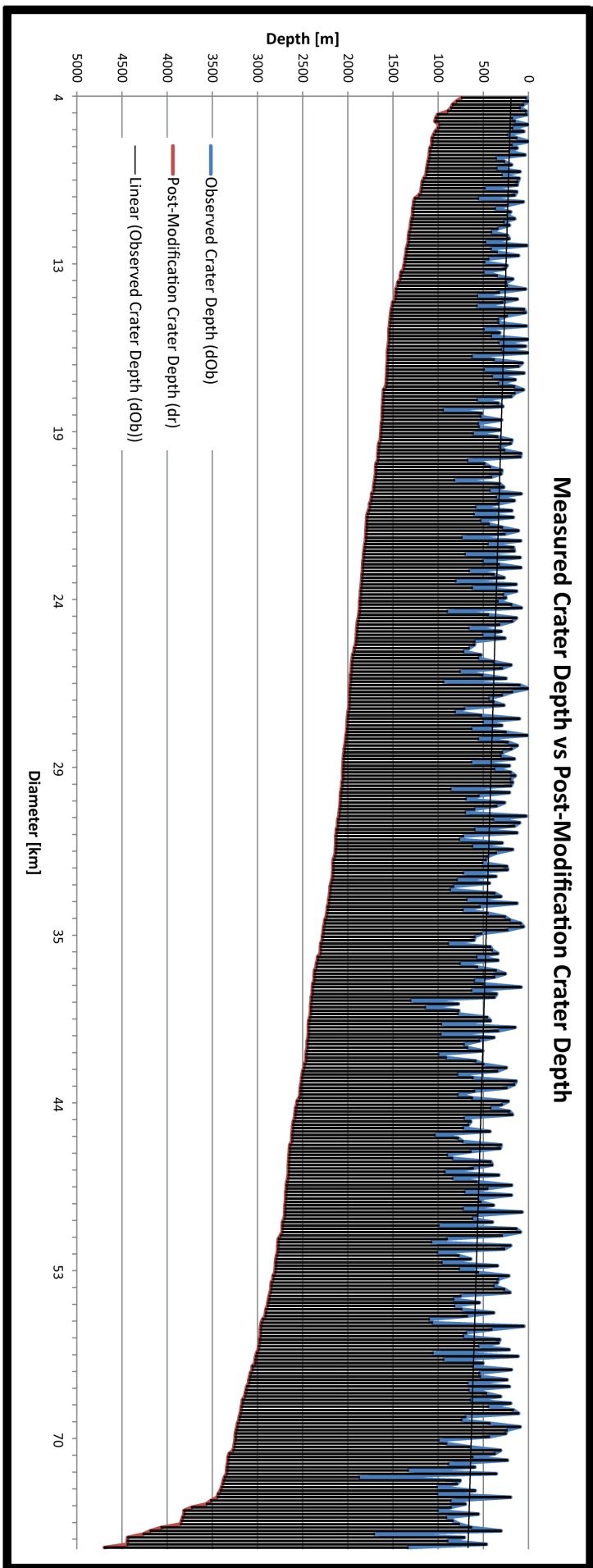


Figure 10.3.: Observed crater depth and the monotonic increase of the depth are shown in comparison to the calculated post-modification crater depth. The thickness of infilling, which is the depth difference of those values is symbolized by the black, dashed area.



features in the crater floor. These features are present in only 15 % of the FFCs. In more than 90 % craters no mesas are observable on the knobs. In 10 % of the craters, mesas are located on the knobs in the crater floor. The same probabilities are calculated for the terrace features. In 20 % of the craters, terraces are observed. In the majority of the craters, 360, the floor is not uplifted, though 70 craters have an increase in elevation within the crater.

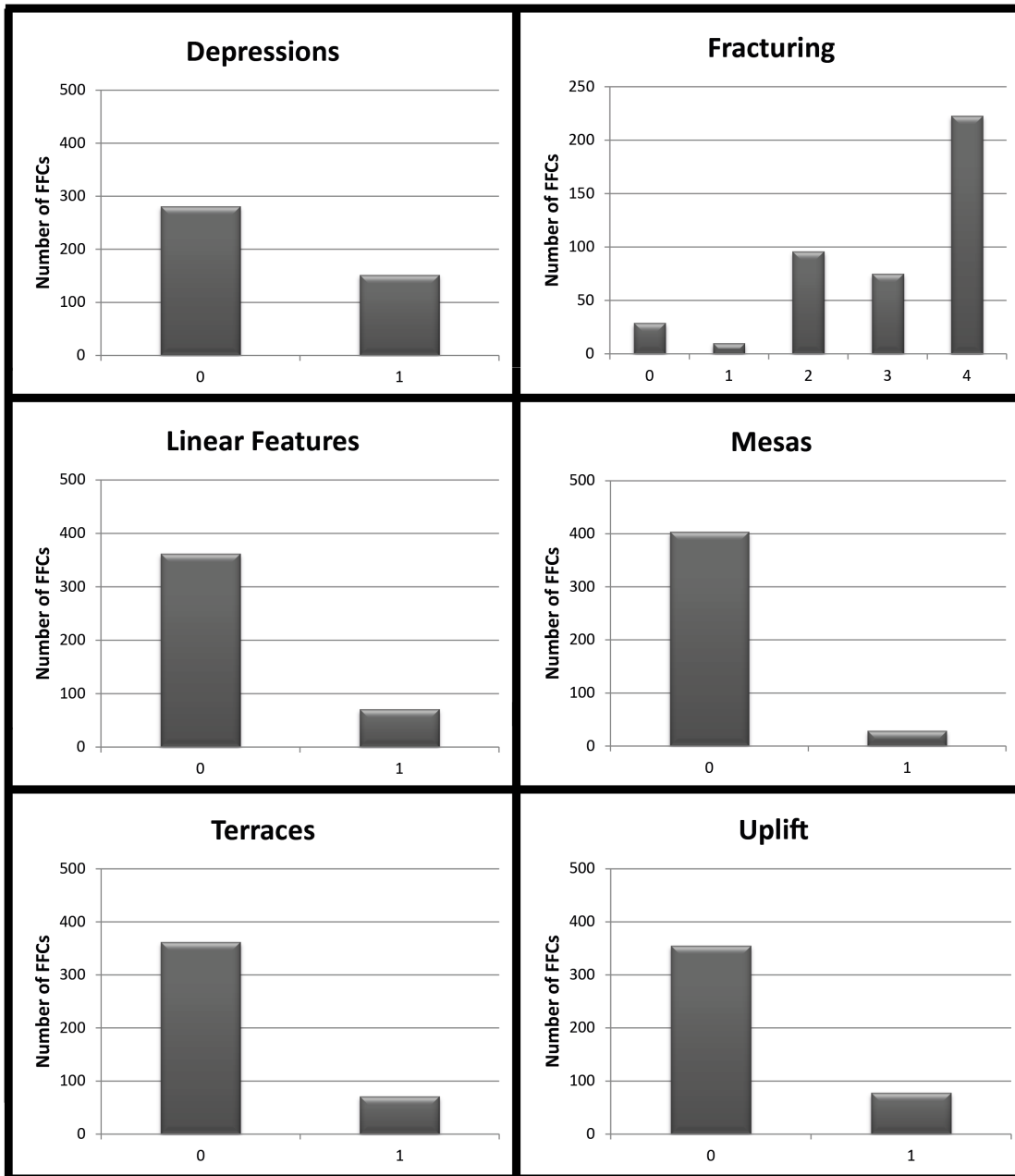


Figure 10.4.: The diagrams show depressions, linear features, mesas, terraces, and uplift in the boolean true-false principle for all FFCs. The fracturing type is divided into five different bins. The classification scheme is explained in Chapter 7.4

### 10.2.2. Elevation

For each crater in the database, different elevation values are measured (Fig.10.5). The measured elevation values for the crater rim and crater floor are printed over the

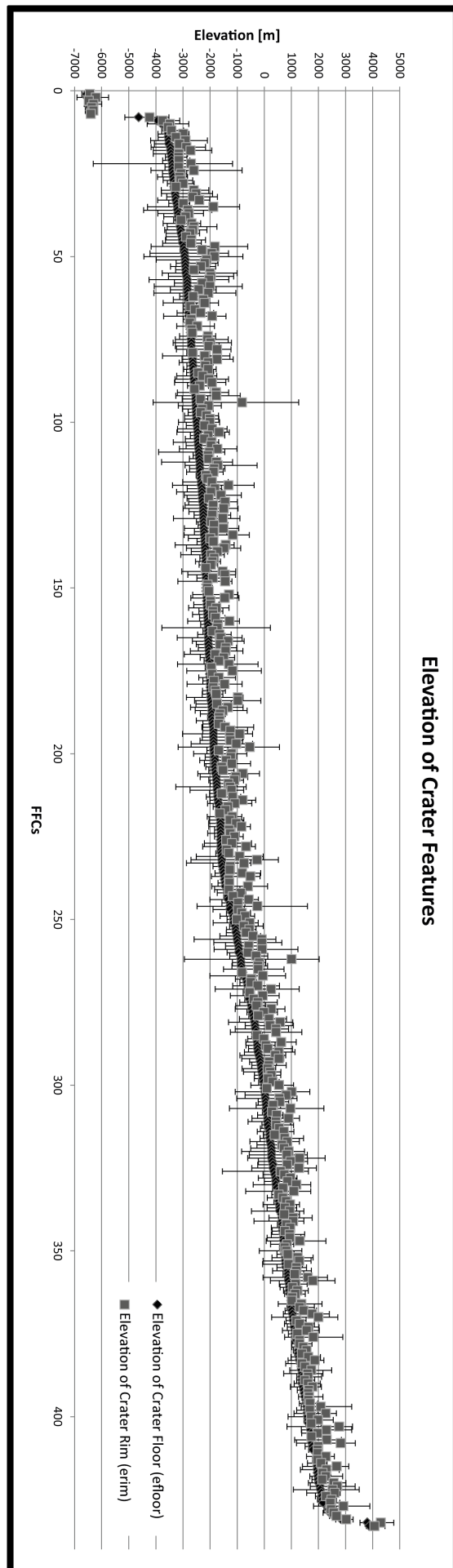


Figure 10.5.: The average crater rim elevation and the average, minimum, and maximum crater floor elevation of the FFCs.

FFCs in the plot (Fig. 10.5) in ascending order. The figure shows very few craters with an elevation between -7,000 and -6,000 m followed by a gap. The main elevation distribution then continues at -4,000 up to 3,000 m. A few individual craters are located at an elevation of 4,000 m. The elevation of the crater rim is always above the elevation of the crater floor. In addition to the crater floor elevation, the minimum and maximum elevation values of the crater floor were printed as error bars. The maximum elevation of the crater floor is often above the average rim elevation of the crater.

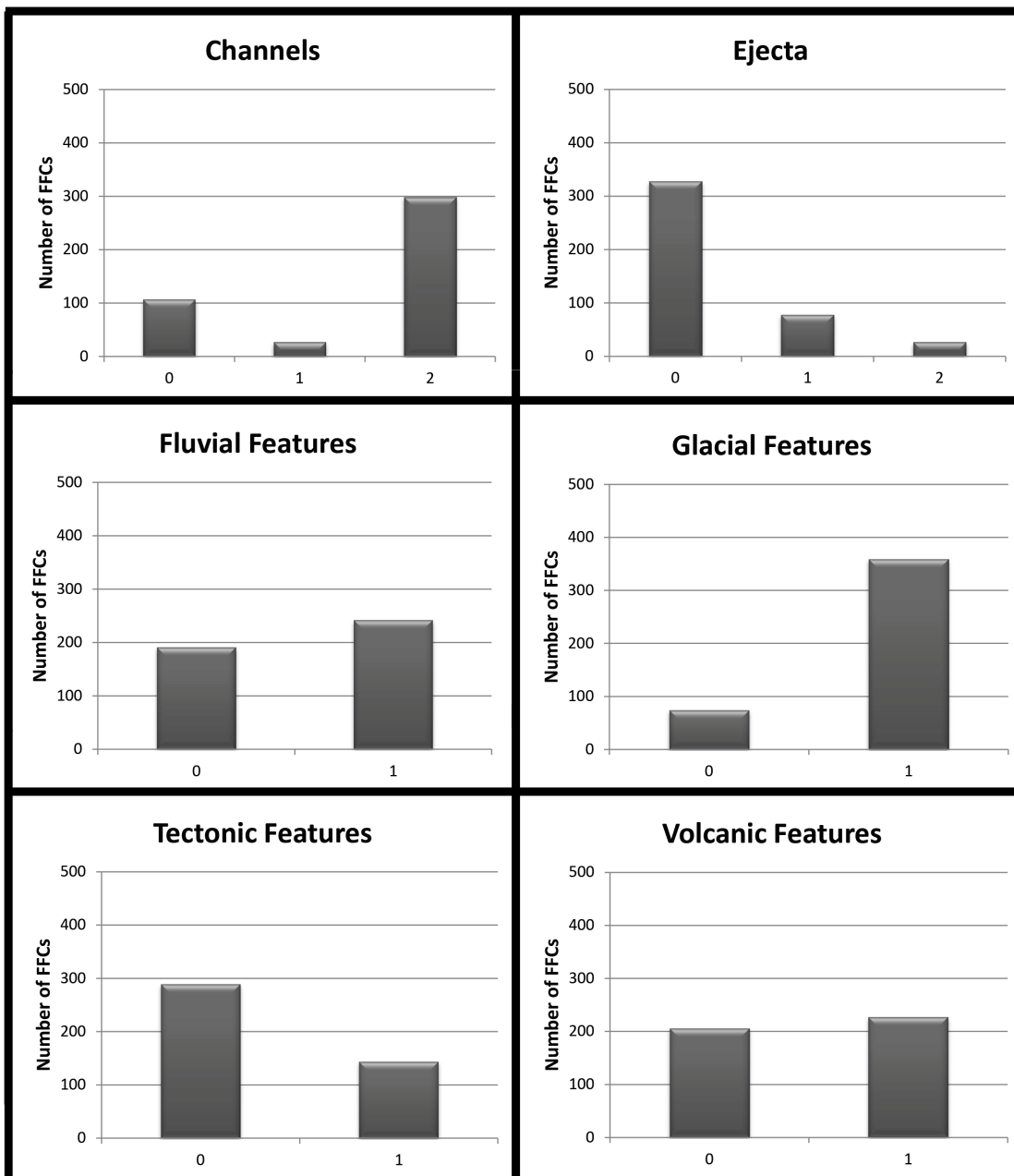


Figure 10.6.: The diagrams show channels and ejecta in three bins. The classification scheme is explained in Chapter 7.4. Fluvial, glacial, tectonic, and volcanic features are divided into categories based on the boolean true-false principle.

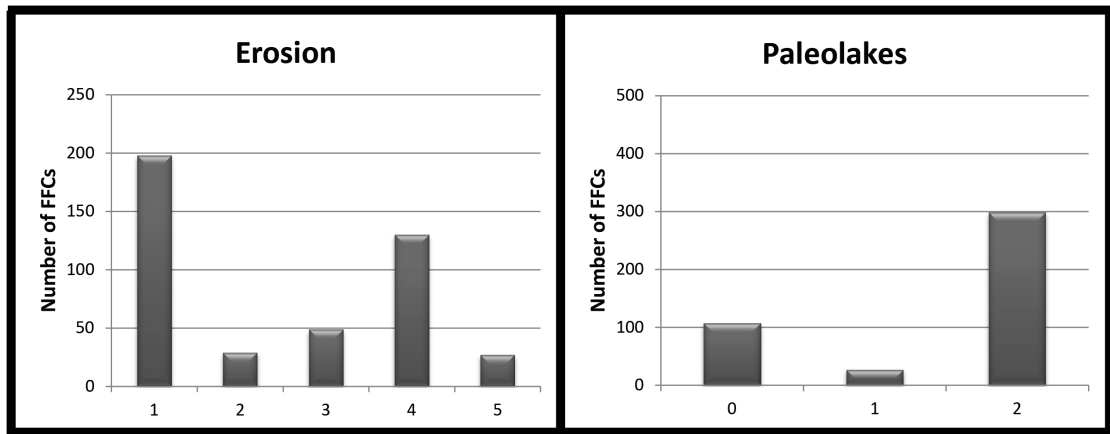


Figure 10.7.: The diagrams show erosion types divided into five bins and potential paleolakes split up into three bins. The classification scheme is explained in Chapter 7.4.

## 10.3. Crater Context

The statistics presented here are based on the case study and the analysis of surface features outside the FFCs, classifications, and neighborhood analysis regarding the environmental context of each crater.

### 10.3.1. Surface Features

The surface features outside the crater are compiled in Fig. 10.6. For more than 100 FFCs no channels intersect the crater rim or range into the crater. The rims of 30 FFCs are carved by only one channel. 70 % of the FFCs have more than one channel intersecting the rim. Ejecta blankets are not found around 75 % of the FFCs. At 20 % of the craters an ejecta blanket is clearly identifiable. For the remaining craters an ejecta blanket can neither be identified, nor completely excluded. 55 % of the craters have a surrounding area indicating the presence of fluvial features. In the surrounding area of 360 craters glacial features are found. This is about 80 % of all FFCs. Only 20 % do not have any of those features in the area surrounding the crater. At 30 % of the FFCs tectonic features are observed in close proximity to the craters. Volcanic features are found in the surrounding area at half of the observed craters.

### 10.3.2. Erosion & Paleolakes

The histogram shows the type of erosion for every FFCs (Fig. 10.7). Fluvial features and the ejecta are the key parameters for the erosion classification. The majority of craters (200) in the database are categorized as type I craters. Fluvial features are observed close to the crater and no ejecta blanket is visible. Consequently, they are considered to be strongly degraded. Type II represents slightly degraded craters with a high level of fluvial erosion, but an existent ejecta blanket. 29 craters meet this description. 49 fresh craters, without evidence for fluvial activity and an uneroded ejecta blanket, are found and defined as type III. Type IV craters have neither fluvial erosion nor an ejecta blanket. 130 FFCs of this type have been identified. At 27 craters the restraining parameters could not be identified clearly. They are considered to be type V craters, due to a lack of information or uncertainties.

The results of the paleolake tool are shown in (Fig. 10.7). The craters are classified based on the amount of channels: no, closed, and open basin lakes. 110 FFCs have no basin lakes. No channels range into these craters to support this classification. A small fraction of craters (30) are categorized as close basin lakes. 300 craters are considered to be open basin lakes.

## 10.4. Origin Types

Based on the observations of surface features inside and outside each FFC and the results of the already presented measurements, calculations, and classifications, the final results of the six origin types are described.

### 10.4.1. Result of the Six Origin Types

The histograms (Fig. 10.8) are based on measurements, calculations, and classifications described in Chapter 7.4. The histograms show the probability in percentage of six different origins for 433 FFCs. In this research the probability describes the number of key parameters met for each origin type. The probability of each origin type is divided into eleven bins, starting at 0 % and ending at a probability of 100 %. This also represents the number of key parameters met for the origin. The tectonic origin is divided into eight bins. Every crater has the possibility of parameters that conform to the key parameters of the origin types and therefore, the probability to be formed by each origin model. This also means that the origin models and the according key parameters are not mutually exclusive.

#### Deep-Water Fault Systems

The histogram of the deep-water fault system origin (Fig. 10.8 A) shows a nearly symmetrical distribution with a distinct peak in the middle of the curve at 50 %. The curve is steeper to the right than to the left. Just one FFC is found with a 0 % probability for this origin type. The curve increases steadily to 80 FFCs at 40 % until it hits the maximum of 140 FFCs with 50 % probability. After that, the curve decreases again to 50 FFCs with 60 % and then decreases further. 15 craters are identified that have a probability of 80 % for this origin. 3 FFCs have a probability of 90 % or more for the deep-water fault system origin.

#### Rayleigh Convection

The probability distribution of the Rayleigh convection origin is symmetrical (Fig. 10.8 B). No FFCs have a probability below 20 % of being formed by Rayleigh convection. The distribution increases toward the mean value and peaks at 50 % with 90 craters. After this peak the curve decreases. 9 FFCs have a probability of 90 % to be formed by this origin type and 2 craters show a 100 % probability.

#### Subsurface Ice

The histogram (Fig. 10.8 C) for the subsurface ice origin is nearly symmetric, peaking at 50 % probability. No FFCs have less than 20 % probability for this origin type. The distribution starts with 4 craters at 20 % probability, 16 craters at 30 % probability, and then increases to the peak value with nearly 200 FFCs at 50 %.

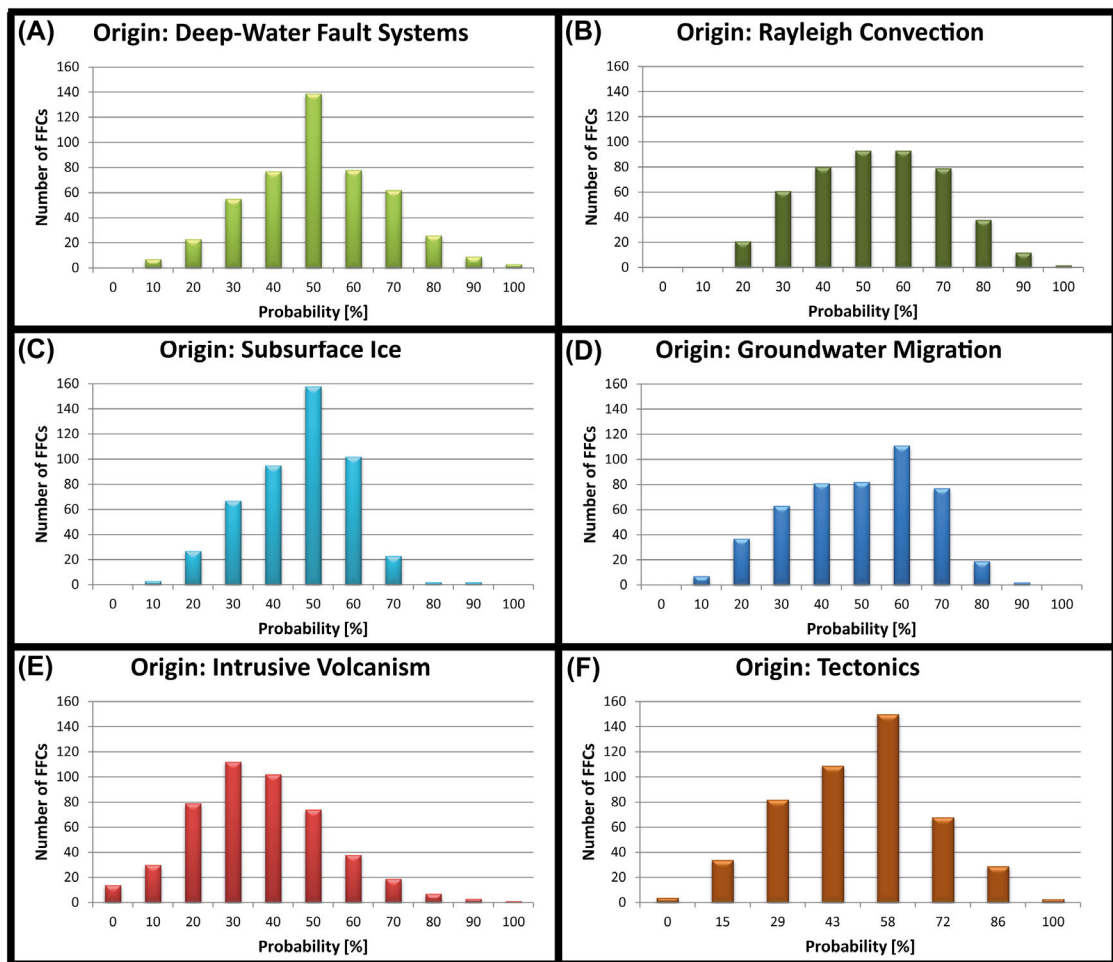


Figure 10.8.: All histograms are based on the origin tools described in Chapter 7.4.

After that peak the distribution decreases and flattens to 100 craters at 60 % probability and 50 craters with 70 %. There are 12 craters in total with a probability for this origin type larger than 70 %.

### Groundwater Migration

The histogram (Fig. 10.8 D) is skewed to the left, but no clear peak is present. There are no FFCs that have a 0 % probability of the groundwater origin. 5 FFCs have a 10 % probability to be formed by this model. The distribution of craters with this origin increases up to 50 %. Between 50 and 70 % the curve reaches its maximum with 80 craters each. After this, the number of craters decreases with increasing probability of the groundwater migration origin. 29 FFCs have an 80 % probability of being formed by groundwater migration. There are only 2 craters that have a 90 % probability for this origin model.

### Intrusive Volcanism

The probability of the intrusive volcanism origin is presented in this histogram (Fig. 10.8 E). The curve is skewed to the right, with a maximum peak shifted to the right of the mean value. Several craters do not support the intrusive volcanism model, whereas just a few craters are found that have likely been formed by this process. 14 FFCs show no parameters that would support this type of origin. The

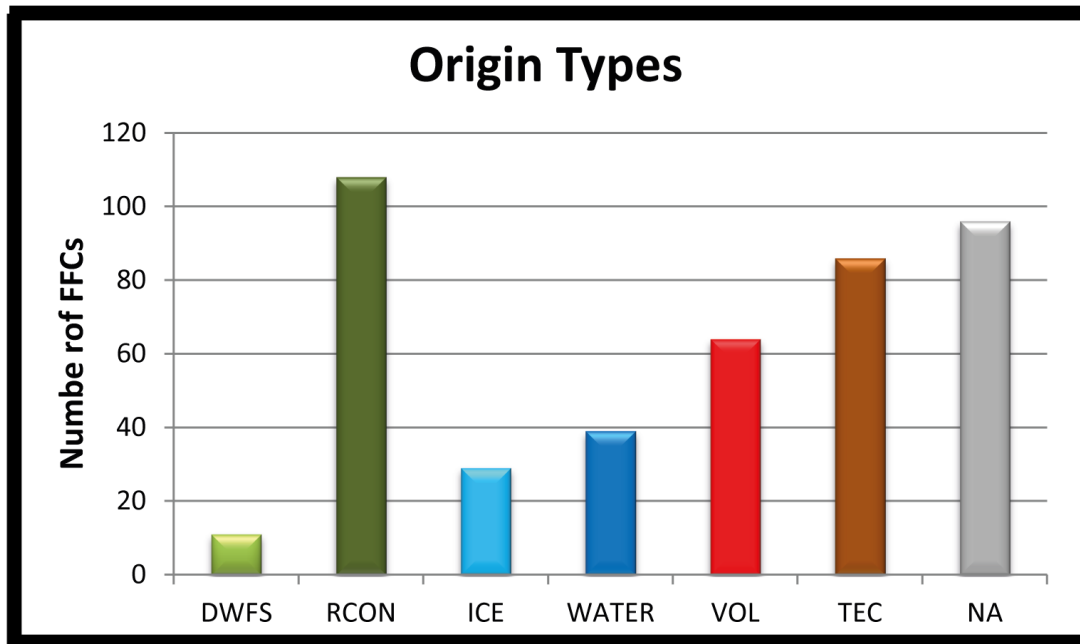


Figure 10.9.: FFCs that have a maximum probability, based on the developed tools, for any origin type  $\leq 50\%$  are not classifiable (NA) with the used tools. The other FFCs are split up into the six origin types. The origin types are abbreviated by the database name. The scheme is explained in Chapter 7.4.

probability is therefore, 0 %. The curve increases quickly to peak first at 30 % and again at 50 % probability for the intrusive volcanism origin with 80 and 100 craters, respectively. The curve decreases after 50 %. There are 15 craters, in total that support this model with a probability higher than 80 %. 4 FFCs fulfill all parameters, resulting in a 100 % probability for the origin of intrusive volcanism.

### Tectonics

The histogram for the tectonic origin (Fig. 10.8 F) is slightly left skewed and peaks at 58 % probability. 10 FFCs have a probability of 0 %. The distribution increases to 130 craters at 58 %. The curve decreases after the peak to 49 craters at 72 %. 27 craters have a probability of 86 % and 2 craters have a 100 % probability to have a tectonic fracturing origin.

### 10.4.2. Most Likely Origin for each FFC

The fracturing origin for each crater is defined by the origin type with the most matching key parameters based on the developed tools (Fig. 10.9). This histogram of the six color-coded origin types shows how many craters each origin type supports. The crater is considered to be not classifiable if  $\leq 50\%$  of the key parameters are met (the probability is  $\leq 50\%$ ). These craters are marked as “NA”. An origin type was not clearly identified for 96 craters. 108 FFCs have Rayleigh convection as the most probable origin model. The origin of deep-water fault systems is the least probable with 11 craters. 29 craters support an origin due to subsurface ice. 39 craters are formed by groundwater migration. 64 craters have most likely developed through intrusive volcanism. Tectonic systems are the origin model for 86 FFCs.

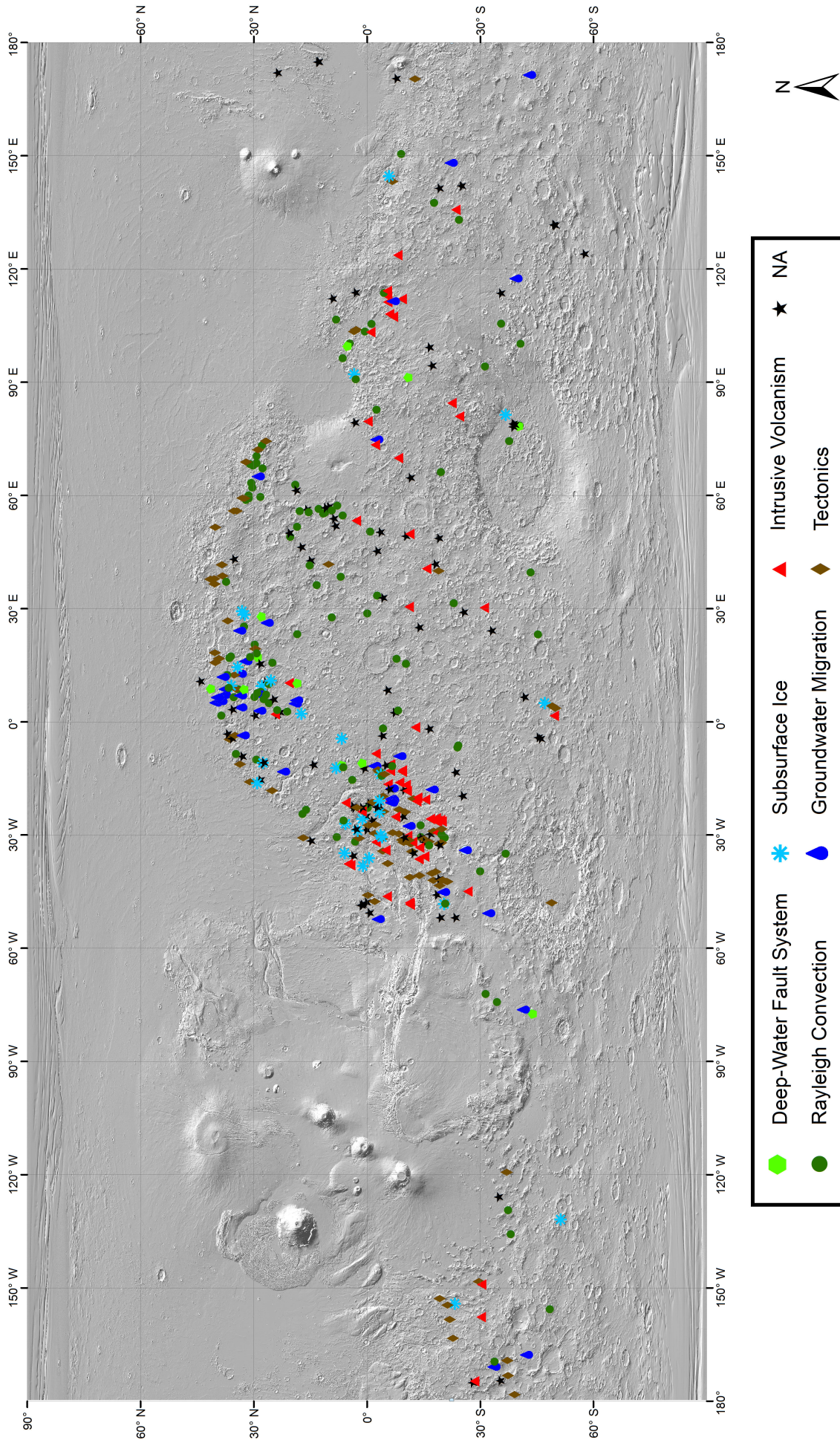
The most probable formation process for each FFC is also shown in a spatial

distribution map (Fig. 10.10). The FFCs developed by Rayleigh convection are not limited to specific regions on Mars. They appear close to the boundary, surrounding volcanic regions, the Hellas basin, and also the southern highlands. The only location where they seem not to be the dominant fracturing origin is close to the outflow channels and chaotic terrains of Valles Marineris. Several deep-water fault systems are found close to the dichotomy boundary in the western Arabia Terra region. 4 FFCs with that origin type are located in the southern highlands, up to a latitude of 40°S. Fracturing due to subsurface ice occurs at the outflow channels and chaotic terrains originating in Valles Marineris and in the Arabia Terra region. Most FFCs with this origin type are in the immediate vicinity of the dichotomy boundary. 4 FFCs with this origin type are found in the Martian highlands. FFCs due to groundwater migration are mainly located in the Arabia Terra region and in the south of the chaotic terrains. Individual craters are found in Terra Sirenum at 35°S and 170°W, and in the vicinity of volcanic regions within the highlands. FFCs influenced by intrusive volcanism are found mainly in the southern highlands, around the volcanic regions, and in a certain distance of the chaotic terrains at 15°S and 25°W. The tectonic systems origin model dominates along the dichotomy boundary, the chaotic terrains, and in the west of Daedalia Planum at 20°S and 160°W. Craters that are not classifiable are found in the highlands and the boundary regions and they are distributed over the entire planet. All craters within the Martian lowlands show no distinct fracturing origin.

### 10.4.3. Origin Types in Detail

The probability values for the different origin types are averaged for all craters of one origin (Fig. 10.11). On the horizontal axis the averaged values of all craters classified as the same origin are listed. The probability for the origin types is printed on the vertical axis. The origin is defined by the maximum value of probability. Within this diagram the overall and typical probability distribution for six origins is highlighted. 11 craters are classified as deep-water fault systems (Fig. 10.9). The averaged probabilities of the different origin types for those craters are shown. The maximum value is averaged to 70 %. The models of Rayleigh convection, subsurface ice, groundwater migration, and tectonics achieve probabilities between 50 and 65 %. The probability difference between these origins is small. In contrast, the probability of intrusive volcanism is 25 %. The distributions for FFCs originating through Rayleigh convection, subsurface ice, and groundwater migration are similar to the deep-water fault systems origin. Again, the peaks of each origin are shown at 65 % and the remaining origin models achieve probabilities of 50 % and are consequently, closely located to the maximum value. The only origin type with different probability values is intrusive volcanism, which is below 35 %. 64 craters are classified as having a fracturing origin due to intrusive volcanism (Fig. 10.9). The averaged probabilities peak for the intrusive volcanism model above 65 %. All other origin models have a probability around 30 %. The average probabilities of 86 craters formed by tectonics peak at 70 %. The other origin models differ between 40 and 50 % probability, and the model of intrusive volcanism reaches only 20 %. The overall distribution of probabilities for the tectonic origin is similar to the intrusive volcanism diagram. The 96 craters that could not be assigned any origin type have average probabilities between 30 and 40 % for each origin model.





Author: Marlene Bamberg Date: 1/24/2014

Figure 10.10.: The most probable origin type for each crater is symbolized and color-coded on this MOLA map.

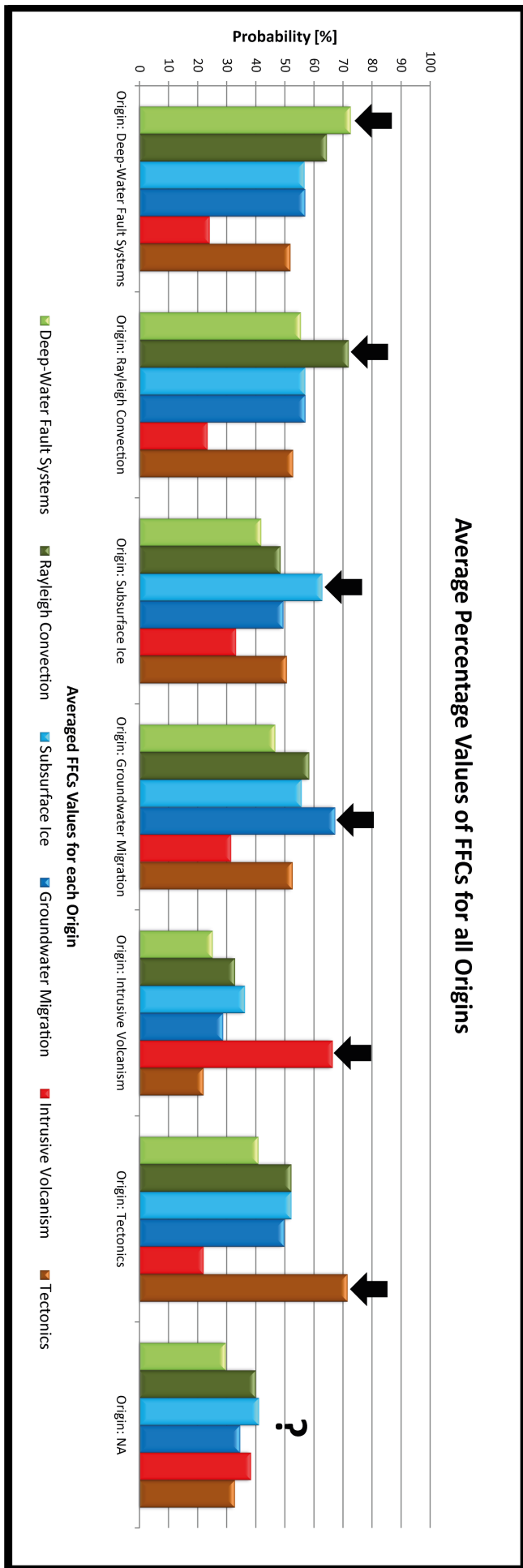


Figure 10.11.: For all FCCs of one origin the probabilities of the color-coded origin models are listed.

#### 10.4.4. Case Study Craters

Crater A and Crater Lipany of the case study are also included in the global FFC database. The probabilities for each fracturing model based on the automated tools are presented for the two craters (Fig. 10.12).

Crater A does not show a clear fracturing origin. The most probable model is Rayleigh convection with 90 %. Deep-water fault systems also have a probability of 75 %. The models of subsurface ice, groundwater migration, and tectonic obtained a probability higher than 55 %. The only model that can be clearly excluded is intrusive volcanism. In the database the fracturing for this crater is classified as Rayleigh convection.

The values of Crater Lipany clearly peak at the intrusive volcanism model for 100 %. All other origins show a probability less than 30 %. In the database the crater is classified as being influenced by intrusive volcanism.

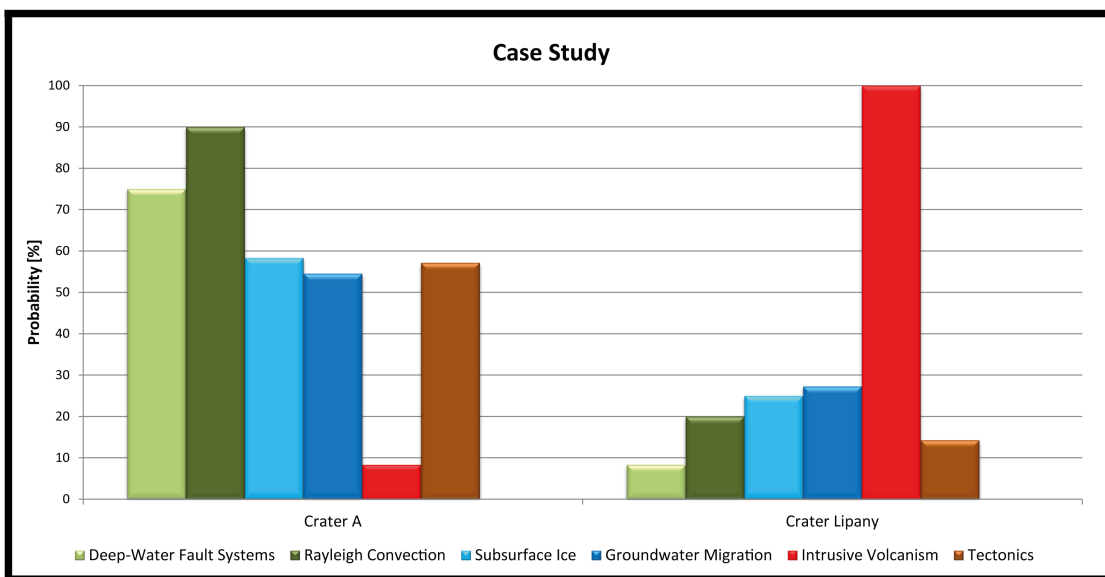


Figure 10.12.: The probabilities of the six origin models are presented for the case study of Crater A and Lipany.



# 11. Discussion

In this chapter the results (Chapter 9 & 10) are discussed and compared to each other. Based on the comparison, advantages but also disadvantages and limits of the automated analysis tools are identified.

## 11.1. Interpretation of Tool Analysis Results

433 FFCs are found mainly along the dichotomy boundary (especially Arabia Terra), the outflow channels, and the Martian highlands (Fig. 10.1). No craters are identified in the Martian lowlands, due to the deposition of young, eroded, and transported surface material. Ancient morphologies are covered in that region and little surface features, in general, are identified in the lowlands. The same process of superposition occurs close to the volcanic regions on Mars. Younger materials, like lava flows, cover ancient surface morphologies. Ice caps at the poles ensure covering of crater morphologies and a high level of erosion makes a distinct identification of surface features nearly impossible.

The crater diameter distribution shows that mainly central peak complex craters with a diameter between 7 and 100 km are floor fractured. Individual craters with a diameter below 7 and above 100 km are also found, but are the exception (Fig. 10.2).

All FFCs are infilled by 1,800 m of material on average (Fig. 10.3). The infilling is essential for the fracturing process. It is either needed to form the fracturing patterns (fine grained sediment layer for convection cells) or it is deposited in the crater as a result of the fracturing process (volcanic materials originating from the subsurface). There are no FFCs with an infilling thickness below 670 m.

Results were obtained for all 433 FFCs on Mars. To classify these FFCs depending on their fracturing origin, defined geologic processes are needed for the semi-automated classification tools. The classification method becomes more reliable with more precise definitions of geologic processes and identification of geomorphological features. This is because the classification tools conduct their analysis based on key parameters, which are defined in Chapter 7. The classification result increases in quality and reliability with more parameters available for one origin type and more specificity in those parameters. The key parameters are based on previous research on FFC formation and the case study included in Chapter 9.

### Intrusive Volcanism Origin

The statistical analysis revealed 64 craters, resulting in 15 % of the FFCs (Fig. 10.9) to be formed by intrusive volcanism with a probability of 65 % in average (Fig. 10.11). All other origin models for the classified craters have a considerable lower probability and are consequently unlikely (Fig. 10.11). The result of this classification is reliable, due to the distinct difference in probability compared to all other origin models. Furthermore, 15 FFCs are found, which support this model with a high probability above 80 % (Fig. 10.8).

The intrusive volcanism model was discussed various times for FFCs on the Moon [Brennan, 1975, Jozwiak et al., 2012, Schultz, 1976, Wichman and Schultz, 1996]. Consequently it is the most analyzed and discussed model for FFC formation. Due to that research several key parameters can be retrieved and adapted to Martian FFCs for the developed classification tool.

The intrusive volcanism model is linked to volcanic areas on Mars. We took recent volcanic areas and also ancient volcanoes into account. 30 % of all FFCs are located close or within volcanic regions. Considerable parts of the Martian surface are covered by volcanic materials, the abundance of basaltic materials, as recorded by the TES instrument, illustrates that assumption (Fig. 6.4). The vicinity of the FFCs reveals important information for the type of origin.

At most FFCs (230) volcanic features have been observed, they support the volcanic origin model. For the clear identification of the origin type no influence of water and ice, resulting in erosion should be present. No fluvial features can be found at 200 FFCs, however, glacial features are present at 80 % of the FFCs (Fig. 10.6). Consequently, the amount of FFCs that do not show any erosion is small (50) (Fig. 10.7). Erosion is not a criterion that eliminates this model, but missing erosion makes it easier to identify the surface morphology and to exclude an origin due to ice or water related processes. It is difficult to analyze, if ice and water related processes are responsible for fracturing, or just occurred after the fracturing. Excluding those environments makes the classification more reliable. To also confirm the presence of processes originating from the subsurface, a closed crater system and no channels intersecting the crater rim are essential for the model. At 110 FFCs channels do not intersect the crater rim. This also excludes tectonic systems, destroying the crater rim (Fig. 10.6). Based on the crater context roughly 100 craters would have a fitting environment for this origin type. The crater context is essential for the identification of prevailing processes, but the crater interior shows which processes were dominant on the crater floor.

For this origin model the “puzzle piece” fracturing is an essential key parameter. This type of fracturing is easy to identify and occurs in 100 craters. Another important parameter is the uplift of the crater floor. It is difficult to identify, but the presence of an uplifted crater floor supports only this origin type. Crater floor uplift has been determined for 80 FFCs. The last parameter supporting this origin type is the presence of depression features, which are potential collapse structures. They develop through subsurface voids and are expected to be observed when subsurface movement due to intrusive processes is present. One third of the craters show depression features within the fracturing in the crater floor (Fig. 10.4).

The information of environmental context and crater interior analysis are merged together to classify craters most probable for an intrusive volcanism origin. The distribution of FFCs is shown in Fig. 10.10. Like previous research already indicated, FFC developed by this origin were expected close to volcanic regions. The distribution map supports this assumption. The majority of FFCs can be found in vicinity to volcanic regions, mainly Daedalia Planum, Syria Planum, Syrtis Major, and Hesperia Planum. They are not located on the volcanic plains. The surface age of the volcanic plains is relatively young, consequently deposited and erupted materials superpose impact craters. Nearly all craters are located within the southern highlands. Just two individual craters are found in the Arabia Terra region far from any known Martian volcano. Both craters have a probability for this origin of less than 60 %. Those craters could have been formed by intrusive volcanism, without a visible volcanic region at the surface. Magma chambers could have been present

in the subsurface at the time of fracturing formation. Without a valve to erupt the magma at the surface, no clear evidence would be present in the region. Additionally, Arabia Terra is a region of high fluvial and glacial activity. This indicated that several processes and surface features are found in that region. Superposition and erosion make it difficult to identify surface features and to distinguish between processes involved at the fracturing formation or at the modification of the crater structures afterwards. The high amount of erosion is the reason for the relatively low origin probability.

With this classification tool FFCs with an origin through intrusive volcanism can be found on Mars.

## Tectonic Origin

20 % (86) of the FFCs show an origin related to tectonic systems (Fig. 10.9). The averaged probability for this origin type is higher than 70 %. Similar to the volcanism model, the result of this classification is precise, because of the significant difference of 20 % probability to all other origin types (Fig. 10.11). 30 FFCs have a probability above 85 % to be formed by this origin model (Fig. 10.8).

The model of tectonic activity explaining floor fracturing was discussed by Hanna and Phillips [2006], Smrekar et al. [2004]. This model is defined by the crater context and location. Consequently, most key parameters are not related to the crater floor, but to the environment the crater is located in. As a result, this origin model has the least number of key parameters.

FFCs are checked whether they are located close to tectonic regions. These regions are defined by grabens and large scale fracturing systems. They are found along the dichotomy boundary, surrounding the Tharsis volcano and Valles Marineris, and in the southern highlands of Mars (Fig. 6.3). The amount of tectonic features and therefore, detail of the tectonic map, are relevant to identify this origin type. Based on the map used, we found just 31 FFCs in the vicinity of tectonic systems. This number is relatively low, but only the largest tectonic features on Mars were mapped.

Tectonic features must be observed in the crater surrounding for this origin model. These features represent not the large-scale fracturing systems that are analyzed in the tectonic map, but rather smaller tectonic features such as wrinkle ridges or faults that are observable on a smaller scale. At 35 % (150) of the FFCs, tectonic features are observed. To distinguish between tectonically and volcanically influenced fracturing, volcanic features should be absent in the crater vicinity. Volcanic features are observed in 50 % of the FFCs, leaving several craters without these types of features. Fracturing due to tectonic activity is often linked to fluvial activity in the region, because ice or subsurface water will be pressurized and pushed to the surface and creates outflow. 60 % of the craters show fluvial activity in the surrounding area. The presence of channels intersecting the crater rim supports the fluvial and, also, the tectonic activity. At 75 % of the craters one or more channels are observed (Fig. 10.6). All the context information leaves 150 FFCs with a potential origin due to tectonic systems.

Only two parameters are important for tectonic fracturing formation. Material falling into subsurface voids is evidence for potential subsurface movements. Thus, depressions should be present on the crater floor. At 35 % of the FFCs depressions are present within the fractures. The fracturing itself can be indicative of tectonics and is developed in several ways. The only fracturing type that would be not supported by this model is the “puzzle piece” fracturing. All other fracturing types,

starting in a certain part of the crater, along the rim, or being present on the entire crater floor could be induced by tectonic activity and fluvial erosion afterwards (Fig. 10.4). 330 craters show the supported fracturing type.

Combining the key parameters of the crater context and crater interior suggests 150 FFCs potentially formed by tectonic activity. The limiting parameter is the location of the crater, itself. This dependency is shown in the origin type distribution map (Fig. 10.10). Many FFCs with a tectonic origin are found along the dichotomy boundary, because several graben systems are located there. Another “hot-spot” for tectonic FFCs is around the outflow channels and chaotic terrains originating from Valles Marineris. FFCs within the highlands and close to large scale tectonic systems also have a high probability of tectonic origin, as expected. These regions are at 40°S and 160°E, as well as 50°S and 5°E.

The spatial results fit the expectations of the distribution for this origin type well. This is surprising, because only six key parameters for the crater context and crater interior were used. Consequently, 150 craters fulfilled the key parameters; adding the spatial parameter helped to obtain a more accurate and reliable result.

### Water and Ice Related Origins

The four remaining origin types are all related to fluvial and glacial environments and processes. The majority of FFCs (108) seem to have an origin type related to Rayleigh convection. Deep-water fault systems are the origin model with the least amount of FFCs (11). 29 craters were developed by the subsurface ice model and 39 FFCs have a fracturing origin due to groundwater migration (Fig. 10.9). Based on this diagram the most probable origin for the fractures, in general, is Rayleigh convection. Nearly 25 % of FFCs have this fracturing origin, which is surprising. We see that the probabilities for various origins are not as drastic as they seem, if we take the average percentage values for all origin types for the glacial and fluvial models into account (Fig. 10.11). The diagram illustrates that the probabilities of all fracturing processes range between 50 and 70 %. This means that an origin type cannot be identified with a high reliability. The only origin process that can be clearly excluded is intrusive volcanism. This is true for the deep-water fault system origin, Rayleigh convection, subsurface ice, and groundwater migration. The required key parameters for these origin types are all related to fluvial or glacial morphologies. These morphologies are linked to each other, representing different stages of aggregation and, therefore, showing interdependency. Based on this assumption, we would expect a more equal distribution of FFCs for the four origin processes. The peak for the Rayleigh convection model is not obvious; the key parameters need to be analyzed for each origin model to understand the distribution and probabilities.

Rayleigh convection is the most likely origin model for 25 % of the FFCs (Fig. 10.9). The probability distribution for this origin process is a smooth curve with a relatively high number of FFCs with a probability higher than 80 % (Fig. 10.8).

This model is associated with polygonal fracturing patterns within the crater floors that are usually much smaller than the observed fractures in the FFCs [Cooke et al., 2011, Gasselt, 2007, Hiesinger and Head, 2000, Lane and Christensen, 2000, Luchitta, 1983, Wenrich and Christensen, 1996]. To take this origin model into account, I suggested a widening of developed fracturing patterns by erosional processes.

Rayleigh convection is not constricted to particular regions on Mars; the model is just limited to  $\pm 40^\circ$  latitude. This does not represent a limitation for the observed



FFCs, since more than 90 % of them are located in this latitude range (Fig. 10.1).

The six context parameters for this origin type are all related to the absence of volcanic and tectonic features and the presence of fluvial and glacial features, erosion, and open or closed basin lakes. On average, more than 250 craters fulfill these parameters (Fig. 10.6& 10.7). The context parameters do not reduce the amount of FFCs for this origin type, either.

Three parameters are analyzed for the crater interior. A very important parameter is the infilling, since this origin model requires a certain thickness of infilling for the development of fractures. The deposited materials inside the crater should be between 1,100 and 1,500 m in thickness. This range is close to the average thickness of 1,800 m for all FFCs. Consequently, nearly 100 FFCs are within the required thickness range (Fig. 10.3). Linear features and fractures covering most of the crater floor support this origin model as well (Fig. 10.4). They are the most restricting parameters, as only 90 craters are observed with linear features and 75 with this type of fracturing.

The combined context and interior information are used to obtain those FFCs with an origin of Rayleigh convection. The boundary conditions for this origin type are very broad. Many craters fit the key parameters, so the amount of FFCs with this origin type is high. This is displayed in the global distribution (Fig. 10.10). Craters developed by Rayleigh convection are consistent over the Martian surface. They are located along the boundary, but also in the highlands. The only region where Rayleigh convection is not the dominant origin of FFCs is the chaotic terrain.

In opposite to the Rayleigh convection origin the model of deep-water fault systems is probable for the least amount of craters. Just 11 FFCs are classified by the tool to be formed by this process (Fig. 10.9). At most FFCs half or less of the required key parameters are available (Fig. 10.9). That means the key parameters are narrow, resulting in a small amount of FFCs matching the restrictions.

Deep-water fault systems is a model described by Moscardelli et al. [2012] for developing large size polygons on Mars. This model does not contain spatial key parameters, because the origin due to deep-water fault system is not limited to specific regions on Mars.

Fluvial and glacial features should be observed in the crater vicinity (Fig. 10.6), this is the case for most FFCs (220 & 360). Tectonic and volcanic features should be absent, which is also the case for several FFCs (300 & 200). A high level of erosion is needed to increase the fracturing size. 200 strongly degraded craters are classified. The crater rim should be dissected by one channel to form a potential paleolake. This would support the presence of a standing body of water, which is important for the development of polygonal patterns by deep-water fault systems. This key parameter narrows the amount of potential FFCs with this origin model down. Just 20 FFCs show potential for a standing body of water in form of a closed basin lake (Fig. 10.7).

Additionally the body of water needs to have a depth of 500 m. This water depth is needed for the formation of the fracturing system. This parameter is obtained by comparing the elevation of the crater rim and floor. A depth of 500 m is supported by 160 craters (Fig. 10.5). The standing body of a certain water depth is an important key parameter for this origin type, consequently the crater needs to have a certain depth. To further support the presence of a crater lake, terraces need to be observed. Within 80 FFCs terraces have been observed. Furthermore, linear features (80) and partially or completely fractured crater floors (300) are other key parameters (Fig. 10.4).

The distribution of the 11 FFCs shows 7 craters in the Arabia Terra region (Fig. 10.10). That region is known for glacial and fluvial activity and a high level of erosion. One crater is located in the Hellas basin and one at the Libya Montes region at 5°N and 100°E. The remaining two craters are located in the Martian highlands, they both have a probability of 65 %. The fracturing within the two craters could have developed through a combination of origin types. That would explain the relatively low probability.

29 FFCs have been classified to have an origin due to subsurface ice (Fig. 10.9). The probability distribution shows just a few FFCs that fulfill less than 40 or more than 80 % of the key parameters. The highest probabilities are mainly arranged between 40 and 70 % (Fig. 10.8). This supports the assumption that glacial and fluvial features are present around many craters but certain key parameters are absent, which results in the small amount of FFCs finally classified for this origin.

The model of subsurface ice was established to explain the chaotic terrains on Mars [Burr et al., 2002, Carr, 1996, Leask et al., 2007, Manker and Johnson, 1982, Massé et al., 2008, Pedersen and Head, 2011, Rodriguez et al., 2005, Sato et al., 2010, Sharp, 1973]. The case study for this origin type was based on Aram Chaos, which is located within the chaotic terrain region [Zegers et al., 2010].

This origin type relates to regions that were formed and modified by fluvial and glacial activity. Chaotic and fretted terrain regions, and the dichotomy boundary of Mars (Fig. 6.1 & 6.2) are of high importance for this origin model. 190 FFCs are found close to the boundary region and 64 craters are located at fretted or chaotic terrains.

The crater surrounding is defined the same way as for the previous water and ice related origins. Most of the FFCs support these key parameters, resulting in no reduction of potential crater candidates and no definite classification (Fig. 10.6).

The fracturing model requires a crater diameter above 100 km and an infilling thickness between 3,500 and 4,000 m. 10 craters have a diameter above 100 km (Fig. 10.2) and just 5 craters have such a high amount of infilling (Fig. 10.3). The key parameters drastically reduce the amount of FFCs for this origin model. Melting subsurface ice causes the floor fracturing, so collapse features and no uplift of the crater floor are expected. 360 FFCs do not indicate an uplifted crater floor and 150 craters show depression features. Various types of fracturing are supported by this model (Fig. 10.4).

The distribution map shows 23 FFCs of this origin type in the Arabia Terra region and along the outflow channels and chaotic terrains at 0°N and 30°W (Fig. 10.10). These locations were expected, because they are highly influenced by fluvial and glacial activity and the model was originally established to explain the formation of chaotic terrains on Mars. Two craters along the boundary and four craters in the Martian highlands are also classified as fractured by subsurface ice, but these six craters have a probability for this origin type below 60 %.

39 craters were determined to have been developed through groundwater migration (Fig. 10.9). The probability distribution is similar to the distribution for Rayleigh convection and shows a flat curve without a recognizable peak. The FFCs are regularly distributed between probabilities of 40 and 70 %. 29 craters are found with a probability above 70 % (Fig. 10.8).

The model of groundwater migration was developed for chaotic terrains on Mars [Andrews-Hanna and Phillips, 2007, Carr, 1996, Clifford, 1993, Russell and Head, 2007]. The Xanthe Terra region was used as a case study to analyze Earth fissuring, seepage and piping [Sato et al., 2010]. A critical flow velocity of the subsurface

water is needed in order to transport soil particles, resulting in subsurface void development and finally, fracturing.

Slope values are essential for subsurface water to reach this critical flow velocity. No information is available about the subsurface slope. Models predicting these values are not reliable because many local and regional parameters have an influence on subsurface water flow. Due to this fact, I chose the dichotomy boundary area as indicator for high velocity of subsurface water. 189 FFCs are located close to the boundary (Fig. 6.1). Volcanic regions are also important for this origin model, since increases in the temperature of the subsurface are necessary in order to melt deposited subsurface ice. 135 FFCs in the vicinity of volcanic regions have been identified (Fig. 6.4).

Additionally, glacial and fluvial features should be observed around the crater, similar to the other origin models (Fig. 10.6). Consequently, they do not reduce the amount of potential FFCs fractured by groundwater migration.

Large crater diameters are preferentially fractured through this origin model. 10 FFCs have a diameter larger than 100 km (Fig. 10.2). The fracturing caused by this origin can be deeper than the infilling. The depth of infilling is therefore, not relevant. Depressions in the fractures are an indicator for collapse processes due to subsurface voids. They can be observed in 150 FFCs. Terraces support the idea of water on the surface and are also a parameter for this origin model. However, terraces are observed within only 80 FFCs. The fracturing can be along the rim, partially, or in the entire crater floor, depending on the amount of transported material and erosion. The majority of craters (330) supports these fracturing types (Fig. 10.4).

Most of the craters classified as developed by groundwater migration are located close to the dichotomy boundary in Arabia Terra and along the chaotic terrains (Fig. 10.10). This distribution was expected, because the surface slope is high at the boundary region. The transition zone between the southern highlands and northern lowlands can range up to several kilometers, but the overall slope is recognizable regardless. The slope supports the subsurface flow of water and the main reason for seepage and piping of the crater floors. Some individual FFCs are located in the Martian highlands, close to tectonic systems, but also volcanic areas. These craters are likely developed by a mixture of formation processes.

The four models described above differ in some parameters from each other, but the crater contexts are identical for each model. This is because the models all include glacial and fluvial features, erosion, and channels. The established tools cannot clearly classify FFCs uniquely to one of the four different origin types related to ice and water processes. The key parameters are too similar, or too few significant differences are defined. The probability of many FFCs for the Rayleigh convection model is high because the parameters are very broad and, additionally, no spatial border is defined. Deep-water fault systems have the same broad context parameters and no spatial limitation, but those craters must be closed basin lakes, which are generally rare on Mars. This key parameter minimizes the amount of FFCs for this origin and makes it the least probable origin model for FFCs. The subsurface ice and groundwater migration models have probabilities between the two near-surface tensile stress models (Rayleigh convection and deep-water fault systems). They are both linked to particular regions on Mars and require large crater diameters. Fewer FFCs have an origin related to subsurface ice because the model requires a very thick layer of infilling, which is rarely observed in FFCs.

## 11.2. Three Final Origin Types

Rayleigh convection, deep-water fault systems, subsurface ice, and groundwater migration can be combined into one ice and water related origin type. This type is clearly distinguishable from the volcanic and tectonic origin types. The new distribution (Fig. 11.1) illustrates that more than 40 % (187) of the FFCs on Mars are fractured due to water and ice related processes, which represents the dominating fracturing origin. Water and ice related processes can be found at various locations on Mars (Fig. 11.2). They prevail along the dichotomy boundary and the large outflow systems and chaotic terrains on Mars. Even in the southern highlands, erosion has occurred. It is difficult to distinguish between those processes which formed the fracturing and those which modified the fractured craters afterwards. No distinction is made between formation and modification processes in the tools. Consequently, the amount of classified FFCs is high for the glacial and fluvial fracturing origin.

Volcanic processes, which are the only explanation for Lunar FFCs, are responsible for fracturing 15 % (64) of the FFCs on Mars. The origin type is limited to areas that do not show a high amount of erosion, fluvial, and glacial activity. This origin type is not the most dominant.

Tectonic activity forms 20 % (86) of the Martian FFCs. Not only large scale graben systems in the highlands, but also the dichotomy boundary shows tectonic activity that could be included in the floor fracturing process. Tectonic activity is also linked to outflow because subsurface ice can melt through, increasing pressure and temperature near the tectonically active regions.

More than 20 % (96) craters are not classifiable with the developed tools. 50 % or less of the key parameters are fulfilled by those craters. This can be explained in several ways. The fracturing of the crater floor could be developed by a mixture of formation models. Some surface features would support one type and others a different type. In total, no clear classification can be achieved and the FFC not classified. Another option would be the formation by one origin model, but the important key parameters are not observable any more, due to erosion or superposition. The last possibility is a so far unknown fracturing model that occurs mainly in the Martian highlands, but also along the dichotomy boundary.

## 11.3. Limits of the Classification Tools

The quality of the classification depends on the database quality. The tools use the information stored in the database. Mistakes or incorrect information would influence the tool results. Not only the database, but also the definition of the key parameters for each classification tool are essential for the quality. The key parameters influence the quality of the classification and need to be chosen based on, e.g. detailed case studies or previous research.

Automated classification tools do not deliver reliable results when the involved geologic processes are not clearly distinguishable. The tools cannot distinguish between the different water and ice related origin types. The used key parameters and the observed morphological features are too similar. To identify the origin type, the FFCs need to be analyzed in detail. Further research on these origin types could increase the knowledge of fracture formation and more key parameters could be defined. However, defining geologic processes and establishing rules and dependencies are complicated because reality does not always follow defined rules. Previous research and the case study (Chapter 9) show that even a detailed analysis of FFCs

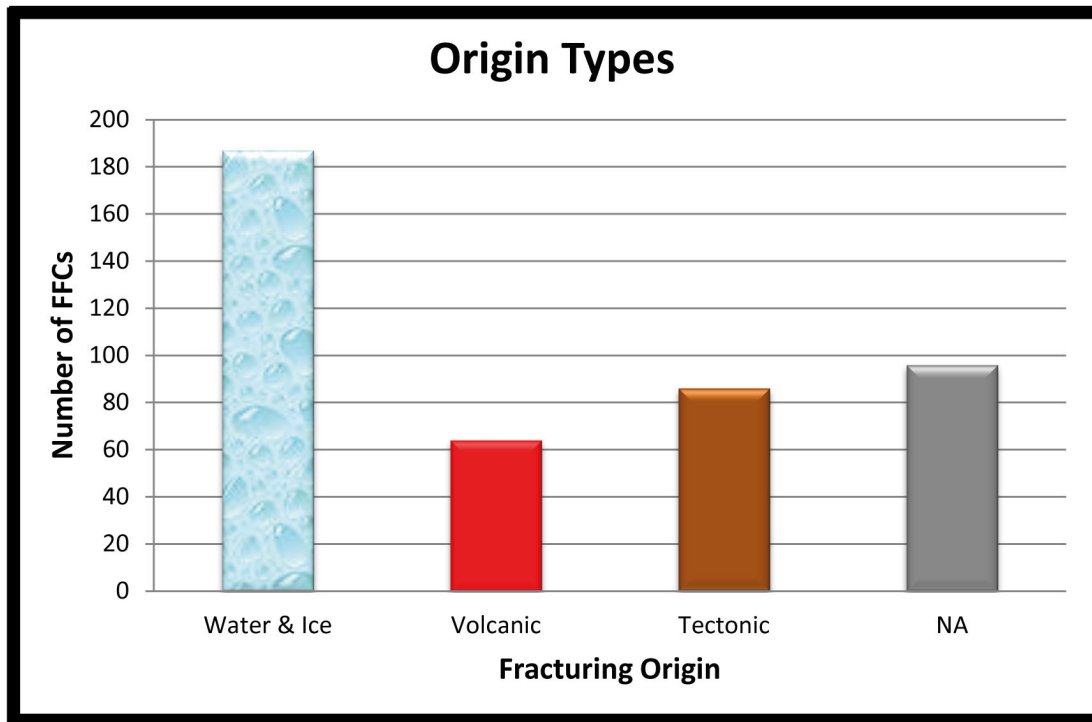


Figure 11.1.: FFC formation on Mars can be divided into three different types: water and ice, volcanic, and tectonic related processes. Some craters are not classifiable (NA) with the developed, automated tools.

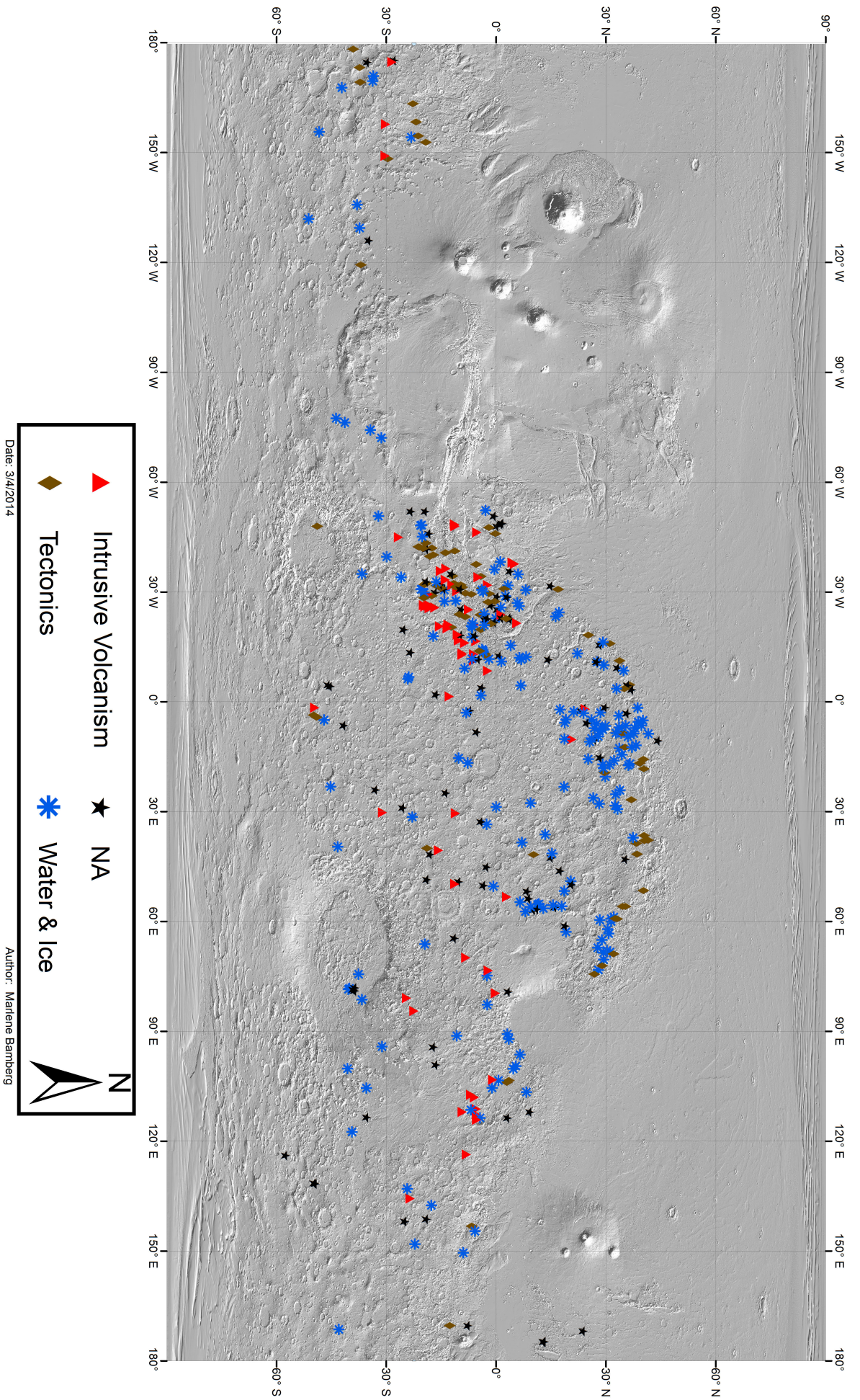
does not always indicate a clear defined origin type. Geologic processes are related to each other and were active over the last billion years. The crater morphologies that are observed today have been modified and eroded and make it difficult to reconstruct the past environment and prevailing conditions. Due to this, even a detailed, high quality analysis might not answer the question of the fracturing origin for craters where related geologic processes or a variety of different processes were active.

The most probable origin type is selected by comparing the probability values of each origin model. The origin with the highest value is automatically defined as most probable fracturing process. The difference to the second most probable is not taken into account. The probability values could be nearly identical or totally different, the result of the classification is the same. Information about the relationship of different formation processes for one FFCs are not considered for the classification, but the information is stored in the database and can be accessed by the user.

## 11.4. Comparison of Manual and Automated Analysis

Two craters were analyzed with both, a conventional manual (Chapter 5 & 9) and an automated approach (Chapter 7 & 10).

With the manual analysis, the observed surface features supported three potential fracturing models for Crater A. The model of groundwater migration, Rayleigh convection, and deep-water fault systems are possible origins for the floor-fracturing. No evidence for tectonic systems and intrusive volcanism were found. With the



*Figure 11.2.: Global map of FFG formation on Mars divided into three different types: water and ice, volcanic, and tectonic related processes. Some craters are not classifiable (NA) with the developed, automated tools.*

automated approach, the fracturing for this crater is classified in the database as Rayleigh convection. However, the probability difference of fluvial and glacial related models is small. The automated analysis provides information about the probabilities of all fracturing models. The probability values are stored in the database and yield additional information for the user.

As already discussed, fluvial and glacial processes are too similar to be classified by automated tools. However, the same problem was observed in the case study. The fracturing origin could not clearly be identified with the manual analysis. In addition, it is difficult to determine a more probable origin model with the manual analysis. The origin model of a FFC is classified clearly, if involved geologic processes form defined surface features, in which case, FFC classification is reliable with a manual and automated approach.

Crater Lipany is an example for a high probability classification and reliable result. The fracturing model for that FFC has been identified in both studies as intrusive volcanism.

## 11.5. Advantages

After establishing the database, including all required information and defining the tool parameters, running the tools themselves takes less than 10 seconds. Establishing the database takes most of the effort and time. Certain information needs to be available for the tool application. Developing a database about FFCs within a GIS is also recommended for a manual analysis and interpretation for each FFC. Often those databases already exist. The database, itself, can also be changed and updated based on new, high resolution images. It is also possible to add new parameters. Newly discovered FFCs can be included or entries can be removed from the database.

Defining the tool parameters is based on case studies and previous research. The difficulty is to develop definitions of geological processes or morphologies characterizing the possible origin types, but this is precisely the reason why the tools obtain reproducible results. They are based on defined and set key parameters. Those parameters can be easily changed when needed and the tools can be run again for the entire database or just selected craters. New results can be seen directly and possible changes compared and discussed.

The automated tools make a global study of FFC classification possible. Without the tools every crater would have to be classified individual and manually by the user, which would be very time consuming and hardly reproducible and comparable. The tools provide parameters that were obtained by defined geostatistical techniques. Hence, the tools guarantee a consistent quality of results. Analysis tools provide additional information and help to the user and are therefore considered assistance systems.





## 12. Summary & Conclusion

This research shows that automated tools, including measurements and classifications can successfully operate global statistical analyses in a short amount of time. The statistical analyses were applied to FFCs on Mars and revealed probabilities of different origin processes.

### 12.1. Technical Results

The purpose of this study was to develop automated analysis tools that focus on statistical parameters. It is possible to conduct an automated statistical analysis of morphologic and geologic surface features based on analysis tools. The tools provide parameters that were obtained by defined geostatistical techniques. Hence, the tools guarantee a consistent quality of results. This also includes achieving reliable, comparable, and usable results, but also reducing the time and effort of conducting such studies. These tools describe the base for a standardized analysis method, which could be adapted to several research topics. Analysis tools provide additional information and help to the user and are therefore considered assistance systems.

Tools were developed for this purpose and tailored to answer a specific research question. The tools are organized in a hierarchic order and follow the principle of dependency. The tools are ordered in three dependency levels. The first level is a set of measurements, which also represent the basis for geoscientific analyses. They are followed by calculations that provide more information about the surface morphology. The final level includes the classifications, which is the end product of the quantitative research.

Translating geologic processes into important key parameters, boundary conditions and rules, which could then be implemented into the tools was a time consuming process. The key parameters and boundary conditions need to be defined precisely. This requires knowledge about the research topic. Case studies and previous research can help to define the needed parameters. The tools were coded within Python and later imported and run in ArcGIS. The quality of the tool results is hardly influenced by the quality and accuracy of the tool definitions, which depend on the research question itself.

There are only a few databases available for surface features on Mars. Establishing a database for the key parameters is another time consuming process, but also the base for several quantitative and qualitative analyses. All features that should be classified must be included in the database. Important key parameters must be included in the database, as well. These include spatial information, environmental context, and small scale surface features. The quality of the database directly influences the results. The software systems ArcGIS and JMars were used for this task. As soon as a database is established, it can be adapted to various research questions, it can also be easily updated and shared. The database increases the flexibility and reproducibility of any experiment it is used in. The set rules for the classifications increase the comparability of the research.

Once the database and the tools have been produced, they operate automatically. Calculations and classifications can be applied to the entire database or just selected features. Running the tools within a database takes only a few seconds and the results are shown within the database.

Related geologic processes, such as glacial and fluvial activity, are too similar to be classified by the automated tools or the manual approach. That was observed by comparing the results of the two case study craters. In addition to the unclear origin type, it is difficult to determine a more probable origin model with the manual analysis. The automated tools provide probability values for each origin model. The classification tools cannot achieve proper results if the probability of a classification is below 50 %. To guarantee the quality and reliability of the results, unclassifiable features need to be labeled. Those features have to be manually analyzed in detail. Another possibility would be the improvement of key parameters and rules for the classification. The discussion and interpretation of the results is still the task of the user.

## 12.2. Scientific Results

433 FFCs were observed on Mars. This crater type was not found in the northern lowlands, on volcanic lava sheets, or close to the poles. All FFCs were found within a latitude of 45°N and 60°S. They are located along the dichotomy boundary, close to chaotic terrains, tectonic systems, and volcanic regions within the Martian highlands. This observation is comparable to the research done by Bamberg et al. [2014], Korteniemi [2003], Korteniemi et al. [2006].

Most FFCs were identified as central peak complex craters. All observed FFCs are filled by 1,800 m of material on average. The observed surface features and the context of each crater differ considerably. This leads to the assumption that the fracturing did not always develop by the same process. Various processes can lead to fracturing of the crater floor. We described six potential fracturing models:

- Intrusive Volcanism
- Tectonic Systems
- Groundwater Migration
- Subsurface Ice
- Rayleigh Convection
- Deep-Water Fault Systems

Parameters and rules were defined for each origin type, which helped to identify the presence of these processes. Surface features were observed and measured in the environmental context and the crater interior. Additionally, spatial data were used to analyze the location of each crater. It was verified whether the crater was located close to volcanic regions, tectonic systems, chaotic and fretted terrains, or the dichotomy boundary. All parameters were taken into account for each origin model. The six origin models were divided into clearly observable geologic processes. This results in the combination of the Rayleigh convection, subsurface ice, groundwater migration, and deep-water fault systems models into one origin type related to ice and water activity.

For the FFCs on Mars, three major origin types were identified. Each type represents different geologic processes, environments, and locations on Mars. The main process to develop floor fracturing is the combination of water and ice activity. At 43 % (187) of the FFCs on Mars, glacial and fluvial processes are significantly involved in the fracturing. The FFCs are located mainly along the dichotomy boundary of Mars and the outflow channels. Surprisingly, several craters were found within the Martian highlands. Erosion due to fluvial and glacial activity modifies craters and also erases surface features indicating different geologic processes. Within the Martian highlands, it is unknown if the fluvial and glacial processes lead to the fracturing event, itself, or modified the crater morphology after it was already fractured through other processes. 20 % (86) of the FFCs are fractured by tectonic activity. Large tectonic systems damage the crater rim and intersect the crater. This initiates the fracturing process and it developed further throughout the crater floor. This fracturing type was found at large scale scarps in the Martian highlands, along the chaotic terrains and outflow channels, and at the dichotomy boundary. The last origin type is intrusive volcanism and 15 % (64) of the FFCs were classified as developed by this process. The FFCs were found in vicinity to volcanic regions, mainly Daedalia Planum, Syria Planum, Syrtis Major, and Hesperia Planum in the Martian highlands and nearby the chaotic terrains.

For more than 75 % (337) of the FFCs, an origin type was identified. 25 % (96) FFCs, mainly located in the Martian highlands and along the dichotomy boundary, could not be classified to one of the fracturing models. This can be explained in several ways. A mixture of origin models, resulting in no clear classification, could develop the fracturing of the crater floor. Another option would be the fractures formed by only one origin model, but the important key parameters are not observable any more, due to erosion or superposition. The last possibility is that fracturing could occur from a so far unknown fracturing model.



## 13. Future Work

Potential future work can be focused on increasing the quality of the developed classification tools and also testing the automated classification methods on different planetary bodies and surface features.

### 13.1. Technical Improvements

The classification tools can be developed further, so that they provide even more information to the user. One option would be to set the obtained origin type probabilities in relation to each other. So far, the maximum probability value is given as most potential origin type. The tools do not consider the probability difference between the origin types, but it can be seen in the database. The origin type would be easier interpretable and additional information of the classification would be gained by adding a calculation of absolute values of probability. The origin type probability would not be only presented in relative percentages but in ratios. E.g. a FFC with a probability of 50 % developed by intrusive volcanism and 80 % developed by tectonic activity would be formed by tectonics 1.6 times more likely than due to intrusive volcanism.

The database could be extended and more parameters of importance added. Spectral information could be included as key parameters in the classification tools regarding glacial and fluvial processes, to improve the reliability of the results. Global maps of minerals need to be available for this research. Spectral data are available by the Compact Reconnaissance Imaging Spectrometer for Mars (CRISM), the Visible and Infrared Mineralogical Mapping Spectrometer (OMEGA), the Thermal Emission Spectrometer (TES), and the Thermal Emission Imaging System (THEMIS). Research has been done on mineral compositions of the Martian surface, which could be also taken into account [Christensen et al., 2001, 2004, Ehlmann et al., 2011, Langevin et al., 2005, Mustard et al., 2008, Poulet et al., 2005].

Mineralogy can also be used to indicate surface processes and past environments. The most important and characteristic minerals indicating water on the Martian surface are Chlorides, Sulfates, and Phyllosilicates (e.g. Carr [2006], Kiefer [2004]).

For the development of Phyllosilicates, a standing body of water (paleolake) is needed. They settle and deposit first and would, consequently, likely be found at the bottom of the stratigraphy [Velde, 1995]. The presence of these minerals would support the existence of a paleolake and could be an additional key parameter for the deep-water fault system origin. Sulfates develop in shallow water and require very high saturation rates. These minerals are often deposited on top of Phyllosilicates. Chlorides need very high evaporation rates and are deposited in playa lakes and are usually found on top of the sulfate deposits [Osterloo et al., 2010]. The spectrometer data show the presence of the minerals, but it is unclear if they developed in situ or have been transported and deposited. It is also unknown if the deposited minerals had any influence on the fracturing or were deposited after the fracturing process. The development of minerals within the crater can hardly be defined to an age.

To increase the precision of the measured data a digital terrain model with a higher resolution could be used. For this research MOLA data are used because a global elevation map is available. HRSC DTMs have a better resolution, but lack global coverage. The accuracy of elevation measurements and depth calculations would increase with global HRSC data and could have an influence on the classifications.

## 13.2. Scientific Applications

Crater size frequency distributions were conducted for two craters within the case study. Age determination for FFCs developed by the three different origin models could help to get information about the chronology of events. The fracturing process in each crater could be randomly active or a model could occur in a certain time period. It is also possible that all models are active in the same time range. This would give further information about the expected erosion and modification of the craters after the fracturing process. It could also provide information on the climate history on Mars.

A comparison between Martian and Lunar FFCs could yield further information into fracturing processes on different planetary bodies. The Lunar FFCs could be compared to the FFCs with a tectonic and volcanic origin on Mars regarding size, depth, fracturing types, and observed surface features. Observed differences or similarities between the FFCs need to be understood and explained to gain more information about subsurface processes. Icy satellites could also be a potential target for searching for FFCs developed in a glacial and fluvial environment. However, the FFC identification on these bodies is more difficult due to the coverage and changing resolution and illumination of image data.

The classification tools can also be adapted to other surface features that should be classified on a global scale. The rules for every classification need to be defined and the database containing the key parameters needs to be established. Potential surface morphologies are various types of impact craters, layered deposits, mass wasting features, dunes, channels, channel networks, tectonic features or deltas.

# Bibliography

- Anderson, D., Mann, M., Mar. 1989. VICAR Image Processing Using Unix, X Windows, and CDROMS. In: Lunar and Planetary Institute Science Conference Abstracts. Vol. 20 of Lunar and Planetary Inst. Technical Report. p. 17.
- Anderson, R. C., Dohm, J. M., Haldemann, A. F. C., Pounders, E., Golombek, M., Castano, A., Jun. 2008. Centers of tectonic activity in the eastern hemisphere of Mars. *Icarus* 195, 537–546.
- Andrews-Hanna, J. C., Phillips, R. J., 2007. Hydrological modeling of outflow channels and chaos regions on mars. *Journal of Geophysical Research* 112, ID E08001.
- Andrews-Hanna, J. C., Zuber, M. T., Arvidson, R. E., Wiseman, S. M., Jun. 2010. Early Mars hydrology: Meridiani playa deposits and the sedimentary record of Arabia Terra. *Journal of Geophysical Research (Planets)* 115, 6002.
- Aureli, K. L., Head, J. W., Goudge, T. A., Fassett, C. I., Mar. 2013. An Analysis of Candidate Closed-Basin Lakes in Impact Craters on Mars. *LPI Contributions* 1719, 1244.
- Bamberg, M., Jaumann, R., Asche, H., Kneissl, T., Michael, G. G., 2014. Floor Fractured Craters on Mars- Observations and Origin. *Planetary and Space Science* (10.1016/j.pss.2013.09.017), 146–162.
- Bandfield, J. L., Hamilton, V. E., Christensen, P. R., Mar. 2000. A Global View of Martian Surface Compositions from MGS-TES. *Science* 287, 1626–1630.
- Baratoux, D., Pinet, P., Toplis, M. J., Mangold, N., Greeley, R., Baptista, A. R., Aug. 2009. Shape, rheology and emplacement times of small martian shield volcanoes. *Journal of Volcanology and Geothermal Research* 185, 47–68.
- Barlow, N. G., 1988. Crater size-frequency distributions and a revised martian relative chronology. *Icarus* 75, 285–305.
- Barlow, N. G., 2008. *Mars- An Introduction to its Interior, Surface and Atmosphere*. Cambridge University Press.
- Barlow, N. G., Perez, C. B., 2003. Martian impact crater ejecta morphologies as indicators of the distribution of subsurface volatiles. *Geophysical Research Letters* 108, 4-1-4-10.
- Boyce, J. M., Garbeil, H., Aug. 2007. Geometric relationships of pristine Martian complex impact craters, and their implications to Mars geologic history. *Geophysical Research Letters* 34, 16201.
- Brennan, W. J., 1975. Modification of preare impact craters by volcanism and tectonism. *The Moon* 12, 449–461.

- Budhu, M., 2008. Mechanics of earth fissures using the mohr-coulomb failure criterion. *Environmental & Engineering Geoscience* 14, 281–295.
- Burr, D. M., Grier, J. A., McEwen, A. S., Keszthelyi, L. P., Sep. 2002. Repeated Aqueous Flooding from the Cerberus Fossae: Evidence for Very Recently Extant, Deep Groundwater on Mars. *Icarus* 159, 53–73.
- Burrough, P. A., 1986. *Principles of Geographical Information Systems for Land Resources Assessment*. Clarendon Press, Oxford.
- Cabrol, N. A., Grin, E. A., 1999. Distribution, classification and ages of martian impact crater lakes. *Icarus* 142, 160–172.
- Carr, M. H., 1996. *Water on Mars*. Oxford University Press.
- Carr, M. H., 2006. *The Surface of Mars*. Cambridge University Press.
- Cartwright, J., James, D., Bolton, A., Jan. 2003. The genesis of polygonal fault systems: a review. *Geological Society of London Special Publications* 216, 223–243.
- Christensen, P., Engle, E., Anwar, S., Dickenshied, S., Noss, D., Gorelick, N., Weiss-Malik, M., April 2013. Jmars- a planetary gis.  
URL <http://adsabs.harvard.edu/abs/2009AGUFMIN22A..06C>
- Christensen, P. R., Bandfield, J. L., Hamilton, V. E., Ruff, S. W., Kieffer, H. H., Titus, T. N., Malin, M. C., Morris, R. V., Lane, M. D., Clark, R. L., Jakosky, B. M., Mellon, M. T., Pearl, J. C., Conrath, B. J., Smith, M. D., Clancy, R. T., Kuzmin, R. O., Roush, T., Mehall, G. L., Gorelick, N., Bender, K., Murray, K., Dason, S., Greene, E., Silverman, S., Greenfield, M., Oct. 2001. Mars Global Surveyor Thermal Emission Spectrometer experiment: Investigation description and surface science results. *Journal of Geophysical Research* 106, 23823–23872.
- Christensen, P. R., Jakosky, B. M., Kieffer, H. H., Malin, M. C., McSween, Jr., H. Y., Neelson, K., Mehall, G. L., Silverman, S. H., Ferry, S., Caplinger, M., Ravine, M., Jan. 2004. The Thermal Emission Imaging System (THEMIS) for the Mars 2001 Odyssey Mission. *Space Science Review* 110, 85–130.
- Clifford, S. M., 1993. A model for the hydrologic and climatic behavior of water on mars. *Journal of Geophysical Research* 98, 10973–11016.
- Cooke, M., Islam, F., McGill, G., Sep. 2011. Basement controls on the scale of giant polygons in Utopia Planitia, Mars. *Journal of Geophysical Research (Planets)* 116, 9003.
- Craddock, R. A., Howard, A. D., 2002. The case for rainfall on a warm, wet early mars. *Geophysical Research Letters* 107, 21–1–21–36.
- Dohm, J. M., Barlow, N. G., Anderson, R. C., Williams, J.-P., Miyamoto, H., Ferris, J. C., Strom, R. G., Taylor, G. J., Fairén, A. G., Baker, V. R., Boynton, W. V., Keller, J. M., Kerry, K., Janes, D., Rodriguez, J. A. P., Hare, T. M., Sep. 2007. Possible ancient giant basin and related water enrichment in the Arabia Terra province, Mars. *Icarus* 190, 74–92.



- Edgett, K. S., Malin, M. C., 2002. Martian sedimentary rock stratigraphy: Outcrops and interbedded craters of northwest sinus meridiani and southwest arabia terra. *Geophysical Research Letters* 29, 32–1–32–4.
- Ehlmann, B. L., Mustard, J. F., Murchie, S. L., Bibring, J.-P., Meunier, A., Fraeman, A. A., Langevin, Y., Nov. 2011. Subsurface water and clay mineral formation during the early history of Mars. *Nature* 479, 53–60.
- Eliason, E. M., Anderson, J. A., Barrett, J. M., Becker, K. J., Becker, T. L., Cook, D. A., Soderblom, L. A., Sucharski, T. L., Thompson, K. T., Mar. 2001. ISIS Image Processing Capabilities for MGS/MOC Imaging Data. In: *Lunar and Planetary Institute Science Conference Abstracts*. Vol. 32 of Lunar and Planetary Inst. Technical Report. p. 2081.
- ESRI, 08 2013. Arcgis resource center.  
URL <http://resources.arcgis.com/en/help/>
- Facility, M. S. F., April 2013. Webmap of all themis images (2002- present).  
URL <http://global-data.mars.asu.edu/bin/themis.pl>
- Fairén, A. G., Dohm, J. M., Baker, V. R., de Pablo, M. A., Ruiz, J., Ferris, J. C., Anderson, R. C., Sep. 2003. Episodic flood inundations of the northern plains of Mars. *Icarus* 165, 53–67.
- Fassett, C. I., Head, J. W., 2007. Layered mantling deposits in northeast arabia terra, mars: Noachian-hesperian sedimentation, erosion, and terrain inversion. *Journal of Geophysical Research* 112, ID E08002.
- Fassett, C. I., Head, J. W., 2008. The timing of martian valley network activity: Constraints from buffered crater counting. *Icarus* 195, 61–89.
- Ferrill, D. A., Wyrick, D. Y., Morris, A. P., Sims, D. W., Franklin, N. M., 2004. Dilational fault slip and pit chain formation on mars. *GSA Today* 14, 4–12.
- Gaddis, L., Anderson, J., Becker, K., Becker, T., Cook, D., Edwards, K., Eliason, E., Hare, T., Kieffer, H., Lee, E. M., Mathews, J., Soderblom, L., Sucharski, T., Torson, J., McEwen, A., Robinson, M., Mar. 1997. An Overview of the Integrated Software for Imaging Spectrometers (ISIS). In: *Lunar and Planetary Institute Science Conference Abstracts*. Vol. 28 of Lunar and Planetary Inst. Technical Report. p. 387.
- Garvin, J. B., Sakimoto, S. E. H., Frawley, J. J., 2003. Craters on mars: Global geometric properties from gridded mola topography. *Sixth International Conference on Mars July 20-25 2003, Pasadena, California*, abstract no.3277.
- Gasselt, S. v., 2007. Cold-climate landforms on mars. Ph.D. thesis, Free University Berlin.
- GDAL, April 2013. Gdal - geospatial data abstraction library.  
URL <http://www.gdal.org/>
- Gomarasca, M., 2004. *Basics of Geomatics*. Springer.
- Greeley, R., Guest, J., 1987. *Geologic map of the eastern equatorial region of Mars*. USGS.

- Grott, M., Baratoux, D., Hauber, E., Sautter, V., Mustard, J., Gasnault, O., Ruff, S. W., Karato, S.-I., Debaille, V., Knapmeyer, M., Sohl, F., Van Hoolst, T., Breuer, D., Morschhauser, A., Toplis, M. J., Jan. 2013. Long-Term Evolution of the Martian Crust-Mantle System. *Space Science Review* 174, 49–111.
- Gwinner, K., Scholten, F., Giese, B., Oberst, J., Jaumann, R., Spiegel, M., Schmidt, R., Neukum, G., 2005. Hochauflösende Digitale Gelaendemodelle der Marsoberflaeche auf der Grundlage von Mars Express HRSC Daten. *PFG* 5, 387–394.
- Gwinner, K., Scholten, F., Preusker, F., Elgner, S., Roatsch, T., Spiegel, M., Schmidt, R., Oberst, J., Jaumann, R., Heipke, C., Jun. 2010. Topography of Mars from global mapping by HRSC high-resolution digital terrain models and orthoimages: Characteristics and performance. *Earth and Planetary Science Letters* 294, 506–519.
- Hanna, J. C., Phillips, R. J., 2006. Tectonic pressurization of aquifers in the formation of mangala and athabasca valles, mars. *Journal of Geophysical Research* 111, ID E03003.
- Hartmann, W., Strom, R., Weidenschilling, S., Blasius, K., Voronow, A., Dence, M., Grieve, R., Diaz, J., Chapman, C., Shoemaker, E., Jones, K., 1981. *Basaltic Volcanism on the Terrestrial Planets*. Pergamon Press Inc.
- Hartmann, W. K., 1985. *Astronomy: the Cosmic Journey*, 3rd Edition. Astronomy Ser. Wadsworth.
- Hartmann, W. K., Neukum, G., 2001. Cratering chronology and the evolution of mars. *Space Science Reviews* 96, 165–194.
- Hauber, E., Bleacher, J., Gwinner, K., Williams, D., Greeley, R., Aug. 2009. The topography and morphology of low shields and associated landforms of plains volcanism in the Tharsis region of Mars. *Journal of Volcanology and Geothermal Research* 185, 69–95.
- Hiesinger, H., Head, J. W., 2000. Characteristics and origin of polygonal terrain in southern utopia planitia, mars: Results from mars orbiter laser altimeter and mars orbiter camera data. *Journal of Geophysical Research* 105, 11999–12021.
- Hockey, T., Barnet, C., May 1994. A DOS-based Version of the VICAR Image Processing System for Planetary Image Reduction, Navigation, and Measuring. In: *American Astronomical Society Meeting Abstracts #184*. Vol. 26 of *Bulletin of the American Astronomical Society*. p. 900.
- Holzer, T. L., Pampeyan, E. H., 1981. Earth fissures and localized differential subsidence. *Water Resources Research* 17, 223–227.
- Horacio, J., Ollero, A., 2011. Geomorphological classification of fluvial ssystem from g.i.s. tools. *Boletin de la Asociacion de Geografos Espanoles* 56, 479–482.
- Ivanov, B. A., 2001. Mars/moon cratering rate ratio estimates. *Space Science Reviews* 96, 87–104.
- Jaumann, R., Nass, A., Tirsch, D., Reiss, D., Neukum, G., 2010. The western libya montes valley system on mars: Evidence for episodic and multi-genetic erosion events during the martian history. *Earth and Planetary Science Letters* 294, 272–290.

- Jaumann, R., Neukum, G., Behnke, T., Duxbury, T. C., Eichertopf, K., Flohrer, J., Gasselt, S. V., Giese, B., Gwinner, K., Hauber, E., Hoffmann, H., Hoffmeister, A., Köhler, U., Matz, K.-D., McCord, T. B., Mertens, V., Oberst, J., Pischel, R., Reiss, D., Ress, E., Roatsch, T., Saiger, P., Scholten, F., Schwarz, G., Stephan, K., Wählisch, M., HRSC Co-Investigator Team1, May 2007. The high-resolution stereo camera (HRSC) experiment on Mars Express: Instrument aspects and experiment conduct from interplanetary cruise through the nominal mission. *Planetary and Space Science* 55, 928–952.
- Jennings, N., 2011. A Python Primer for ArcGIS. Create Space Independent Publishing Platform.
- Jodlowski, P., Platz, T., Michael, G. G., Mar. 2012. Preliminary Eruption History of the Syrtis Major Volcanic Province, Mars. In: Lunar and Planetary Institute Science Conference Abstracts. Vol. 43 of Lunar and Planetary Inst. Technical Report. p. 2494.
- Jong, S., Van der Meer, F., 2004. Remote sensing image analysis: including the spatial domain. Remote Sensing and Digital Image Processing Series. Kluwer Academic.  
URL <http://books.google.de/books?id=uFBreFpwPzgC>
- Joseph, G., Feb. 2000. How well do we understand Earth observation electro-optical sensor parameters? *International Journal of Photogrammetry and Remote Sensing* 55, 9–12.
- Jozwiak, L. M., Head, J. W., Neumann, G. A., Zuber, M. T., Smith, D. E., Mar. 2012. Lunar Floor-Fractured Craters: Classification, Distribution, and Implications for Magmatism and Shallow Crustal Structure. In: Lunar and Planetary Institute Science Conference Abstracts. Vol. 43 of Lunar and Planetary Inst. Technical Report. p. 1512.
- Kiefer, W. S., 2004. Gravity evidence for an extinct magma chamber beneath syrtis major, mars: a look at the magmatic plumbing system. *Earth* 222, 349–361.
- Kneissl, T., Michael, G., Mar. 2013. Crater Size-Frequency Measurements on Linear Features - Buffered Crater Counting in ArcGIS. LPI Contributions 1719, 1079.
- Kneissl, T., van Gasselt, S., Neukum, G., Mar. 2010. Measurement of Strike and Dip of Geologic Layers from Remote Sensing Data - New Software Tool for ArcGIS. In: Lunar and Planetary Institute Science Conference Abstracts. Vol. 41 of Lunar and Planetary Institute Science Conference Abstracts. p. 1640.
- Kneissl, T., van Gasselt, S., Neukum, G., Sep. 2011. Map-projection-independent crater size-frequency determination in GIS environments- New software tool for ArcGIS. *Planetary and Space Science* 59, 1243–1254.
- Korteniemi, J., 2003. Collapses and depressions post-dating crater formation in martian impact structures - distribution and consequences. Third International Conference on Large Meteorite Impacts August 5-7, 2003, Noerdlingen, Germany, abstract no.4091.

- Korteniemi, J., Aittola, M., Lahtela, H., Öhman, T., Raitala, J., Mar. 2006. Martian Floor-fractured Craters vs. Craters with Irregular Depressions. In: Mackwell, S., Stansbery, E. (Eds.), 37th Annual Lunar and Planetary Science Conference. Vol. 37 of Lunar and Planetary Inst. Technical Report. p. 2145.
- Kresse, W., Danko, D., 2012. Handbook of Geographic Information. Springer.
- Lachenbruch, A. H., 1970. Crustal temperature and heat production: Implication of the linear heat flow relation. *JGR* 75, 3291–3300.
- Lammer, H., Bredehöft, J. H., Coustenis, A., Khodachenko, M. L., Kaltenecker, L., Grasset, O., Prieur, D., Raulin, F., Ehrenfreund, P., Yamauchi, M., Wahlund, J.-E., Griekmeier, J.-M., Stangl, G., Cockell, C. S., Kulikov, Y. N., Grenfell, J. L., Rauer, H., Jun. 2009. What makes a planet habitable? *Springer* 17, 181–249.
- Lane, M. D., Christensen, P. R., 2000. Convection in a catastrophic flood deposit as the mechanism for the giant polygons on mars. *Journal of Geophysical Research* 105, 17617–17627.
- Langevin, Y., Poulet, F., Bibring, J.-P., Gondet, B., Mar. 2005. Sulfates in the North Polar Region of Mars Detected by OMEGA/Mars Express. *Science* 307, 1584–1586.
- Lawhead, J., 2013. Learning Geospatial Analysis with Python. Packt Publishing.
- Leask, H. J., Wilson, L., Mitchell, K. L., Aug. 2007. Formation of Mangala Valles outflow channel, Mars: Morphological development and water discharge and duration estimates. *Journal of Geophysical Research (Planets)* 112, 8003.
- Lemmens, M., 2011. Geo-information: Technologies, Applications and the Environment. *Geotechnologies and the environment*. Springer London, Limited.  
URL [http://books.google.de/books?id=n\\_tUAWYg4UQC](http://books.google.de/books?id=n_tUAWYg4UQC)
- Leverington, D. W., Maxwell, T. A., Jun. 2004. An igneous origin for features of a candidate crater-lake system in western Memnonia, Mars. *Journal of Geophysical Research (Planets)* 109, 6006.
- Luchitta, B., 1983. Permafrost on mars: Polygonally fractured ground. *Permafrost: Proceedings of the 4th International Conference* 4, 744–748.
- Lutz, M., Ascher, D., Tismer, C., 2000. Einführung in Python. O'Reily.
- Malin, M. C., Bell, J. F., Cantor, B. A., Caplinger, M. A., Calvin, W. M., Clancy, R. T., Edgett, K. S., Edwards, L., Haberle, R. M., James, P. B., Lee, S. W., Ravine, M. A., Thomas, P. C., Wolff, M. J., May 2007. Context Camera Investigation on board the Mars Reconnaissance Orbiter. *Journal of Geophysical Research (Planets)* 112, 5.
- Malin, M. C., Edgett, K. S., 2000. Evidence for recent groundwater seepage and surface runoff on mars. *Science* 288, 2330–2335.
- Malin Space Science Systems, I., April 2013. Ctx-coverage.  
URL <http://www.msss.com/news/index.php?id=43>

- Mangold, N., Ansan, V., Baratoux, D., Costard, F., Dupeyrat, L., Hiesinger, H., Masson, P., Neukum, G., Pinet, P., 2008. Identification of a new outflow channel on Mars in Syrtis Major Planum using HRSC/MEX data. *Planetary and Space Science* 56, 1030–1042.
- Manker, J. P., Johnson, A. P., 1982. Simulation of martian chaotic terrain and outflow channels. *Icarus* 51, 121–132.
- Massé, M., Le Mouélic, S., Bourgeois, O., Combe, J.-P., Le Deit, L., Sotin, C., Bibring, J.-P., Gondet, B., Langevin, Y., Dec. 2008. Mineralogical composition, structure, morphology, and geological history of Aram Chaos crater fill on Mars derived from OMEGA Mars Express data. *Journal of Geophysical Research (Planets)* 113, 12006.
- Mather, P., Koch, M., 2011. *Computer Processing of Remotely-Sensed Images: An Introduction*. Wiley.  
URL <http://books.google.de/books?id=GWhvDMNh1hAC>
- McGill, G., 2002. Geologic map transecting the highland/lowland boundary zone, Arabia Terra, Mars. USGS.
- McKay, C. P., Marinova, M. M., Mar. 2001. The Physics, Biology, and Environmental Ethics of Making Mars Habitable. *Astrobiology* 1, 89–109.
- Melosh, H., 1989. *Impact Cratering- a geologic process*. Oxford University Press.
- Michael, G., Neukum, G., Mar. 2008. Surface Dating: Software Tool for Analysing Crater Size-Frequency Distributions Including Those Showing Partial Resurfacing Events. In: *Lunar and Planetary Institute Science Conference Abstracts*. Vol. 39 of *Lunar and Planetary Institute Science Conference Abstracts*. p. 1780.
- Michael, G. G., Neukum, G., 2010. Planetary surface dating from crater size-frequency distribution measurements: Partial resurfacing events and statistical age uncertainty. *Earth and Planetary Science Letters* 294, 223–229.
- Morgenstern, A., Hauber, E., Reiss, D., van Gasselt, S., Grosse, G., Schirmer, L., Jun. 2007. Deposition and degradation of a volatile-rich layer in Utopia Planitia and implications for climate history on Mars. *Journal of Geophysical Research (Planets)* 112, 6010.
- Morris, E. C., Underwood, J. R., 1978. Polygonal fractures of the martian plains. *Reports of planetary geology program 1977-1978*, 97–99.
- Moscardelli, L., Dooley, T., Dunlap, D., Jackson, M., Wood, L., 2012. Deep-water polygonal fault systems as terrestrial analogs for large-scale martian polygonal terrains. *GSA Today* 22, Issue 8, 4–9.
- Murawski, H., Meyer, W., 2004. *Geologisches Wörterbuch*, 11th Edition. Elsevier.
- Mustard, J. F., Murchie, S. L., Pelkey, S. M., Ehlmann, B. L., Milliken, R. E., Grant, J. A., Bibring, J.-P., Poulet, F., Bishop, J., Dobra, E. N., Roach, L., Seelos, F., Arvidson, R. E., Wiseman, S., Green, R., Hash, C., Humm, D., Malaret, E., McGovern, J. A., Seelos, K., Clancy, T., Clark, R., Marais, D. D., Izenberg, N., Knudson, A., Langevin, Y., Martin, T., McGuire, P., Morris, R., Robinson, M.,

- Roush, T., Smith, M., Swayze, G., Taylor, H., Titus, T., Wolff, M., Jul. 2008. Hydrated silicate minerals on Mars observed by the Mars Reconnaissance Orbiter CRISM instrument. *Nature* 454, 305–309.
- Nass, A., van Gasselt, S., Jaumann, R., Asche, H., Sep. 2010. Cartographic Symbolization and Management for GISbased Geological and Geomorphological Mapping. In: European Planetary Science Congress 2010. p. 602.
- Nass, A., van Gasselt, S., Jaumann, R., Asche, H., Sep. 2011a. Implementation of cartographic symbols for planetary mapping in geographic information systems. *Planetary and Space Science* 59, 1255–1264.
- Nass, A., van Gasselt, S., Roatsch, T., Hauber, E., Jaumann, R., Oct. 2011b. GIS-based Cartographic Approaches for Geological and Geomorphological Mapping: Current Status. In: EPSC-DPS Joint Meeting 2011. p. 854.
- Neukum, G., 1983. Meteoritenbombardement und datierung planetarer oberflächen. Ph.D. thesis, University of Munich.
- Neukum, G., Ivanov, B., 1994. Crater size distributions and impact probabilities on Earth from lunar, terrestrial-planet, and asteroid cratering data. Gehrels, T., Matthews, M.S., Schumann, A.M. (Eds.).
- Neukum, G., Jaumann, R., 2004. Mars Express: the scientific payload. ESA Publications Division.
- Osterloo, M. M., Anderson, F. S., Hamilton, V. E., Hynek, B. M., Oct. 2010. Geologic context of proposed chloride-bearing materials on Mars. *Journal of Geophysical Research (Planets)* 115, 10012.
- O’Sullivan, D., Unwin, D., 2010. *Geographic Information Analysis*, 2nd Edition. John Wiley & Sons.
- Pain, C. F., Clarke, J. D. A., Thomas, M., Oct. 2007. Inversion of relief on Mars. *Icarus* 190, 478–491.
- Parker, T. J., Gorsline, D. S., Saunders, R. S., Pieri, D. C., Schneeberger, D. M., Jun. 1993. Coastal geomorphology of the Martian northern plains. *Journal of Geophysical Research* 98, 11061.
- Parker, T. J., Saunders, R. S., Schneeberger, D. M., Nov. 1989. Transitional morphology in west Deuteronilus Mensae, Mars - Implications for modification of the lowland/upland boundary. *Icarus* 82, 111–145.
- Pechmann, J. C., May 1980. The origin of polygonal troughs on the northern plains of Mars. *Icarus* 42, 185–210.
- Pedersen, G. B. M., Head, J. W., 2011. Chaos formation by sublimation of volatile-rich substrate: Evidence from galaxias chaos, mars. *Icarus* 211, 316–329.
- Poulet, F., Bibring, J.-P., Mustard, J. F., Gendrin, A., Mangold, N., Langevin, Y., Arvidson, R. E., Gondet, B., Gomez, C., Dec. 2005. Phyllosilicates on Mars and implications for early martian climate. *Nature* 438, 623–627.
- Press, F., Siever, R., Grotzinger, J., Jordan, T. H., 2003. *Understanding Earth*. W. H. Freeman.

- Richards, J., 2013. Remote Sensing Digital Image Analysis: An Introduction. Springer.  
URL <http://books.google.de/books?id=ETfwQnBMP4UC>
- Rodriguez, J. A. P., Sasaki, S., Kuzmin, R. O., Dohm, J. M., Tanaka, K. L., Miyamoto, H., Kurita, K., Komatsu, G., Fairén, A. G., Ferris, J. C., May 2005. Outflow channel sources, reactivation, and chaos formation, Xanthe Terra, Mars. *Icarus* 175, 36–57.
- Russell, P. S., Head, J. W., 2007. The martian hydrologic system: Multiple recharge centers at large volcanic provinces and the contribution of snowmelt to outflow channel activity. *Planetary and Space Science* 55, 315–332.
- Sato, H., Kurita, K., Baratoux, D., May 2010. The formation of floor-fractured craters in Xanthe Terra. *Icarus* 207, 248–264.
- Scholten, F., Roatsch, T., Gwinner, K., Matz, K.-D., Mertens, V., Flohrer, J., Waehlich, M., Giese, B., Pischel, R., Oberst, J., Jaumann, R., Neukum, G., the HRSC Co-Investigator Team, 2005. Von rohdaten aus dem mars express orbit zu digitalen gelaendemodellen und orthobildern-operationelle verarbeitung von hrsc daten. *Photogrammetrie-Fernerkundung-Geoinformation* 5, 365–372.
- Schowengerdt, R. A., 1997. Remote Sensing- Models and Methods for Image Processing. Academic Press.
- Schultz, P. H., 1976. Floor-fractured lunar craters. *The Moon* 15, 241–273.
- Schumacher, S., Zegers, T. E., 2011. Aram chaos and its constraints on the surface heat flux of mars. *Icarus* 211, 305–315.
- Scott, D., Dohm, J. M., Rice Jr., J., 1995. Map of mars showing channels and possible paleolake basins. USGS.
- Seidelmann, P. K., Abalakin, V. K., Bursa, M., Davies, M. E., de Bergh, C., Lieske, J. H., Oberst, J., Simon, J. L., Standish, E. M., Stooke, P., Thomas, P. C., Jan. 2002. Report of the IAU/IAG Working Group on Cartographic Coordinates and Rotational Elements of the Planets and Satellites: 2000. *Celestial Mechanics and Dynamical Astronomy* 82, 83–111.
- Sharp, R., Malin, M. C., 1975. Channels on mars. *Geological Society of America Bulletin* 86, 593–609.
- Sharp, R. P., 1973. Mars: Fretted and chaotic terrains. *Geophysical Research Letters* 78, 4073–4083.
- Sheng, D., Sloan, S. W., Gens, A., Smith, D. W., Aug. 2003. Finite element formulation and algorithms for unsaturated soils. Part I: Theory. *International Journal for Numerical and Analytical Methods in Geomechanics* 27, 745–765.
- Smith, D. E., Zuber, M. T., Frey, et al., Oct. 2001. Mars Orbiter Laser Altimeter: Experiment summary after the first year of global mapping of Mars. *Journal of Geophysical Research* 106, 23689–23722.

- Smrekar, S. E., McGill, G. E., Raymond, C. A., Dimitriou, A. M., Nov. 2004. Geologic evolution of the Martian dichotomy in the Ismenius area of Mars and implications for plains magnetization. *Journal of Geophysical Research (Planets)* 109, 11002.
- Snyder, G. S., Ashworth, Jr., W. B., Nov. 1987. Book-Review - *Maps of the Heavens*. *Journal for the History of Astronomy* 18, 287.
- Squyres, S. W., Carr, M. H., Jan. 1986. Geomorphic evidence for the distribution of ground ice on Mars. *Science* 231, 249–252.
- Survey, U. G., March 2014. Usgs glossary.  
URL <http://geomaps.wr.usgs.gov/parks/misc/glossarya.html>
- Tanaka, K. L., 1986. The stratigraphy of mars. *Geophysical Research Letters* 91, E139–E158.
- Tornabene, L. L., Ling, V., Osinski, G. R., Boyce, J. M., Harrison, T. N., McEwen, A. S., Mar. 2013. A Revised Global Depth-Diameter Scaling Relationship for Mars Based on Pitted Impact Melt-Bearing Craters. In: *Lunar and Planetary Institute Science Conference Abstracts*. Vol. 44 of *Lunar and Planetary Institute Science Conference Abstracts*. p. 2592.
- University, W., April 2013. Mars ororbit data explorer.  
URL <http://ode.rsl.wustl.edu/mars/indexProductSearch.aspx>
- Velde, B. (Ed.), 1995. *Origin and Mineralogy of Clays- Clays and the Environment*. Springer.
- Watson, I., Burnett, A., 1993. *Hydrology: An Environmental Approach*. CRC Press.
- Wenrich, M. L., Christensen, P. R., 1993. A formational model for the polygonal terrains of mars: Taking a crack at the genesis of the martian polygons. *Lunar and Planetary Inst. Workshop on the Martian Northern Plains: Sedimentological, Periglacial, and Paleoclimatic Evolution*, 19–21.
- Wenrich, M. L., Christensen, P. R., 1996. A formational model for the martian polygonal terrains. *Lunar and Planetary Science* 27, 1419.
- Wessel, P., Smith, W. H. F., 2013. *The Generic Mapping Tools (GMT) version 4.5.9 Technical Reference & Cookbook*. SOEST/NOAA.
- Wichman, R. W., Schultz, P. H., 1996. Crater-centered laccoliths on the moon: Modeling intrusion depth and magmatic pressure at the crater taruntius. *Icarus* 122, 193–199.
- Wolf, P., Ghilani, C., 1997. *Adjustment computations: statistics and least squares in surveying and GIS*. No. Bd. 1 in 3rd Ed). John Wiley & Sons.  
URL <http://books.google.de/books?id=de1RAAAAMAAJ>
- Wolf, P., Ghilani, C., 2006. *Elementary surveying: an introduction to Geomatics*. Pearson Prentice Hall.
- Worboys, M. W. M. D. M., 2004. *GIS: A Computing Perspective*. CRC Press.



Xiao, L., Huang, J., Christensen, P. R., Greeley, R., Williams, D. A., Zhao, J., He, Q., Mar. 2012. Ancient volcanism and its implication for thermal evolution of Mars. *Earth and Planetary Science Letters* 323, 9–18.

Zandbergen, P. A., 2013. *Python Scripting for ArcGIS*. Esri Press.

Zegers, T. E., Oosthoek, J. H. P., Rossi, A. P., Blom, J. K., Schumacher, S., Sep. 2010. Melt and collapse of buried water ice: An alternative hypothesis for the formation of chaotic terrains on Mars. *Earth and Planetary Science Letters* 297, 496–504.



# Appendix

## Publications

Bamberg, M., Jaumann, R., Asche, H., Kneissl, T., Michael, G.G. (2013): Floor Fractured Craters on Mars- Observations and Origin, Planetary and Space Science, Special Issue, doi:10.1016/j.pss.2013.09.017.

Bishop, J. L., Tirsch, D., Tornabene, L. L., Jaumann, R., McEwen, A. S., McGuire, P. C., Ody, A., Poulet, F., Clark, R. N., Parente, M., Voigt, J., Aydin, Z., Bamberg, M., Petau, A., McKeown, N. K., Mustard, J. F., Hash, C., Murchie, S. L., Swayze, G., Neukum, G. & Seelos, F. (2013) Mineralogy and morphology of geologic units at Libya Montes, Mars: Ancient aqueous outcrops, mafic flows, fluvial features and impacts. *Journal of Geophysical Research*, 118, doi:10.1029/2012JE004151.

## Conference Contributions

Bamberg, M., Asche, H., Jaumann (2013c): Additional Tools for Surface Analysis in ArcGIS, EPSC Meeting (Talk), London (Great Britain), abstract #2013-435.

Bamberg, M., Asche, H., Jaumann, Kneissl, T. (2013b): Quantitative and Statistical Analysis of Floor Fractured Craters, EPSC Meeting (Talk), London (Great Britain), abstract #2013-416.

Bamberg, M., Jaumann, R., Asche, H., Kneissl, T., Michael, G.G. (2013a): Observations and Origins of Fractured Craters on Mars, 44rd Lunar and Planetary Science Conference (Talk), The Woodlands, Texas (USA), abstract #2362.

Osinski, G. R.; Ferrière, L.; Kring, D. A.; Anders, D.; Armstrong, K.; Baker, D.; Bamberg, M.; Beddingfield, C.; Gaither, T.; Harrison, T.; Huber, M. S.; Hurwitz, D.; Jaret, S.; Kramer, G.; Kuriyama, Y.; Lucas, M.; Marion, C. L.; Mercer, C.; Mount, C.; Neish, C.; Nuhn, A.; Ostrach, L.; Pickersgill, A.; Pilles, E.; Potter, R. W. K.; Ryan, A.; Sharp, M.; Swartz, N.; Thomson, O.; Veto, M.; Wielicki, M. M.; Wright, S.; Zanetti, M. (2013): Revisiting the Distribution and Properties of Shatter Cones at the Sudbury Impact Structure, Canada, LPI Contribution No.1737, abstract #3061, Sudbury, Canada, 5-8 Aug.

Bamberg, M., Kneissl, T., Michael, G.G., Jaumann, R., Asche, H. (2012e): Floor Fractured Craters on Mars- an Overview, Northern Arizona University (Invited Talk), Flagstaff (USA).

Bamberg, M., Kneissl, T., Michael, G.G., Jaumann, R., Asche, H. (2012d): Comparison of Floor Fractured Craters- a Case Study for Mars, Planetary Crater Consortium Meeting (Talk), Flagstaff (USA), abstract#1201.

Bamberg, M., Jaumann, R., Asche, H. (2012c): Comparison of Floor Fractured Craters- a Case Study for Mars, EPSC Meeting, Madrid (Spain), abstract #2012-304.

Bamberg, M., Jaumann, R., Asche, H. (2012b): Floor Fractured Craters around Syrtis Major, Mars, EGU General Assembly, Geophysical Research Abstracts Vol.14, Vienna (Austria), abstract #2012-2406.

Bamberg, M., Jaumann, R., Asche, H. (2012a): Floor Fractured Craters around Syrtis Major, Mars, 43rd Lunar and Planetary Science Conference, The Woodlands, Texas (USA), abstract #1833.

Bamberg, M., Jaumann, R., Asche, H., Nass, A. and Tirsch, D. (2011b): Fractured Craters in Southern Syrtis Major, Mars, EPSC-DPS Joint Meeting, Nantes (France), abstract #2011-401-3.

Bamberg, M., Jaumann, R., Asche, H., Naß, A., Tirsch, D. (2011a): Young basaltic deposits in impact craters at the south-eastern extension of Syrtis Major, Mars: preliminary report, EGU General Assembly, Geophysical Research Abstracts Vol.13, Vienna (Austria), abstract #2011-3182-2.

Tirsch, D., Erkeling, G., Bishop, J., Jaumann, R., Bamberg, M. (2011): The Libya Montes Region on Mars: Geology, Mineralogy, and Possible Habitable Environments, 2011 Fall Meeting, AGU, #abstract P21B-1666, San Francisco, Calif., 5-9 Dec.

## Awards

### **Outstanding Student Poster(OSP) Award 2012**

European Geosciences Union, Vienna, Austria

Floor Fractured Craters around Syrtis Major, Mars

Bamberg, M., Jaumann, R., Asche, H.

## Curriculum Vitae

Page 143 (Curriculum Vitae) is not included in the online publication, due to personal data.

Die Seite 143 (Curriculum Vitae) enthält persönliche Daten. Sie ist daher nicht Bestandteil der Online-Veröffentlichung.